Modélisation des ondes infragravitaires : de l'échelle régionale à l'échelle mondiale

Arshad Rawat

THÈSE / UNIVERSITÉ DE BRETAGNE OCCIDENTALE

sous le sceau de l'Université européenne de Bretagne

pour obtenir le titre de

DOCTEUR DE L'UNIVERSITÉ DE BRETAGNE OCCIDENTALE

École Doctorale des Sciences de la Mer

présentée par

Arshad RAWAT

Préparée au Laboratoire d'Océanographie Spatiale

Numerical Modelling of Infragravity Waves

From regional to global scales

Thèse soutenue le 13 mars 2015
devant le jury composé de :

A.J.H.M RENIERS
Dr.ir., Professor, TU Delft

Wayne CRAWFORD
Dr, HDR, CNRS Researcher, Institut de Physique du Globe

Nadia SENECHAL
Maître de Conférences HDR, Université de Bordeaux

Christophe DELACOURT
Professeur des Universités, UBO

Fabrice ARDHUIN
Dr, HDR, Directeur de Recherche, Laboratoire de Physique des Océans, CNRS - Ifremer

Jérome AUCAN
Dr, Chercheur, Institut de Recherche pour le Développement (IRD), LEGOS

“And on that Day, We shall let them surge on one another like waves in the sea and then the Trumpet will be blown, and We shall gather them all together”

Acknowledgement

This thesis report concludes the PhD program prepared at the Ecole Doctorale des Sciences de la Mer, of the Université de Bretagne Occidental in Brest, France under the under the aegis of the Université européenne de Bretagne. This study was conducted over a period of 3 years mainly at the Laboratoire d'Oceanograhie Spaciale of Ifremer in Brest, France and partly at the Mauritius Oceanography institute.

First and foremost, I would like to thank the members of the graduation committee for accepting to be part of it and for their supervision and feedback. Special thanks to my PhD advisor Fabrice Ardhuin for his input and guidance throughout the project, and also to all the colleagues at the LOS including Bertrand Chapron, Jean, Mickael, Olivier, Abderrahim, Fanny, Pierre, Marie Laure, Francine, Janick, Guillaume, Li Yun and Elisabeth Bondu from the EDSM for their help, support and for the great atmosphere during my stay there. I would also like to thank colleagues at the Mauritius Oceanography institute including Reza, JIM and Dinesh for their support and advice.

I am also extremely grateful to Dr. Ad Reniers and Dr, Wayne Crawford who have kindly accepted to review this thesis manuscript.

This PhD work was co-funded by the CNES as part of the SWOT preparation program and the U.S. National Ocean Partnership Program, under grant N00014-10-1-0383.

Finally, and more importantly I want to thank my family and friends both in Mauritius and in France for their support during these past 3 years.

Brest, February 2015

Foreword

Wind-generated surface gravity waves are ubiquitous at the ocean surface. Their period varies between 2 and 25 seconds, with wavelength varying between a few meters to several hundreds of meters. Longer and, lower frequency surface gravity waves, called infragravity (IG) waves, are associated to these short, high frequency wind-generated waves. These infragravity waves have dominant periods comprised between 30 seconds and 10 minutes, and, when they propagate freely, with horizontal wavelengths of up to tens of kilometres, as given by the linear surface gravity wave dispersion relation. Outside of surf zones, the vertical amplitude of these infragravity waves is of the order of 1-10 cm, while the amplitude of wind-generated waves is of the order of 1-10 m.

Given the length scales of the infragravity wavelengths, and despite the fact that the infragravity wave field exhibits much smaller vertical amplitudes than the high frequency wind-driven waves, the infragravity wave field will be a significant fraction the signal measured by the future Surface Water Ocean Topography satellite (SWOT) mission. This infragravity wave field will have to be characterized in order to achieve the expected precision on dynamic height measurements. It appears likely that the above mentioned precision will not be feasible for high sea states and long and steep swells. One of the aims of this thesis was to provide a first quantification of these associated uncertainties. Beyond the SWOT mission, the quantification of the IG wave field is a key problem for the understanding of several geophysical phenomena, such as the understanding of microseisms and ice shelves break up.

Nomenclature

α	Dimentional constant in empirical formulation of IG wave
$E(f)$	Spectral energy density (m^2/Hz or m^2s)
$E(f,\theta)$	Directional spectral-energy density ($m^2/Hz/rad$ or $m^2s.rad^{-1}$)
σ_i	Angular pulsation for wave component i
$\boldsymbol{k}_i$	Wavenumber vector for wave component i
θ_i	Propagation direction of wave component i
ϕ	Velocity potential
ζ or η	Free surface elevation
D_s	Surface elevation 2nd order coupling coefficient
D_p	Bottom pressure 2nd order coupling coefficient
$N(k,\theta)$	Wave action spectrum in terms or wavenumber and direction
S_{xx}	Cross-shore radiation stress
S_{yy}	Long-shore radiation stress

$T_{m0,-2}$	Mean period given by the -2 and 0 moments of the surface elevation spectrum
γ_{lib}	Gamma-l, liberation parameter

Abbreviations

D or H	Water depth
free IG	Free infra-gravity waves
Hs	Significant wave height
H_{IG}	Significant wave height in the infragravity band
H_{rms}	Root-mean-squared wave height
IG	Infra-Gravity
JONSWAP	Joint North Sea Wave Project parametric spectral shape
P or *p*	Pressure
SWASH	Simulating WAves till SHore
SWOT	Surface Water Ocean Topography (SWOT) mission
LW	Long wave
SW	Short wave
T	Wave period
WWIII	WAVEWATCH III (WAVEs WATer level and Current Hindcasting)
XBeach	eXtreme BEACH behaviour model
Zs	Free surface elevation

Contents

1 Introduction

1.1 What are infragravity waves?

Infragravity (IG) waves are ocean gravity waves having long-periods and wavelengths. The periods can be of several minutes and the wavelengths may be tens of kilometers long. They share some characteristics with tsunamis and internal waves but with specific origins and characteristics. Usually gravity waves with periods ranging from 30 to 300 seconds are referred to as infragravity waves. Infragravity waves are generated mostly along the continental shelf by nonlinear wind wave interactions. These differ from normal oceanic gravity waves, which are created by the action of the wind acting directly on the sea-surface. However the restoring force is still gravity, explaining their classification as gravity waves.

In the wave spectrum, they correspond to the frequency band which comes just before the wind waves which consist of both wind-sea and swell. A qualitative analysis of the wave power spectrum from Munk (1950) can be seen in Figure 1.

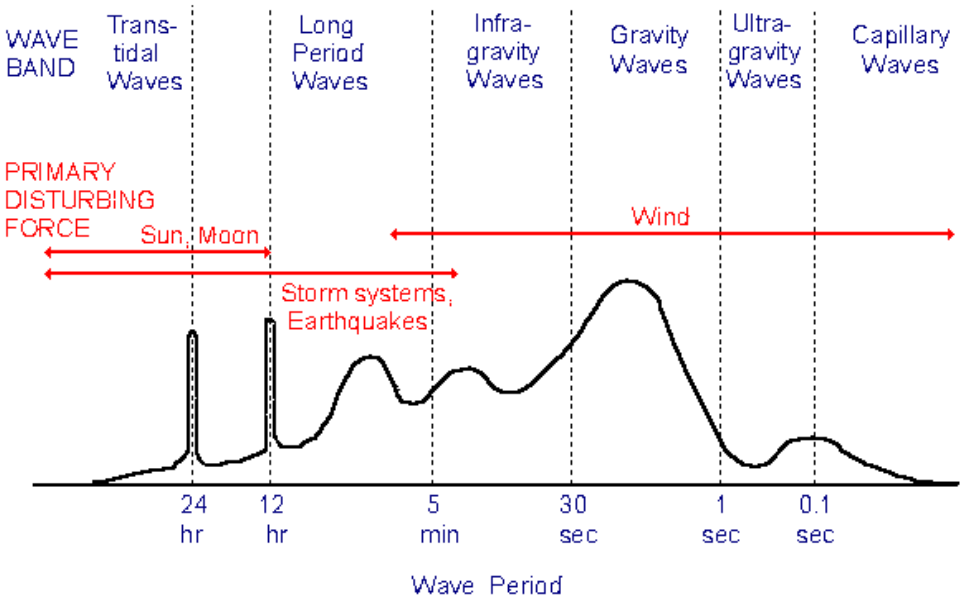

Figure 1.1: Qualitative wave energy spectrum showing the range of Infragravity waves (adapted from Munk, 1950).

The first investigations of IG waves were carried out by Munk (1949) and Tucker, (1950). Initially the waves were observed as sea level changes in the surf zone, and thus they became known as surf beats. Later it was realized that these waves can occur anywhere by nonlinear interactions among wind waves. The more general term infragravity wave was thus proposed by Kinsman, (1965) and became accepted for these waves.

The amplitudes of IG waves are dependent on the water depth, ranging from a few

centimeters in the open ocean (Aucan & Ardhuin, 2013) to several meters near the shoreline (Sheremet et al., 2014). They can thus be of great interest for the correction of altimetry derived sea-surface heights across the oceans, as well as for storm surge investigation along coastal areas and harbour oscillations.

As the wind waves interact among themselves and with the topography, the nonlinear processes convert some of their energy into sub-harmonics giving rise to the infragravity waves. The resulting long period oscillations appear as 'bound' to the underlying wave groups (e.g. Herbers et al. 1994, 1995). Hence, these group-induced long waves are of periods and wavelengths equal to that of the underlying wave groups and they travel with the group velocity. Bound waves do not follow the dispersion relationship of linear surface gravity waves.

Infragravity waves can be found in various measurements, both in shallow water and in the deep ocean with instruments ranging from wave-riders and tsunameters to ocean-bottom seismometers (OBS).

The signature of infragravity waves can also be found in the seismic noise (microseisms). Two main mechanisms are thought to give rise to microseisms (Hasselmann 1963). In the case of infragravity waves, it is their interaction with the bottom topography that can explain the generation of seismic waves with the same frequency and their variability (Ardhuin et al., 2015). The sources of seismic noise with periods 50 to 300 s were found to be located along the shelf breaks, generated by IG waves of the same period.

1.2 Sources of infragravity waves

Longuet-Higgins and Stewart (1962) suggested that as the incident swell are dissipated in the surf zone, the associated bound Infragravity waves are released as free waves. The bound IG waves form the set-down that accompanies wave groups, with the same periodicity, wavelengths and group velocity as the wave groups. The bound waves are believed to be liberated at the shore line where the short waves break (Bowen and Huntley, 1984; Oltman-Shay and Guza, 1987). Upon liberation the IG waves then reflect from the beach and propagate toward the sea. An alternative mechanism resulting from a varying breakpoint position could however also play a significant part (Symonds et al., 1982).

Extensive observations on both Pacific and Atlantic continental shelf sites show a strong correlation between infragravity and swell energy levels, and suggests that free infragravity waves are predominantly radiated from the beach (Herbers et al., 1995a and others).

Given their long wavelength, most of the free IG energy is trapped by refraction on the shelf, where they are referred to as edge waves. Edge waves propagate along the shore, where they are mostly dissipated but with some part gradually leaking into deeper waters (Holman and Bowen, 1984; Bowen and Huntley, 1984; Oltman-Shay, and Guza,

1987). The small fraction of the IG energy that goes back into the open ocean is known as leaky waves. Observed infragravity energy levels on the beach, shelf and in the open ocean are indeed qualitatively consistent with strong refractive trapping and a relatively weak leaky component (e.g., Webb et al., 1991; Okihiro et al., 1993; (Herbers et al., 1995)).

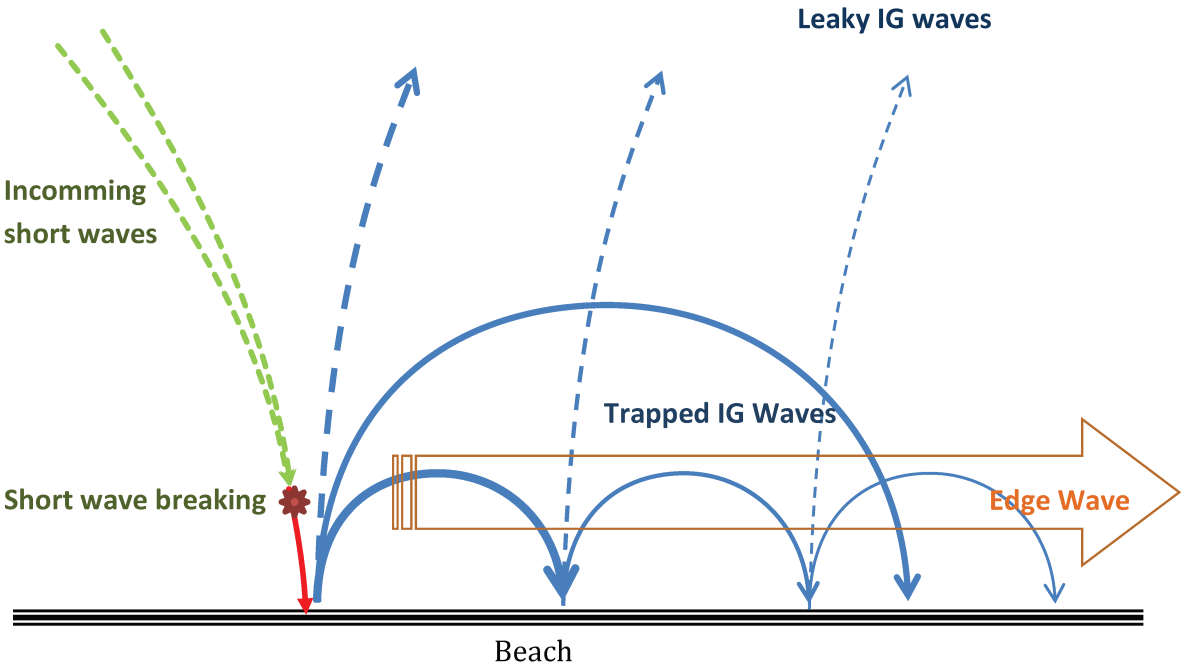

Figure 1.2: Illustration of generation of free IG by the liberation mechanism. Two short waves with slightly different frequencies (green dashed rays) form a forced wave with a 'difference' frequency corresponding to the wave group envelope. The forced wave then gets liberated as the short waves break (star). The free wave (red ray) then propagates towards the shore and is subsequently reflected and refracted several times (blue solid rays) and gradually partly dissipating and partly leaking back to the sea (blue dashed rays).

More recently, Harmon et al. (2012) were able to use differential pressure gauges to localise IG wave generation areas from ambient noise correlation. Godin et al (2013) developed a simple model of the spectral and spatial distribution of IG energy in the deep ocean off New Zealand, also from a network of seafloor pressure sensors. Godin et al., (2014) used wave interferometry to investigate the propagation and directional properties of infragravity waves away from the shore of New Zealand. It was found that free, linear waves with a strongly anisotropic power flux density distribution were dominant in the IG wavefield.

Webb et al. (1991) showed that the observed pressure spectra below 0.03 Hz in the deep ocean are mostly free infragravity waves rather than bound IG at that location and suggested they originate from remote shorelines. A relationship between long wave energy at a particular location and the average height of the short waves incident on coastlines 'seen' from that location was used to successfully explain the observations. Aucan & Ardhuin (2014) analysis of multiyear pressure records in the Pacific Ocean

showed IG levels which were seasonal and higher than previously reported. Here also the IG levels at a spot varied proportionally to short waves impacting corresponding coastlines. However the exact sources of remote IG waves within an oceanic basin and their paths of propagation were never studied and will be studied in the last chapter of this thesis.

1.3 Why study infragravity waves?

IG waves have been studied since the 1950's but many aspects remain poorly understood. For example we do not know yet how in the ocean much IG energy is created and where, also concerning its dissipation or its interaction with wind-waves and swells. But the IG signal can be found in a wide range of environments, even in land-based seismic records.

Even though the amplitudes of IG waves can be just a few centimeters in the open ocean, they can still be of great interest. For example if the sea level needs to be measured at 1 cm accuracy and a resolution under 20 km, as intended for the upcoming SWOT and Compira satellite altimetry missions, the presence of IG waves could be detrimental. The global IG wave field hence needs to be properly known for the correction of these measured sea-surface heights, or at least for estimating the level of error.

During large storms, IG waves can actually be very high right on the shoreline (up to 3 m height, Sheremet et al. 2014) and this can strongly contribute to storm surge and coastal flooding. In the domain of coastal dynamics, IG-waves have been found to be responsible for many phenomena, including the formation of rip currents, wave set-up, sand bars, beach cusps and other forms of coastal topographies, as well as sediment transport.

IG waves can also induce seiche in semi-closed basins, such as ports and harbours (Okihiro et al., 1993). These basins usually have natural periods of a few minutes which coincide with to the frequency band of long waves, including IG waves. Hence IG waves in the ocean are the primary factor determining the intensity of harbour oscillations through resonance. Seiche-generating motions outside the harbour can arise from both bound and free IG waves that are incident on the harbour entrance.

Seiche motions in these basins create unacceptable vessel movement which can, in turn, lead to the breaking of mooring lines, fenders and piles, and to the onset of large amplitude ship oscillations and damage. The same kind of structural stress can also occur offshore where IG waves can excite resonances in mooring systems in oil-production or storage facilities at sea (floating production, storage and offloading (FPSO) units).

Resonance at IG wave periods can also lead to the breaking up of ice tongues around polar regions (Bromirski et al., 2010), which can be of much importance in the context of global warming. IG waves can propagate under sea ice with little energy loss but a change in phase speed that depend on ice thickness (sea ice tomography, Wadhams and Doble, 2008).

1.4 Plan of work

The main aim of this study is to build a global model for IG waves, which has not been done previously. Due to limits in computing power, this model cannot be phase resolving. This would require resolutions in the order of the length of the short waves (sea and swell). Since this is not feasible at global scales, we will instead use third generation spectral models, which are nowadays being routinely run on such scales. Examples include WAVEWATCH III (Tolman et al., 2014) and WAM (WAMDI Group, 1988)

To set up such a model, we will in the first part of this study focus on some general and theoretical aspects of bound and free Infragravity waves. We will estimate the bound IG energy from accurate frequency-directional wave spectra or by using a bispectral analysis and document the liberation of IG waves into free modes at the shoreline.

In the next chapter, some basic phase-resolving modelling will be carried out in order to characterise the coastal variability of free infragravity wave energy in terms of incoming short waves and topographic characteristics. The amount of leaky infragravity waves radiated offshore for a given incident short wave spectrum on a given coastline is going to be studied on local and regional scales using current phase resolving models such as SWASH (Zijlema et al., 2011) and XBeach (Roelvink et al., 2009b).

The results will then be used to set up source terms for free IG waves within the WAVEWATCH III spectral wave model. This will then be calibrated and validated with several observation datasets on regional scales and finally on global scales. In the last chapter we will study specific IG event, including the generation and the propagation of large IG events across ocean basins. These major IG bursts are believed to be the most problematic in the context of precise satellite altimetry measurements or the breaking of ice tongues off Antarctica.

2 General Aspects of Infragravity Waves

In general, the observed infragravity field is a mixture of forced waves, phase-coupled to local wave groups, and (uncoupled) free waves. In the deep ocean, the contribution of forced waves to the infragravity energy is very low but increases with increasing swell energy and decreasing water depth (Herbers et al. 1994). In shallow water waves are more nonlinear and the second-order effects are relatively large and help to explain the formation of infra-gravity waves in the coastal zone. Deeper waters are usually dominated by free waves. In this chapter we are going to recapitulate the main theoretical background of bound and free waves.

2.1 Bound Infragravity Waves

From a mathematical point of view, the nonlinear wave interactions that give rise to infragravity waves come from the second-order terms in the wave equation (Hasselmann, (1962) and others). The long waves in a regular wave group were shown by Longuet-Higgins and Stewart, (1962) by to be produced by fluxes of mass and momentum associated with ocean waves. These fluxes of mass and momentum act through the radiation stress which is an internal compressive force proportional to the square of the wave height. The variation of the radiation stresses induces changes in the mean surface elevation (wave setup and setdown) which result in a long wave that is bound to the propagating wave groups. The mechanism by which the radiation stress influences the flow equations is explained in the appendix.

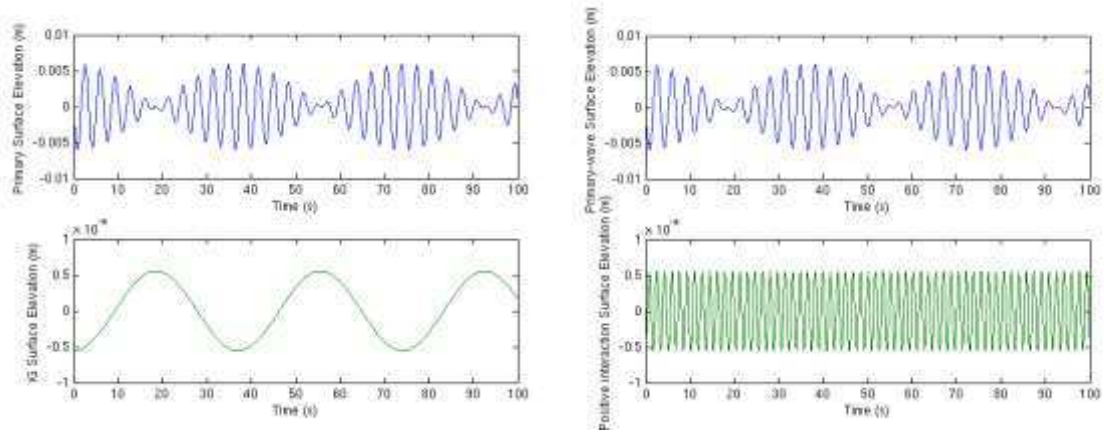

Figure 2.1: An analytical example of first- and second-order waves. The blue signal line shows first order wave train. The green curve on the bottom left shows the 'difference' second-order terms which corresponds to the IG bound wave. The green curve on the bottom right shows the higher frequency 'sum' interaction second-order component.

The bound IG waves form the set-down that accompanies wave groups, having troughs that are beneath the high short waves of the group and crests in-between the wave groups (Longuet-Higgins and Stewart, 1962). They have the same periodicity and the same lengths as the wave groups but do not follow the dispersion relation. They travel

with the group velocity of the short waves , which is significantly smaller than the phase speed of free long waves with the same frequencies.

The wave group speed, and hence the bound IG wave speed is given by

$$c_g = \frac{\partial \sigma}{\partial k} = c\left(\frac{1}{2} + \frac{kD}{sinh\, 2kD}\right) \tag{2.1}$$

where c is the phase velocity of the individual waves given by the dispersion relation

$$c = \frac{\sigma}{k} = \left[\frac{g}{k}\tanh(kD)\right]^{1/2} \tag{2.2}$$

and σ is the angular frequency with D being the local water depth.

The second-order equations also show that the bound IG waves are determined by the difference of the wave-number vectors of the short waves. This is referred to as 'difference' interaction or the generation of sub-harmonics. 'Sum' interactions are also possible, with the non-linearities producing higher frequency harmonics as shown in Figure 2.1, but are not going to be studied here. There is also a quadratic dependency of the bound long-waves with the short wave height as discussed in the appendix.

2.1.1 Second order approximation for the surface elevation

The expression for the bound IG wave elevations is a function of the first-order components of the wave field modulated by a second order transfer function. In its most complete form, the inviscid, incompressible and irrotational wave equation is given by Stokes (1849) and Miche (1944)

$$\frac{\partial^2 \phi}{\partial t^2} + g\frac{\partial \phi}{\partial z} = g\nabla\phi \cdot \nabla\zeta - \frac{\partial \varsigma}{\partial t}\cdot\frac{\partial^2 \phi}{\partial z \partial t} - \left(\frac{\partial}{\partial t} + \frac{\partial \zeta}{\partial t}\cdot\frac{\partial}{\partial z}\right)\left[\nabla\phi\cdot\nabla\phi + \frac{\partial \phi}{\partial z}\cdot\frac{\partial \phi}{\partial z}\right] + C'(t) \tag{2.3}$$

Here ζ is the free surface elevation and ϕ is the velocity potential. Predictions of infragravity bound waves in constant depth are obtained by expanding (2.1) together with the boundary conditions by the method of Stokes, to the second order in the wave slope (Biesel, 1952; Longuet-Higgins and Stewart, 1964, 1962, 1960; Hasselmann, 1962; and others). Assuming small wave slopes, an approximate solution can be obtained by expanding the wave parameters ζ and ϕ as a perturbation series (Stokes, 1849)

$$\begin{aligned} \phi &= \phi^{(1)} + \phi^{(2)} + \phi^{(3)} + \ldots \\ \zeta &= \zeta^{(1)} + \zeta^{(2)} + \zeta^{(3)} + \ldots \end{aligned} \tag{2.4}$$

At lowest order, i.e. the linearized version of (2.1), the sea surface elevation is assumed

to be a linear sum of free waves (the Airy solution).

$$\zeta^{(1)}(\vec{x},t)=\sum_{\vec{k},s} Z_{\vec{k}}^{s}\, e^{i.\left(\vec{k}.\vec{x}-s\sigma t\right)} \tag{2.5}$$

With $\sigma_i \equiv 2\pi.s_i f_i$, $s_i = \pm 1$, $Z_{\vec{k}}^{s}$ being the amplitude of each component. Equation (2.6) below is the usual dispersion relation linking σ_i and k_i at depth h. The $\vec{x}$ notation denotes two dimensional vectors or operators in the xy-plane.

$$\sigma_i \equiv \sqrt{g k_i \tanh\left(k_i h\right)} \tag{2.6}$$

The second order correction is given by

$$\zeta^{(2)}(\vec{x},t)=\sum_{s1=\pm 1} D_s(s_1 f_1, s_2 f_2, \Delta\theta)\cdot Z_{\vec{k}}^{(1)}{}_{s_1}\cdot Z_{\vec{k}}^{(1)}{}_{s_2}\times \exp[-i2\pi(s_1 f_1+s_2 f_2)t] \tag{2.7}$$

Where the coupling coefficient for the surface elevation variance between waves of frequency f_1 and f_2 and an angle θ is given by (Hasselmann 1962 and Okihiro et al. 1992)

$$\begin{aligned} D_s(s_1 f_1, s_2 f_2, \Delta\theta) = &-\frac{g k_1 k_2 cos(\Delta\theta)}{2\sigma_1\sigma_2}+\frac{\sigma_3^2-\sigma_1\sigma_2}{2g}+\frac{g\sigma_3}{[g k_3 tanh(k_3 h)-\sigma_3^2]\cdot\sigma_1\sigma_2} \\ &\times\left\{\sigma_3\left[\left(\frac{\sigma_1\sigma_2}{g}\right)^2-k_1 k_2 cos(\Delta\theta)\right]-\frac{1}{2}\left[\frac{\sigma_1 k_2^2}{cosh^2(k_2 h)}+\frac{\sigma_2 k_1^2}{cosh^2(k_1 h)}\right]\right\} \end{aligned} \tag{2.8}$$

With $\sigma_3=\sigma_1+\sigma_2$ and $k_3 \equiv \left\|\vec{k}_1+\vec{k}_2\right\| \equiv \sqrt{\left[k_1^2+k_2^2+2k_1 k_2\cos\left(\Delta\theta\right)\right]}$

It should be noted that the infragravity response depends strongly on the water depth and the appropriate depths must be chosen during the modelling and computation of second order responses.

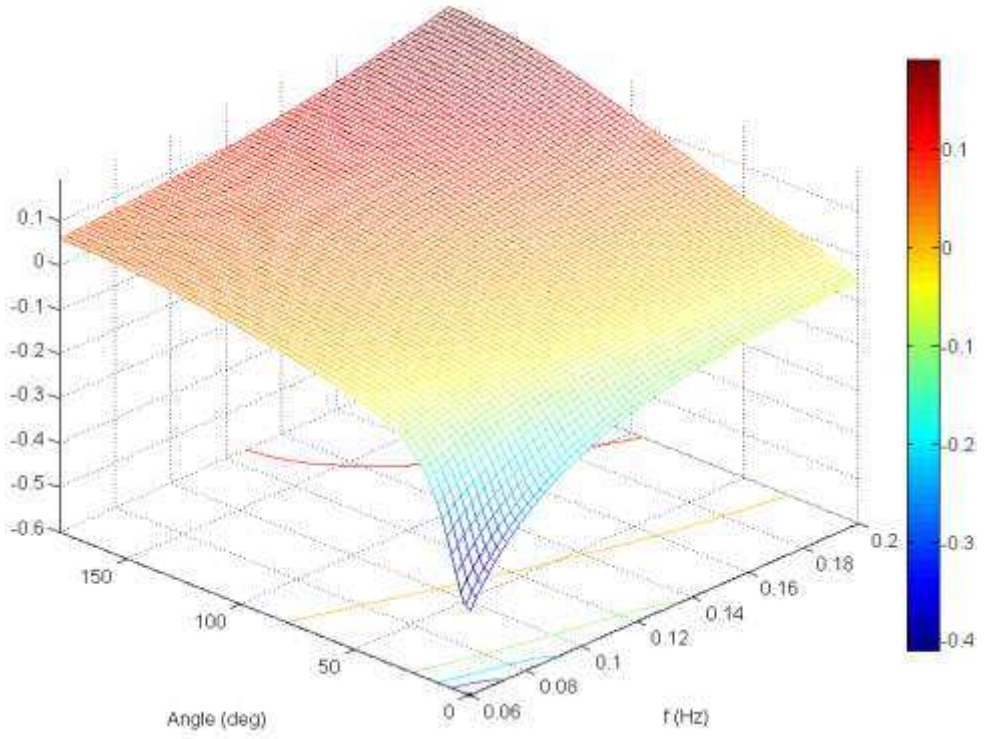

Figure 2.2: The variation of the surface elevation interaction coefficient D_s with the frequency f and the direction $\Delta\theta$ for a depth of 13m and a Δf of 0.03 Hz.

As seen from Figure 2.2, the absolute value of the surface elevation interaction coefficient increases as the frequency f and the direction difference $\Delta\theta$ decreases. Hence the bound IG energy at 0.03 Hz will be higher for directionally similar and lower frequency interacting waves, such as swells.

2.1.2 Second order approximation for bottom pressure

As with the free surface elevation and the velocity potential, the primary bottom pressure field can also be expressed through a perturbation expansion of the surface boundary conditions together with the Bernoulli equation as follows (Hasselmann, 1963, 1962)

$$p = p^{(1)} + p^{(2)} + p^{(3)} + \ldots \tag{2.9}$$

The primary bottom pressure $p^{(1)}(\vec{x},t)$ can be expressed as the Fourrier-Stieltjes transform (Hasselmann 1962)

$$p^{(1)}(\vec{x},t) = \int_k e^{i.(\vec{k}.\vec{x})} \cdot \left[dP_-^{(1)}(\vec{k}).e^{i\sigma t} + dP_+^{(1)}(\vec{k}).e^{-i\sigma t}\right] \tag{2.10}$$

Where $dP_{-}^{(1)}(\vec{k})$is the complex conjugate of $dP_{+}^{(1)}(-\vec{k})$.

The secondary bottom pressure $p^{(2)}(\vec{x},t)$ field is then given by (Herbers, 1994)

$$p^{(2)}(\vec{x},t) = \int_k \int_k \exp\left[i.\left((\vec{k}_1 + \vec{k}_2).\vec{x}\right)\right] \times \sum_{s1=\pm 1} D_p \cdot dP_{s_1}^{(1)}(\vec{k}_1) \cdot dP_{s_2}^{(1)}(\vec{k}_2) \times \exp[-i2\pi(s_1 f_1 + s_2 f_2)t] \quad (2.11)$$

Where the coupling coefficient $D_p(s_1 f_1, s_2 f_2, \Delta\theta)$for the bottom pressure between waves of frequencies f_1 and f_2 and travelling at an angle of $\Delta\theta$ ($=|\theta_1-\theta_2|$) with respect to each other is given by (Herbers et al. 1994)

$$D_p(s_1 f_1, s_2 f_2, \Delta\theta) = -\frac{g k_1 k_2 cos(\Delta\theta)}{2\sigma_1\sigma_2} + \frac{g\sigma_3 cosh(k_1 h) cosh(k_2 h)}{[g k_3 tanh(k_3 h) - {\sigma_3}^2] \cdot \sigma_1\sigma_2 cosh(k_3 h)} \times \left\{\sigma_3\left[\left(\frac{\sigma_1\sigma_2}{g}\right)^2 - k_1 k_2 cos(\Delta\theta)\right] - \frac{1}{2}\left[\frac{\sigma_1 k_2^2}{cosh^2(k_2 h)} + \frac{\sigma_2 k_1^2}{cosh^2(k_1 h)}\right]\right\} \quad (2.12)$$

With $\sigma_3 = \sigma_1 + \sigma_2$ and $k_3 \equiv \left\|\vec{k}_1 + \vec{k}_2\right\| \equiv \sqrt{[k_1^2 + k_2^2 + 2k_1 k_2 \cos(\Delta\theta)]}$

In the case of infra-gravity wave forcing, this coefficient is applied as $D(f+\Delta f, -f, \Delta\theta+\pi)$. Physically, this corresponds to the interaction of two primary swell-sea waves of frequencies $f+\Delta f$ and f with a directional difference of $\Delta\theta$ to produce a forced secondary IG wave with frequency Δf. Figure 2.3 below shows the variation of the pressure coupling coefficient D_p for a water depth of 13m with f and $\Delta\theta$ for a fixed Δf of 0.03 Hz.

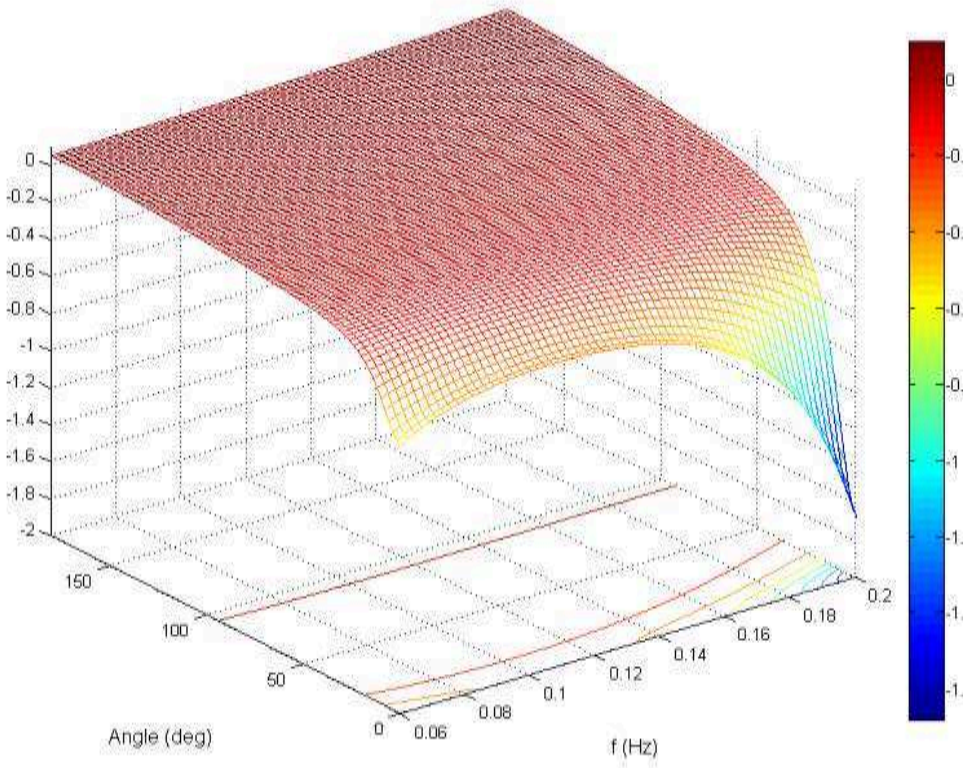

Figure 2.3: The variation of the bottom pressure coupling coefficient D_p with the frequency f and the direction $\Delta\theta$ for a depth of 13m for a fixed Δf of 0.03 Hz

Similarly to the surface elevation coupling coefficient, it shows that the interaction is higher when the interacting frequencies are low, and the difference in directions is low. Typically this corresponds to swells which have frequencies and directional spread.

It should be noted that the bound IG fields calculated from both the surface elevation and pressure coupling coefficients is based on the assumption that the short wave groups and bound long waves are in equilibrium, and therefore are 180° out of phase. This assumes a stationary wave field over a flat bottom.

Being a function in 4 dimensions (f_1, f_2, θ_1 *and* θ_2), computing the coupling coefficient can become numerically expensive, particularly for finer discretisation. However, if the angular and frequential discretisation and depths are kept constant, the coupling coefficient array should remain the same and could be pre-calculated, stored and used throughout similar runs.

2.1.3 Bound Infragravity Energy spectrum

In a natural, directional sea the total long-wave energy becomes the sum of contributions from all pairs of frequencies. Neglecting interactions involving primary waves with frequency less than Δf, the spectrum corresponding to bound IG (with only the difference frequencies retained) is given by (Herbers 1994)

$$E_{forced}(\Delta f) = \int_{\Delta f}^{\infty} df \int_{0}^{2\pi} d\,\theta_1 \int_{0}^{2\pi} d\,\theta_2 D^2(f+\Delta f, -f, \Delta\theta+\pi) E(f+\Delta f, \theta_1) E(f, \theta_2) \quad (2.13)$$

Figure 2.4 below shows an example of such a spectrum calculated from a measured directional energy spectrum and the corresponding IG spectrum. The measurement is from a wave-rider buoy in the Iroise Sea, deployed in a water depth of about 35m.

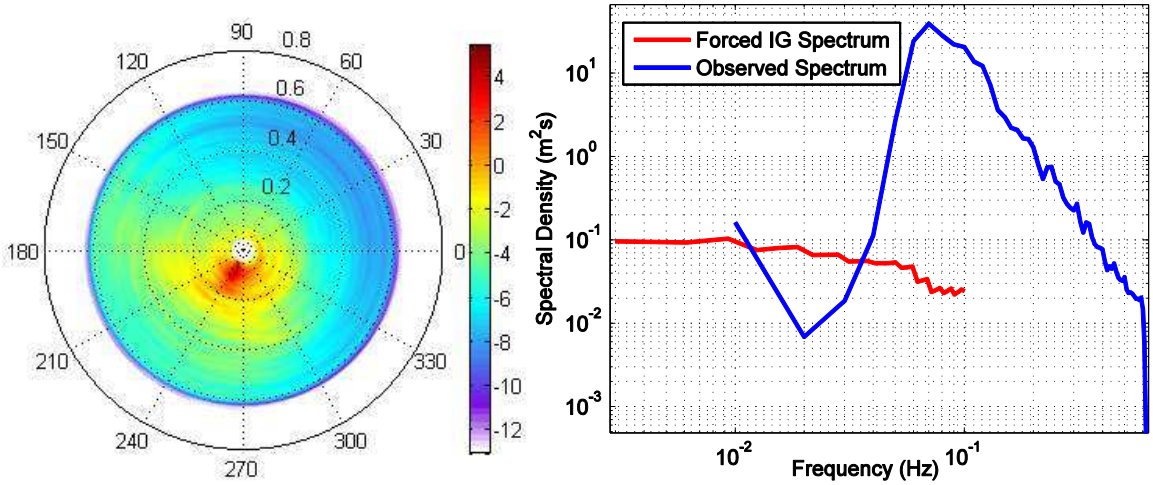

Figure 2.4: The directional spectrum from a measured directional surface elevation spectrum (left , in log.m²s.rad⁻¹) and the computed forced-IG spectrum (right) for a depth of 35m.

The direction of each bound IG component is calculated from the propagation vectors $\boldsymbol{k_1}$ and $\boldsymbol{k_2}$. It should be noted that the propagation direction of the IG waves does not correspond to the difference direction $\Delta\theta$. The angle of propagation corresponds rather to the vector difference

$$\vec{k}_{IG} = \Delta\vec{k} = \vec{k}_2 - \vec{k}_1 \quad (2.14)$$

This can then be implemented as

$$\begin{pmatrix} \Delta k \cos\theta_{IG} \\ \Delta k \sin\theta_{IG} \end{pmatrix} = \begin{pmatrix} k_2 \cos\theta_2 - k_1 \cos\theta_1 \\ k_2 \sin\theta_2 - k_1 \sin\theta_1 \end{pmatrix} \quad (2.15)$$

And then subsequently solved for θ_{IG}

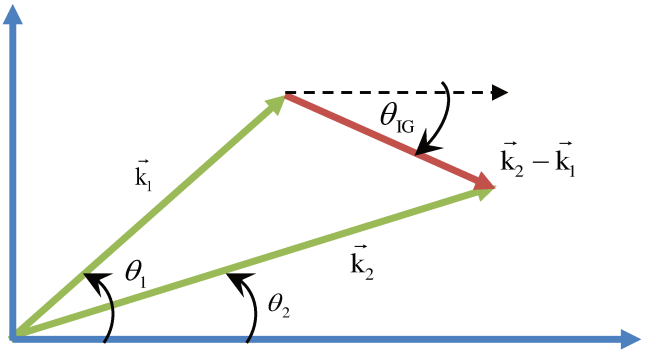

Figure 2.5: The Wave number vectors of two short-wave components, the resulting longwave vector and their associated angles

It should be noted that two interacting wave components contribute to only one infragravity wave frequency and direction. However, one infragravity wave component may be forced by many different short wave interactions.

- Computation of Directional IG spectra

Implementing the computation of the directional spectrum was done in MATLAB, as a development of the previous non-directional routine. Runs for several artificial and measured input spectra were carried out and the resulting spectra are shown

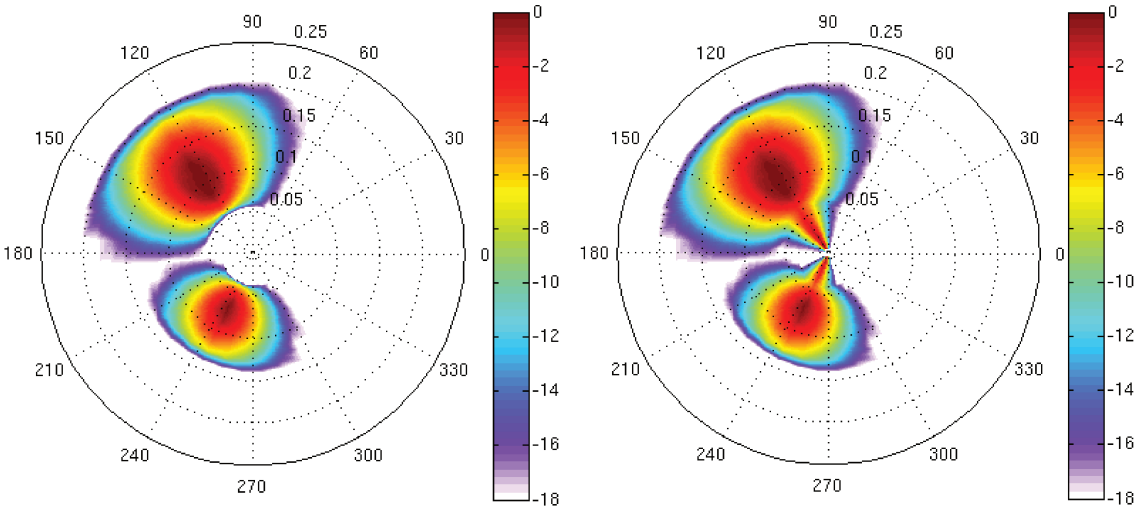

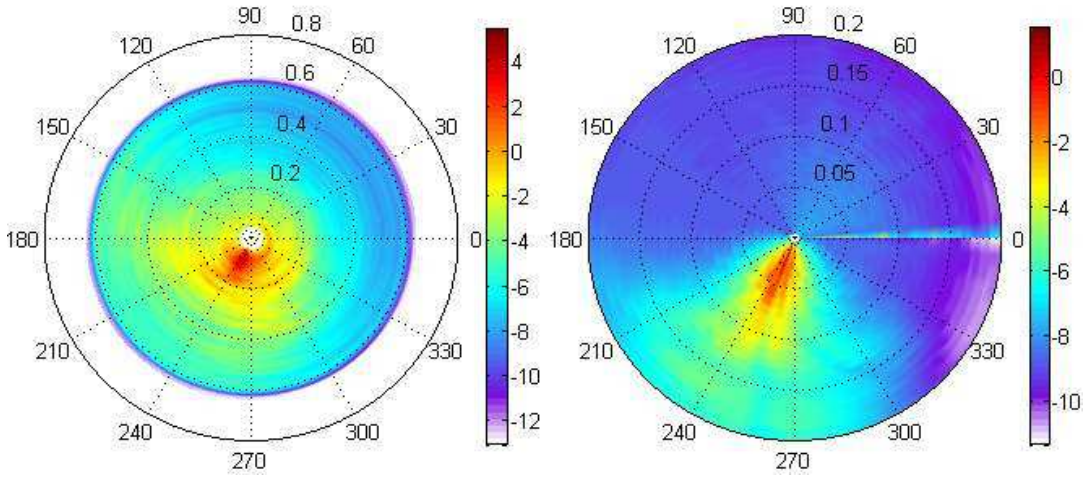

Figure 2.6: The directional frequency-energy input spectra (on the left) and the corresponding directional bound IG output spectra (right) for an artificial spectrum with 2 swell components (top) and a measured spectrum (bottom) in log.m^{2}s.rad^{-1} for a depth of 13m.

It can be observed that as expected, the bound IG waves tend to form in the same directions of the forcing waves, and lower input frequency components tend to produce a higher IG response than higher frequencies. Also, lower directional spreads ($\Delta\theta$) tend to produce higher IG response. All these effects are linked to the form of the coupling coefficients.

2.1.4 Bound IG calculations using the Hamiltonian formulation

Another method for calculating the 2nd order response was constructed by Janssen, (2009) based on the consequences of the canonical transformation in the Hamiltonian theory of water waves (Zakharov and Kuznetsov, 1997). Using Krasitskii's canonical transformation (Krasitskii, 1994) general expressions for the second-order wavenumber and frequency spectrum sea surface were derived. Apart from 'minus' and 'plus' interactions, Stokes-frequency correction, Nonlinear and quasi-linear corrections are also included.

The method was numerically tested with 'minus' interaction, with identical results with the 2nd order coupling coefficients. The detailed theoretical background and explanation on the methodology used can be found in Jansen (2009).

2.1.5 Bound IG over a sloping bottom – Growth Rates

As noted earlier, the bound IG energy calculated through the 2nd order coupling coefficients or the Hamiltonian formulation is based on the assumption that the short wave groups and bound long waves have reached equilibrium on a flat bottom. This is usually characterized by the forced waves being in exact phase opposition with the short-wave groups. This state can be considered as a maximum attainable level. In

general the bottom is not completely flat. On a sloped bottom, or a narrow flat shelf, the equilibrium might not be reached and bound IG energy is probably going to be less than that maximum value. In fact in such cases we might not really refer to these long waves as forced or bound waves but rather as subharmonics.

For sloping profiles, this bound IG level is expected to be less as the transfer of energy from short waves to IG waves is dependent on the slope of the profile, where a mild slope creates a larger transfer than a steep slope (Reniers et al., 2010). Also, the wider the shelf, the more time there is for non-linear interactions between short waves to occur, and reach the equilibrium limit (Battjes et al., 2004). Hence both the bottom slope and the shelf width is going to affect the level generated subharmonics.

On sloping bottom, the subharmonics are influenced by non-linear shoaling as investigated by Battjes et al. (2004). Instead of being in exact phase opposition, there exist a phase lag of the incident subharmonics behind the short-wave groups, which has a role in the transfer of energy between the grouped short waves and the shoaling long waves.

The phase lag appears to increase with increasing frequency, which is reflected in a frequency-dependent growth rate, varying from Green's law free-wave variation of $D^{-1/4}$ for the lower frequencies to the $D^{-5/2}$ shallow-water limit for forced sub-harmonics (Longuet-Higgins and Stewart, 1962, 1964) for the higher frequencies. This observed frequency dependence was also tentatively generalized to a dependence on a normalized bed slope, β (defined in the next section), by Battjes et al. (2004) and Dongeren et al. (2007).

2.2 Generation of Free IG waves

Two main generation mechanisms of free IG-waves are currently recognized, one by the liberation of forced waves and the second by the moving of breakpoint position in wavegroups. Although observations of the directional properties of infragravity waves radiated from shore are in agreement with Longuet-Higgins and Stewart's hypothesis for at least some categories of coastlines (Herbers et al 1995b), the role of wave-breaking and associated set-up variations in the infragravity wave generation process is still poorly understood.

2.2.1 Generation of free waves by liberation of bound IG-waves

The first mechanism is the release of bound IG-waves in the surf zone. Based on observations by Munk (1949) and Tucker (1950), Longuet-Higgins and Stewart (1962) suggested that as the incident short-wave propagates shoreward they are dissipated in the surf zone, mostly through breaking. The bound Infragravity waves associated to the wave groups are then released as free waves, and reflect from the beach and propagate seaward over the continental shelf as shown in Figure 2.7.

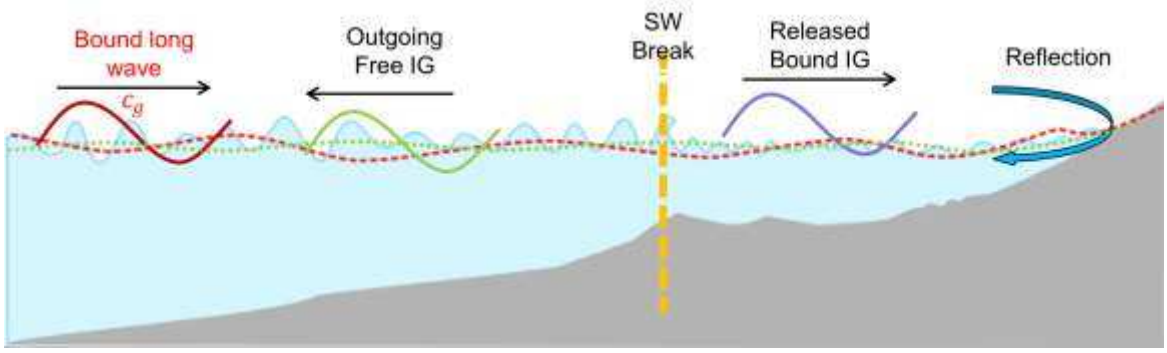

Figure 2.7 IG wave generation by the liberation of bound-IG waves.

Although numerous field measurements confirm this hypothesis, the actual release mechanism can be instigated by several factors. For example Toledo et al. (2012) proposed the release mechanism to be governed by a class II Bragg interaction where there is resonant wave-wave and bottom topography interaction.

2.2.2 Generation of free waves by a moving breakpoint

Alternatively, Symonds et al. (1982) suggested that slow oscillations in the wave setup, associated with slow variations of the breakpoint location of groupy incident swell, can drive free infragravity waves. As the waves break, a strong gradient in the radiation stress develops due to the dissipation of wave energy. This radiation stress gradient results in a set-up at the shoreline, whereby higher waves result in a greater set-up than relative low waves.

Due to the group structure of the incident waves and the resulting time-varying breakpoint, the resulting set-up is not constant but varies on the time scale of the wave. This time varying set-up then propagates freely shoreward as an IG-wave. In addition to this shoreward propagating free IG-wave, a seaward propagating free IG-wave which is out of phase with the wave groups is also generated (Baldock, 2006) as shown in Figure 2.8

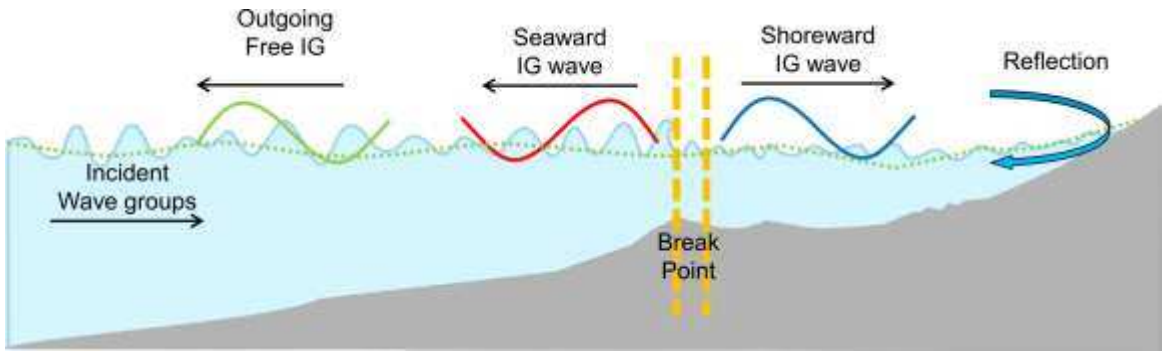

Figure 2.8 IG wave generation by the time-varying berakpoint mechanism (Symonds et al., 1982).

Analysis of field observations and flume experiments showed the relative importance of

the two generation mechanisms. For relativly mild slopes, both field (Herbers et al., 1995a; Ruessink, 1998) and flume (Janssen, 2003) observations showed the dominance of free IG-waves generated by the release of bound IG-waves. In contrast, flume experiments with a steep slope (1:10) showed a dominance of free IG-waves generated by the time-varying breakpoint (Baldock et al., 2000). Schäffer (1993) gave formulations for the combination of both mechanisms. The delineation between these two mechanisms can also be linked to the normalized bed slope β as explained in the next section.

2.2.3 Shoreline reflection of long waves

After having been generated by either mechanism, free IG waves propagating toward the shoreline can be reflected backward. As explained by Battjes et al. (2004), a given bed slope is going to appear steeper to longer waves than to shorter waves, because the longer waves will experience a greater change in depth within a wavelength than the shorter ones. Hence a dimensionless parameter, the normalized bed slope β, was introduced which expresses the relative depth change per wavelength. It can be written as h_x/kh, in which h and h_x are characteristic values of depth and bed slope in the local region considered. $k = \omega/c_g$ is the wave number and $\omega=2\pi f$. Approximating c_g as $\sqrt{(g/h)}$ it can be simplified as

$$\beta_h = \frac{h_x}{\omega}\sqrt{\frac{g}{h}} \tag{2.16}$$

Usually h is chosen at the depth at the mean breakpoint position and noted as h_b. This parameter is related to the surf similarity parameter ξ (Battjes, 1974) as

$$\xi = \sqrt{2\pi}.\,\beta_H \tag{2.17}$$

where H is taken as the incoming wave height near the shoreline. Another parameter that is closely related to β is the normalized surf zone width as defined for a plane slope by Symonds et al. (1982) in the context of a breakpoint generation model.

$$X = \frac{\omega^2 h_b}{g h_x^2} \tag{2.18}$$

For short waves , Battjes (1974) found a relation between the reflection coefficient at the shoreline R and the surf similarity parameter, which can be simplified as

$$R = 0.1\pi\beta_H^2 \tag{2.19}$$

This relationship was found by Battjes et al. (2004) to apply to low-frequency waves as well, governing the reflection of incoming IG waves from the shoreline; the shoreline reflection being smaller for milder slopes and higher frequencies. The outgoing IG wave energy E_{out} is hence related to the incoming IG energy E_{in} by

$$E_{\text{out}} = R^2 \,.\, E_{\text{in}} \tag{2.20}$$

It is hence expected to find an f^{-4} dependence of the outgoing IG wave from the incoming IG energy

$$E_{out}(f) \sim \frac{1}{f^4} \cdot E_{in}(f) \tag{2.21}$$

2.2.4 Delineation between 'regimes'

The normalized bed slope β can also be used to mark the delineation between two slope 'regimes': a steep-slope regime for β >0.3 and a mild-slope regime for β <0.06 (Battjes et al., 2004).

The steep-slope regime seems to give rise mostly to the break-point generation mechanism of IG waves as well as a small offshore IG growth rate and strong reflection at the shoreline.

On the other hand, the mild-slope regime seems to harbour the liberation mechanism with higher bound wave shoaling and a weak coastline reflection with IG wave breaking.

2.3 Free infragravity Waves

After having been generated, the IG waves (partially) reflect at the beach and subsequently propagate in the seaward direction. Depending on the initial propagation direction in shallow water, these waves may either radiate to the open ocean as leaky waves, or reflect back towards the shore from turning points on the sloping beach and shelf. They are then known as edge waves. The simultaneous presence of incoming and outgoing IG waves can also result in a standing IG wave pattern between the surf zone and the shoreline.

2.3.1 Free Edge waves

Edge waves are three-dimensional waves trapped against the nearshore by successive reflection and refraction. They can propagate alongshore (progressive edge waves) or be long-shore-standing (standing edge waves). They usually have a finite number of nodes in the cross-shore direction, and a theoretically infinite number of nodes/antinodes in the long-shore dimension.

Observed infragravity energy levels on the beach, shelf and in the open ocean are qualitatively consistent with strong refractive trapping and a relatively weak leaky component (e.g., Webb et al. , 1991; Okihiro et al. , 1992; Herbers et al. , 1995a). However, when local swell energy levels are high, seaward propagating waves dominate the infragravity band, suggesting that free waves radiated from shore are under normal conditions significantly damped before reaching their turning point on the shelf (Elgar et al , 1994; Herbers et al. , 1995).

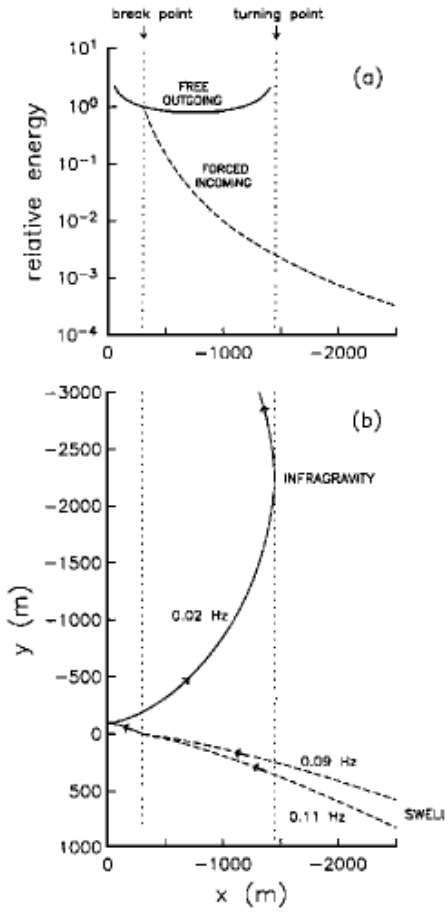

Figure 2.9: Illustration of generation of free IG by the liberation mechanism and subsequent liberation, reflection and trapping (adapted from Herbers et al , 1994).

2.3.2 Free Leaky waves

While infragravity waves radiated from shore are predominantly trapped on the shelf, a relatively weak leaky component propagates into the deep sea. Webb et al. (1991) showed that free infragravity waves observed in the open ocean are the weak background radiation from distant shores where incident swell and infragravity wave energy levels are high. The estimation of the amount of IG energy that manages to leak from the shoreline is also poorly known. Herbers et al. (1995a) and Evangelidis (1996) showed that the amplitude of the leaky waves have a variation of $D^{1/2}$ rather than the Green's law free-wave variation of $D^{1/4}$ (linear de-shoaling). It was suggested that the additional $D^{1/2}$ variation was due to the trapping effect.

A first empirical approximation was formulated by Vis et al. (1985) who proposed the IG wave height, H_{IG} radiated from the shore to be

$$H_{IG} \approx 0.08 \left(\frac{H_s \, T_p}{D} \right)^2 \tag{2.22}$$

Where H_s is the significant wave height of wind seas and swells and T_p is the peak

period.

Ardhuin et al. (2014) developed an empirical source of offshore free IG waves, which was inferred from coastal measurements in Hawaii, North Carolina and France. Based on these datasets, H_{IG} radiated from the shoreline was successfully approximated by

$$H_{IG} \approx \alpha_1 H_s T_{m0,-2}^2 \sqrt{\frac{g}{D}} \tag{2.23}$$

Where $T_{m0,-2}$ is the mean period given by the -2 and 0 moments of the surface elevation spectrum, g is the apparent acceleration of gravity, D is the local mean water depth, and α_1 is a dimensional constant. The observation analysed by Ardhuin et al., (2014), shows that, within a factor of 2, α_1= 12x10-4 s-1. This empirical formulation will be discussed in detail in upcoming chapters.

2.3.3 Far-IG waves

Free infragravity motions on the continental shelf are either waves radiated from nearby beaches, where they are generated, or can be remotely generated waves arriving from the open ocean. These distant (trans-oceanic) sources appear to dominate the infragravity wave field on the shelf during extremely calm conditions when the generation of infragravity waves on nearby beaches is relatively weak (Herbers et al., 1995a, b).

In contrast to the directional broadening and trapping of waves radiated from local shores, remotely generated waves traveling into shallow water refract towards propagation directions that are perpendicular to the shoreline, causing a directionally narrow, shoreward propagating wave field close to shore. They can also have another signature because of the dispersion relation where the lower frequency free IG arrive earlier than the higher frequencies as shown in Figure 2.10 below, which is a spectral time series of pressure measurements at 166m depth off the north of Waimea, Hawaii.

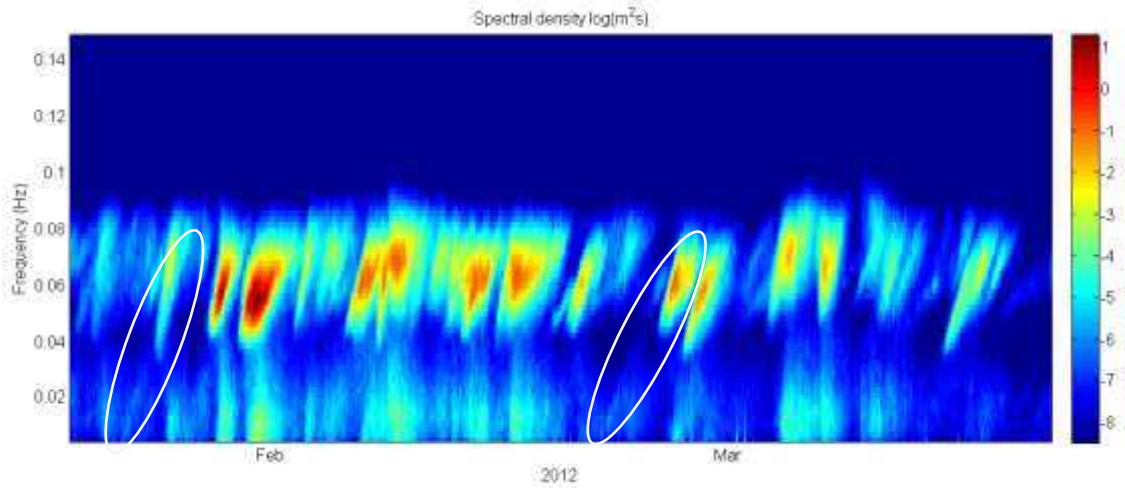

Figure 2.10 Spectral time series of bottom pressure at 166m depth off Waimea during the beginning of 2012 showing IG signal from far sources (denoted by white ellipses). Vertical slopes are believed to be locally generated IG.

This is rarely visible because the local sea state is rarely calm enough not to generate local IG in a certain time widow for the distant source to be visible.

Upon reflection from the beach these waves may propagate back to the open ocean or become trapped on the shelf if the shelf is not regular. Observed directional spectra of infragravity waves on the shelf during low wave conditions are indeed bimodal with narrow peaks in shoreward and seaward directions, in contrast to the broad directional spectra (with significant alongshore propagation) typically observed during high energy conditions (Herbers et al., 1995a). It is probably this re-reflected IG that contributes to the ambient IG noise levels in oceanic basins as suggested by the acoustic analogy of sound intensity in an enclosed room (Munk , 1963).

2.3.4 Dissipation of IG

Dissipation of oceanic free IG waves remains poorly understood, but it is widely believed to occur principally in coastal regions due to shelf/coastal absorption processes. This was investigated by Rabinovich, et al., (2013) in the context of tsunami waves. Rawat et al., (2014) also suggested this conclusion to be valid for IG waves.

Possible dissipation mechanisms include bed friction, breaking and energy transfer to short waves . Henderson and Bowen (2002) attributed the observed shoreline dissipation of long-wave energy to bottom friction. This is particularly important in case of an extensive flat and shallow region, such as a coral reef (Pomeroy et al., 2012), but less significant on sloping beaches (van Dongeren et al., 2007; Henderson et al., 2006), where the main cause was rather attributed to the nonlinear transfer mechanism through triad interactions from low-frequency energy to higher-frequencies.

Battjes et al. (2004) found that the normalized bed slope parameter, β also governs dissipation at the shoreline. For large values of β (steep-slope regime), long waves were

shown to be almost fully reflected from the shoreline, while for small values of β (mild-slope regime) reflections at the shoreline are small as the long waves tend to break.

Battjes et al. (2004) also found that the conventional criterion used to distinguish breaking and nonbreaking short waves on a slope was also applicable to low-frequency waves near the shoreline. It was hence suggested that the observed energy losses are due to the breaking of the long waves. This hypothesis was further substantiated by van Dongeren et al. (2004). Based on a numerical study, Ruju et al. (2012) suggested that nonlinear interactions are strongest in the outer surf zone, whereas IG-wave breaking appears to be the dominant process in the inner surf zone.

3 Modelling of IG Waves with Phase Resolution

In this chapter a review of existing models to study certain aspects of IG wave generation and propagation in coastal areas is presented. Several hypotheses concerning the generation, liberation and propagation of IG waves are going to be tested, which will then be used to define parametrizations in a phase-averaged global model.

Several types of numerical models are available to study IG-waves. IG-waves can be modelled by phase-resolving models based on a Boussinesq type formulation (e.g Madsen et al., 1991), Reynolds Averaged Navier Stokes (RANS) type formulation (e.g. Lin and Liu, 1998) or a non-hydrostatic approach (e.g. Stelling and Zijlema, 2003). These phase-resolving models account for all relevant near-shore processes such as shoaling, refraction, reflection, and non-linearity. They thereby provide a potentially accurate approach, but which might be computationally expensive.

Alternatively, 'Surf-beat models' simulate IG waves by combining a wave driver model, which provides the forcing of the wave groups, with a shallow water model that accounts for the near-shore transformation of the IG waves (e.g. (Roelvink et al., 2009a)).

3.1.1 Boussinesq-type models

Boussinesq-type models are based on the Boussinesq approximation for water waves (Boussinesq, 1872). At their core, the equations are the depth-integrated shallow water equations for non-dispersive linear wave propagation. The basic foundation is extended by the addition of terms which include the lowest order effects of nonlinearity and frequency dispersion. This includes a polynomial approximation to the exact dispersion relation $(2\pi f)^2 = gk \tanh(kD)$. This matches well only in shallow waters making the equations invalid for intermediate and deep waters.

Improvements in model applicability have been obtained using higher order of approximation for frequency dispersion effects (e.g Madsen et al., 1991). Also the use of either progressively higher order truncated series expansions (Gobbi et al., 2000 and Agnon et al., 1999) or multiple level representations (Lynett and Liu, 2004), have allowed their application to the entire shoaling zone or deeper. Also fully-nonlinear formulations have been developed (eg Wei et al., 1995 and Madsen et al., 2003)

Boussinesq wave models have become a useful tool for modeling surface wave transformation from deep water to the swash zone, as well as wave-induced circulation inside the surfzone. Both the primary waves and the low frequency waves are calculated with full phase resolution. Examples include MIKE 21 BW (Madsen and Sørensen, 1993), TRITON (Borsboom et al., 2001) and FUNWAVE (Shi et al., 2012), which have been extensively used. A major inconvenience of Boussinesq-type models is that they are

expensive. Short waves are solved individually and therefore the grid resolution should be small.

3.1.2 Non-hydrostatic models

Non-hydrostatic models also solve the free-surface flow equations but only for a number of discrete horizontal layers. They differ from classical Navier-Stokes models in that the free surface is described by a single valued function that allows them to efficiently compute free-surface flows (Stelling and Zijlema, 2003). Furthermore their implementation is usually less complex compared to Boussinesq models hence there is an improvement in terms of robustness and maintenance. As with Boussinesq-type models, there is also an approximation of the dispersion relationship which can be improved by increasing the number of vertical layers.

Their nonlinearity allows a representation of free and bound waves. Computationally the cost of non-hydrostatic models is however comparable with that of the Boussinesq-type models. It is this approach that has been implemented in the SWASH model (Zijlema et al., 2011), which will later be described.

3.1.3 Surf-beat models

Surfbeat models are basically shallow-water models forced on wave group scale. A wave driver model provides the forcing on a primary wave group scale through the radiation stress and the shallow-water model generates and propagates the infragravity waves. These models are computationally efficient since individual short waves don't need to be resolved but information on their phases is hence also not provided. However, the phases of the short waves are not necessary for the purpose of this study. These models are able to resolve both bound and free IG waves with their proper phases. However as the long waves are computed with shallow water approximation, they are not frequency-dispersive. This is not expected to have a major impact in the context of regional IG modelling.

Examples of surfbeat models are IDSB (Reniers et al., 2002) and XBeach (Roelvink et al., 2009). XBeach will be used later in this chapter and should provide a fairly accurate, and computationally less expensive approach to study IG waves near the coast.

3.2 Modeling IG waves using SWASH

SWASH (Simulating WAves till SHore) is a hydrodynamic model for the simulation of non-hydrostatic free-surface flows. It is based on the nonlinear shallow water equations including non-hydrostatic pressure, which are derived from the incompressible Navier-Stokes equations describing conservation of mass and momentum.

Zijlema et al. (2011) successfully simulated IG waves by comparing SWASH predictions with the analytical finite depth equilibrium solution of Longuet-Higgins and Stewart

(1960) and with the laboratory observations of Van Noorloos (2003). Furthermore, Rijnsdorp et al., (2014) demonstrated that SWASH is able to reproduce most of the processes commonly associated with the evolution of IG waves near the shore. These include the shoaling of bound IG waves, shoreline reflections, the phase lag between the wave envelope and the incoming IG waves, nonlinear interactions and even the occurrence of IG wave breaking.

3.2.1 Bichromatic waves over a sloping bottom

We start our investigation with the use of SWASH in a 1D mode to briefly and qualitatively investigate the generation, evolution and liberation of IG waves from incoming short waves . The non-hydrostatic option was used with a second-order weakly-reflective wavemaker, based on weakly nonlinear wave theory, in order to include the incident (bound) IG wave contributions. The waves are considered to be unidirectional and the non-hydrostatic equations (Zijlema et al., 2011) therefore presented in a two-dimensional vertical plane bounded by the free surface and the bottom. To avoid the accumulation of IG energy in the domain, outgoing IG waves at the input boundary are absorbed in SWASH by nullifying the velocity due to this motion in the incident velocity signal (Rijnsdorp et al., 2014).

Firstly the model was forced at the seaward boundary with a finite series of short wave (Hs of 5m and mean period of 10s) groups, and their evolution was analysed in space and time (Figure 3.1)

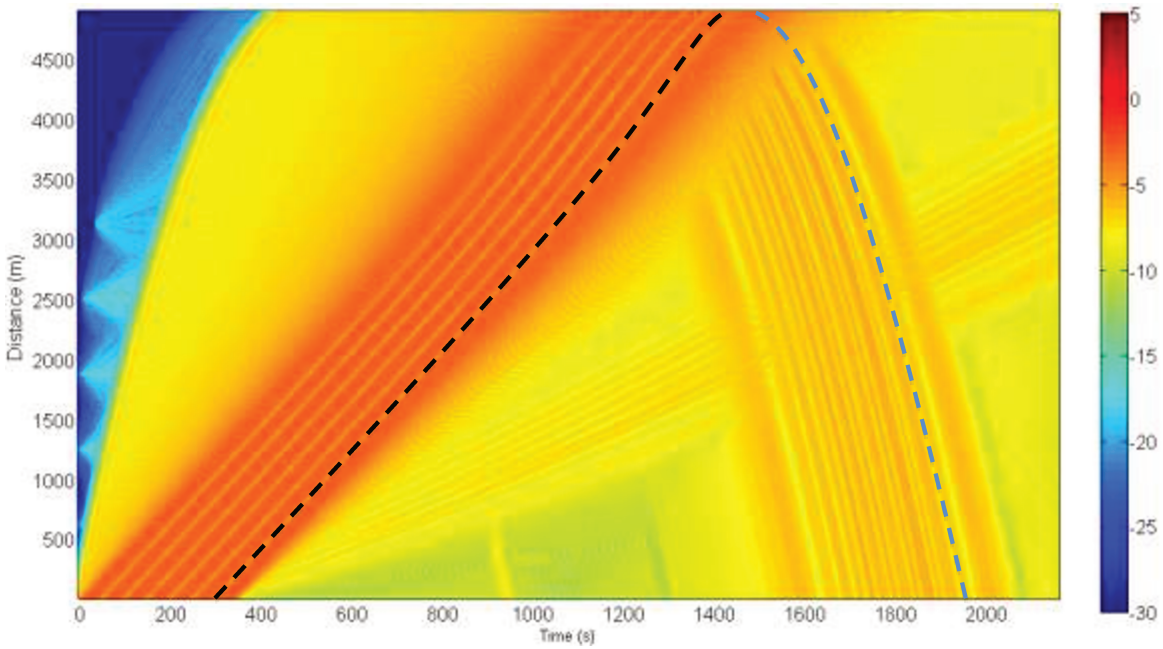

Figure 3.1: Simulated propagation of 7 regular wave-groups on a 1% sloping bottom, showing the formation of bound IG, the dissipation of the wave groups and the conversion of the group envelopes into free IG waves. The shore is centered at the 5000m position. The color-scale represents the absolute displacement of the free surface in log (m). Notice the different propagation speeds of the incoming wave groups (black dashed line) and the outgoing free IG waves (grey dashed line).

The wave groupiness is conserved up to the dissipation of the short-waves and then give rise to the free waves which propagates at different speeds than the incomming wave groups. However the exact free IG generationg mechanism (forced-IG liberation or varying breakpoint position) cannot be distinguished. The different propagation speeds of the incoming wave groups (black dashed line) and the outgoing free IG waves (grey dashed line) can be also noted.

3.2.2 General case: Oblique waves on a uniform slope

Here a 1D uniform slope configuration is forced by a parameterised short wave spectrum (JONSWAP) provided at the seaward boundary. A Fourier analysis is performed on each grid point to obtain the surface elevation spectral densities E(f). The total wave height (Hs) is then calculated by integrating E(f) over the complete frequency band and the wave height due to low frequency motions (H_{IG}) over 0.004Hz to 0.04Hz with

$$H_{IG}(x) = 4\sqrt{\int_{f_{min}}^{f_{max}} E(x,f)df} \tag{3.1}$$

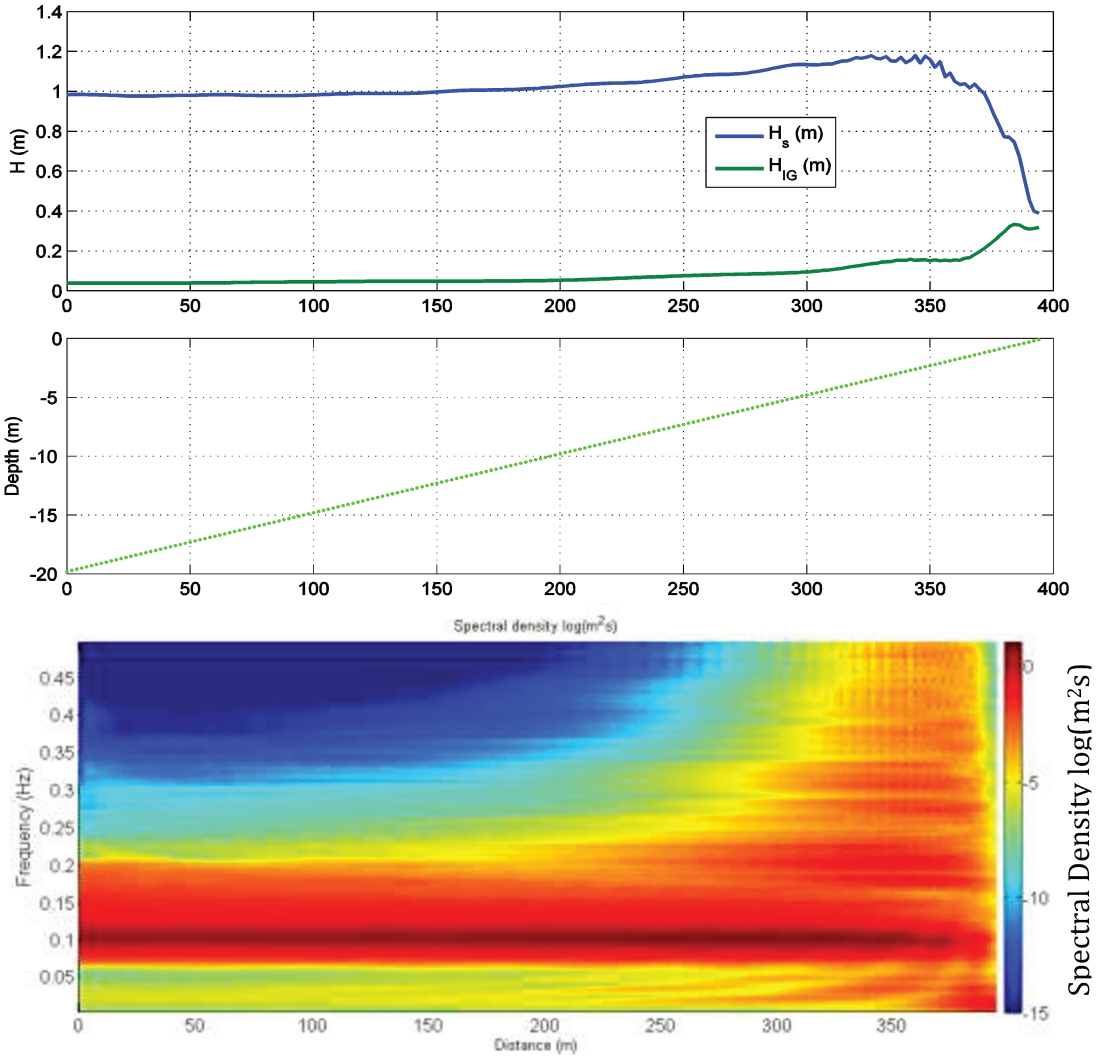

Figure 3.2: Output of 1D modeling with SWASH, showing (top) the evolution of wave height (blue line) and the wave height due to low frequency motions (green line) for a stationary 1m, 10s JONSWAP sea on a 5% sloping bottom. The shore is centered at the 400m position and the forcing boundary at 0m. The bottom figure shows the evolution of the frequency spectrum.

The evolution of the spectrum is apparent, with the IG part dominating the swell and sea, as the waves move towards the coastline. The spectrum tends to get 'flat' and the IG proportion tends to become larger than the other components. Several harmonics of the input spectra also appear towards shallow waters. A standing wave node can also be seen in the low frequencies, and its position can be seen varying from being far for the lowest frequencies, to being almost mingled with the beach for the higher frequencies.

However when the experiment is repeated on a 2D configuration, there seem to be an improper absorption of outgoing IG energy at the forcing boundary in SWASH even with the use of sponge layers (absorbing boundaries) as shown in Figure 3.3.

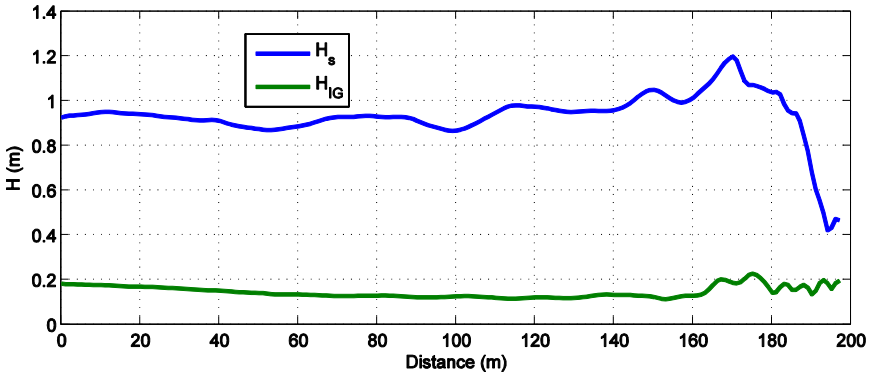

Figure 3.3 Output of 2D modeling with SWASH, showing the evolution of wave height (blue line) and the wave height due to low frequency motions (green line) for a 1m, 12s JONSWAP sea on a 10% sloping bottom showing the accumulation of IG energy near the forcing boundary (on the left).

The nullifying of the velocity due to this motion in the incident velocity signal (Rijnsdorp et al., 2014) seem to be less efficient in 2D configurations compared to 1D. This, together with the high computational cost of SWASH resulted in the choice to test the use of XBeach in order to carry out the rest of the investigation.

3.3 IG wave modeling using XBeach

XBeach, an acronym for 'eXtreme BEACH behaviour model', is a two-dimensional, public-domain wave model developed by Deltares, amongst others with original funding from the US Army Corps of Engineering (USACE) for Deltares, IHE, Delft University of Technology and the University of Miami. It was developed for the computation of natural coastal response during time-varying storm and hurricane conditions, including dune erosion, overwash and breaching (Roelvink et al., 2009). It can resolve wave propagation, long waves and mean flow, sediment transport and morphological changes. The model solves the steady and unsteady (IG) surface elevation and particle velocities from the nonlinear shallow water equations of mass and momentum with radiation stress forcing, cast in a Generalized Lagrangian Mean (GLM) formulation (Andrews and McIntyre, 1978). The model also solves for the wave action and roller energy balance equations (Svendsen, 1984).

The radiation stress forcing is calculated from the wave action equation for the time variation of the short-wave envelope on the wave group scale (cf Appendix I). The underlying assumption is that the short-wave energy propagates at the group speed when the spectra are narrow banded, which has been confirmed experimentally (Janssen et al., 2003). This forcing on the wave group scale generates IG wave motions. The model does not resolve the shape of the short-wave motions. There is also a non-hydrostatic option in XBeach that is similar to a single layered SWASH model. XBeach thus uses a phase average over the short waves but resolves the phase of the long waves. As investigated by (Roelvink et al., 2009a), XBeach is well able to reproduce the infragravity wave spectrum of measured data.

3.3.1 Running XBeach

XBeach requires input of the initial bathymetry and boundary conditions which are generated from offshore (measured or computed) wave spectra (for the wave action equation and time-varying IG motions) and slowly varying (tidal) water levels from measurements or an outer domain model. We refer to Van Dongeren et al., (2003) for details on the boundary condition implementation. To resolve infragravity motions, the wave and roller equations must be solved in non-stationary, wave-group resolving mode. In the present application it is run in a 2D hydrodynamic mode with no morphological change and sediment transport.

The typical approach was to test XBeach forced by a parameterised short wave spectrum (JONSWAP) provided at the seaward boundary on a 10% sloping bottom. The domain is a square with similar spatial resolution in both directions. Results from the profile in the middle of the domain are then extracted. Figure 3.4 shows results for the shortwave heights and free surface. The swash motion due to infragravity waves that are forced by the wave groups and the outgoing free waves can be clearly seen. The ARC switch (active reflection compensation at seaward boundary, van Dongeren et al., 2003) in XBeach seems to play an important role in nullifying the reflection of outgoing IG waves at the input boundary. Here the absorbing boundary includes the incidence angle of the reflected infragravity waves. This compensation is also carried out in SWASH but does not seem to work properly for 2D configurations.

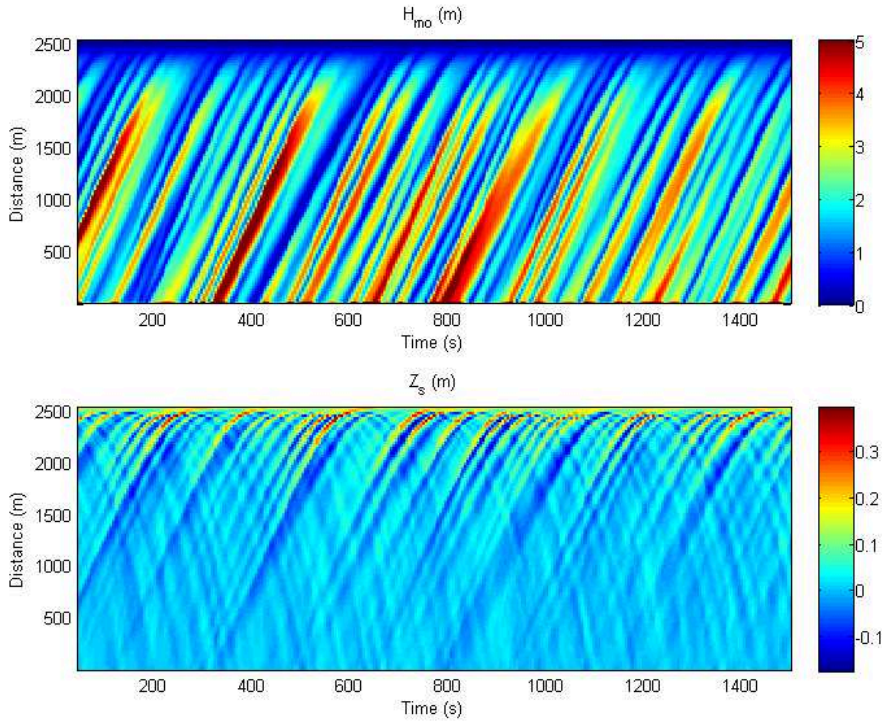

Figure 3.4 Output of XBeach modeling, showing the evolution of Hs (top) and of the free surface due to low frequency motions (bottom) for a 4m JONSWAP sea on a 10% sloping bottom. The shore is centered at the 2500m position.

The different propagation speeds of the incoming (forced) waves and the outgoing free

IG waves can here also be also noted.

With XBeach, the short wave height (Hs) can be simply obtained from the directly outputted $H_{rms.}$ But a Fourier analysis still needs to be performed on each grid point to obtain the low frequency surface elevation spectral densities E(f),which can then be integrated over 0.004Hz to 0.04Hz as previously to obtain H_{IG}.

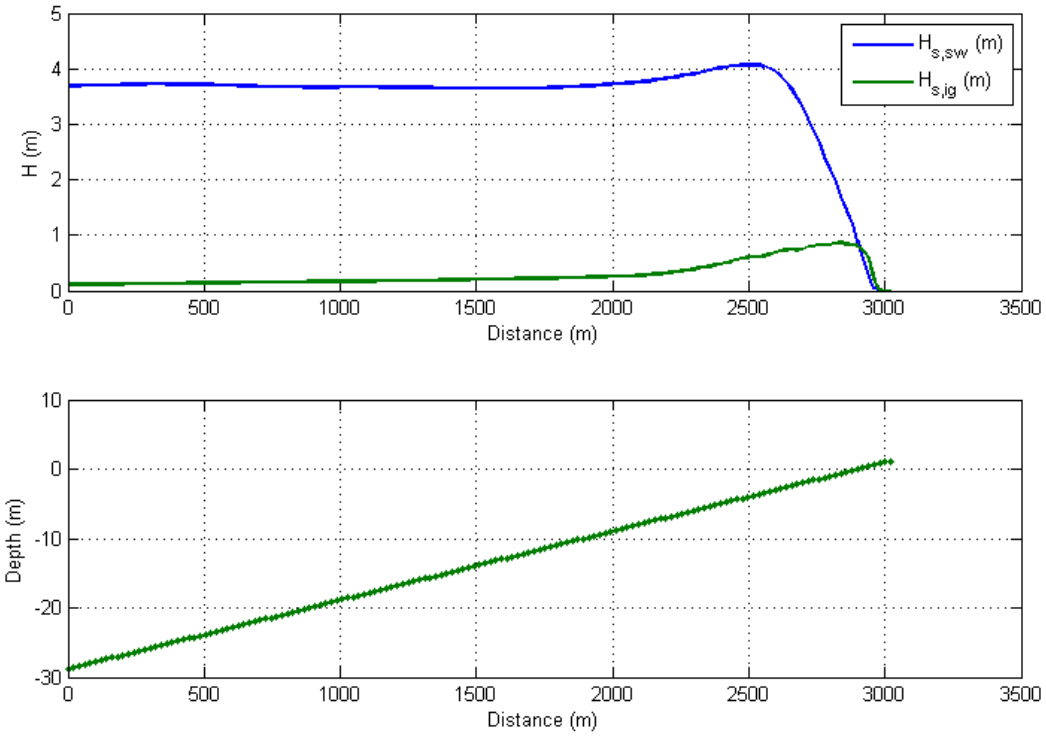

Figure 3.5 Output of 2D modeling with XBeach, showing (top) the evolution of short wave heights (blue line) and the wave height due to low frequency motions (green line) for a 4m, 12s JONSWAP sea on a 1% sloping bottom (bottom profile).

The performance and validation of XBeach in the context of IG waves have been extensively carried out by several teams.

3.3.2 Estimation of incoming and outgoing IG components

In order to properly investigate the outgoing IG energy levels from the surf zone, the proportion of shoreward and seaward IG energy levels must be known. As XBeach does not have an analysis tool to present the bound long wave and the free long wave separately, other methods have been explored.

The output signal can be decomposed by several methods including the 'Array Method', which compares the co-spectra of surface elevations for at least two different locations (eg Dongeren et al., 2007), or the 'collocated method' which decomposes the signal in the time domain based on both the sea surface elevation and velocity time signal of the IG-waves (Guza and Thornton, 1985).

A variation of this latter method would be to analyse the evolution of the directional spectrum. Although this won't allow the complete differentiation of the bound and free components in the spectrum, it should be enough to suit our purpose of estimating the outgoing free IG levels. It will be also simpler to apply to every grid-point along the whole cross-section than the array method.

Since XBeach does not have the option of directly outputting the directional spectrum in the surface elevation (low frequency) space, the spectrum must be calculated from other output variables such as the orbital velocities at the surface and the surface elevation itself. This can be done by using the co-spectra combine with methods such as PUV and UVW, together with the Minimum Entropy (MEM) Method (Benoit et al., 1997). Another method would be to use the bi-spectra (Herbers et al., 1994) to separate forced components, but this method works with a flat bottom assumption and also requires the availability of the short-wave directional spectra.

Here we estimate the directional spectra at each grid point with the PUV co-spectral method, using the horizontal orbital velocities and the vertical displacement of the water surface. Together with the MEM method, this yields $E(x, f, \theta)$. The incoming and outgoing IG levels are then calculated using

$$H_{IG,Shoreward}(x) = 4\sqrt{\int_{180}^{360}\int_{0.004}^{0.04} E(x,f,\theta)df\,d\theta} \tag{3.2}$$

$$H_{IG,Seaward}(x) = 4\sqrt{\int_{0}^{180}\int_{0.004}^{0.04} E(x,f,\theta)df\,d\theta} \tag{3.3}$$

The method seems to work well as shown in Figure 3.6.

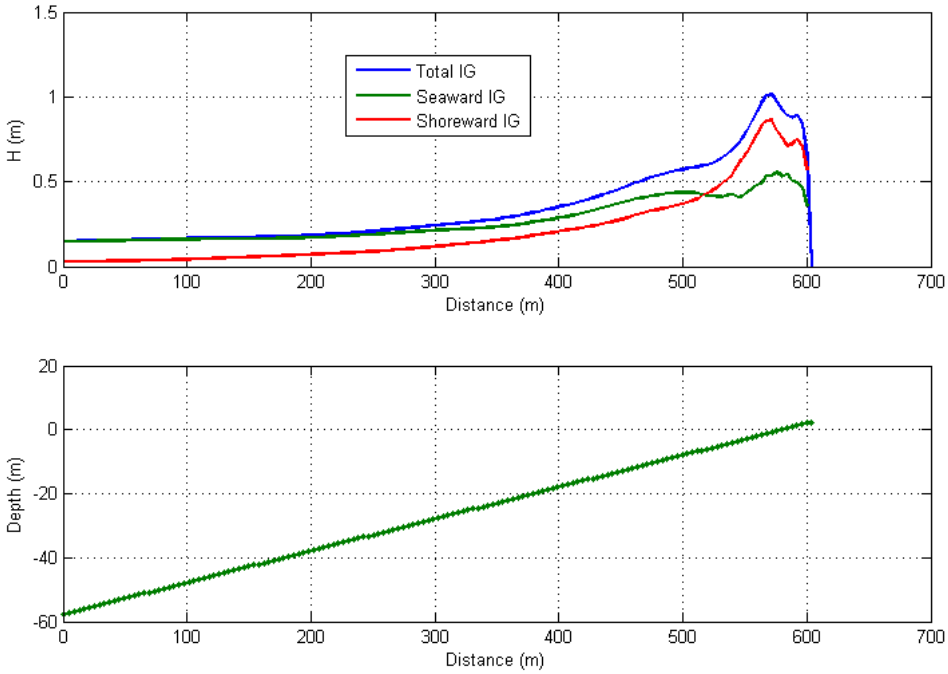

Figure 3.6 Differentiation between incoming and outgoing IG components for a 4m JONSWAP sea (top figure) on a 10% sloping bottom (bottom figure). The shore is centered at the 600m position.

The asymptotic behaviour in deep water is more easily seen with a logarithmic scale (Figure 3.7).

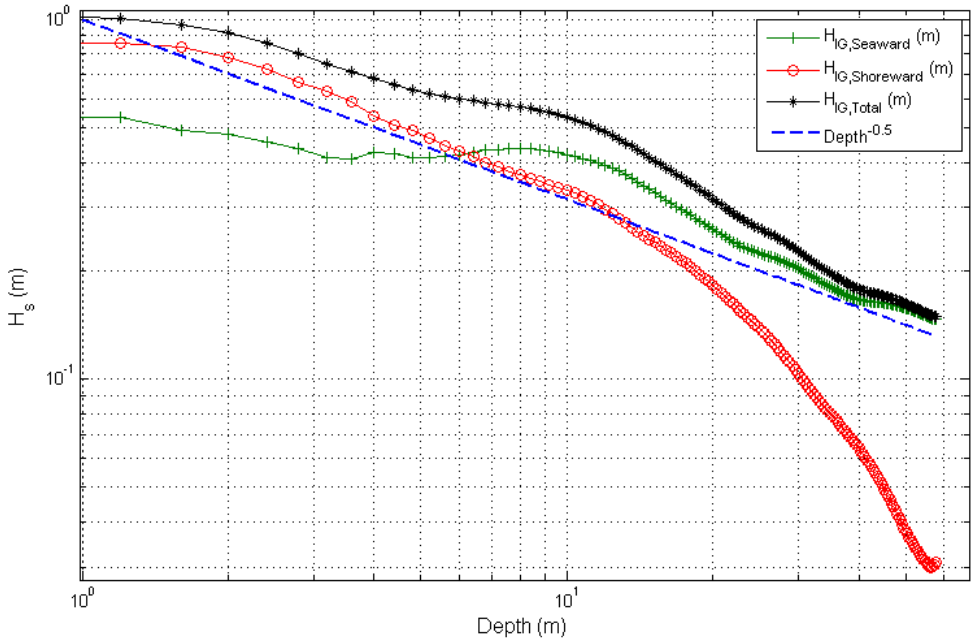

Figure 3.7: Incoming and outgoing IG components in log-log space for a 4m JONSWAP sea on a 10% sloping bottom.

In deeper waters, the shoreward IG, which is assumed to be mostly bound IG is very sensitive to the depth, but not the outgoing free IG (Figure 3.7). The bound IG 'growth'

can be seen (red curve and circles) because it does not follow linear $D^{-1/2}$ shoaling. At some point in shallow waters (around 10m depth), the shoreward IG wave starts to follow a $D^{-1/2}$ shoaling, which suggest that they are now free waves.

Near the shore, the free IG value is approximately constant up to a certain turning point (around 10m depth) and then joins a $D^{-1/2}$ asymptotic de-shoaling behaviour for greater depths.

The model run also duplicates this $D^{-1/2}$ evolution law for the free IG wave heights observed by Herbers (1995a) and Evangelidis (1996) and used in Ardhuin et al. (2014) in the empirical formulation of the offshore IG field. The origin of this $D^{-1/2}$ evolution comes from the conservation of the spectral energy density for waves propagating in two dimensions

$$\frac{d}{dx}\left(\frac{c_g E}{k}\right) = 0 \tag{3.4}$$

Hence

$$\mathrm{E} \sim \frac{k}{c_g} \sim \frac{1}{D} \tag{3.5}$$

And

$$H_s \sim \frac{1}{\sqrt{D}} \tag{3.6}$$

This property of conservation was derived by Longuet-Higgins (1957) and is applicable if the directional spread of the spectrum is large enough, which is the case for IG waves (Herbers et al., 1994)

Also there seem to be a good correlation between IG levels at the intersection of the incoming and outgoing curves and the value of the outgoing IG level further offshore when adjusted by $D^{-1/2}$.

3.3.3 Liberation depth

If we assume IG liberation occurs at the breaking point, then the depth at which this happens will be related to H_s by the classical γ coefficient (Battjes and Janssen 1978) which is a simplification of a formulation by Miche (1944).

$$\gamma = \frac{H_s}{Depth} \tag{3.7}$$

This is a simplification applicable in shallow water depths (when $D/L < 0.04$), as in general this ratio depends on both the wave steepness and the bottom slope. γ is generally assumed to be in the range 0.7 to 1.3. We can now define the coefficient γ_{lib} as

$$\gamma_{lib} = \frac{H_s}{Depth_{IG}} \tag{3.8}$$

$Depth_{IG}$ corresponds to the actual location where bound IG waves are liberated. The aim is to identify this depth location using just a generalized value for γ_{lib} and incoming Hs. From there it would then be easy to deduce HIG using the incoming short waves spectra, and evaluate its outgoing value using $D^{1/2}$ variation. This would later be useful to parameterize the offshore free IG level with the incoming bound IG level, and hence the incoming short waves spectra. From the simulations carried out with XBeach, we have found values of γ_{lib} in the range 0.6-0.8. But this could also depend on other factors such as directional spread. We shall now study the variation of the spectral shapes.

3.3.4 Spectral evolution in the surf zone

If we integrate the directional spectra over only the shoreward and seaward directions, as in (3.2) and (3.3), the shoreward and seaward frequency spectrum can be evaluated at each point of the grid (Figure 3.8). This allows us to study and compare the shapes of the spectra at different positions along the slope, inside and outside of the surf-zone.

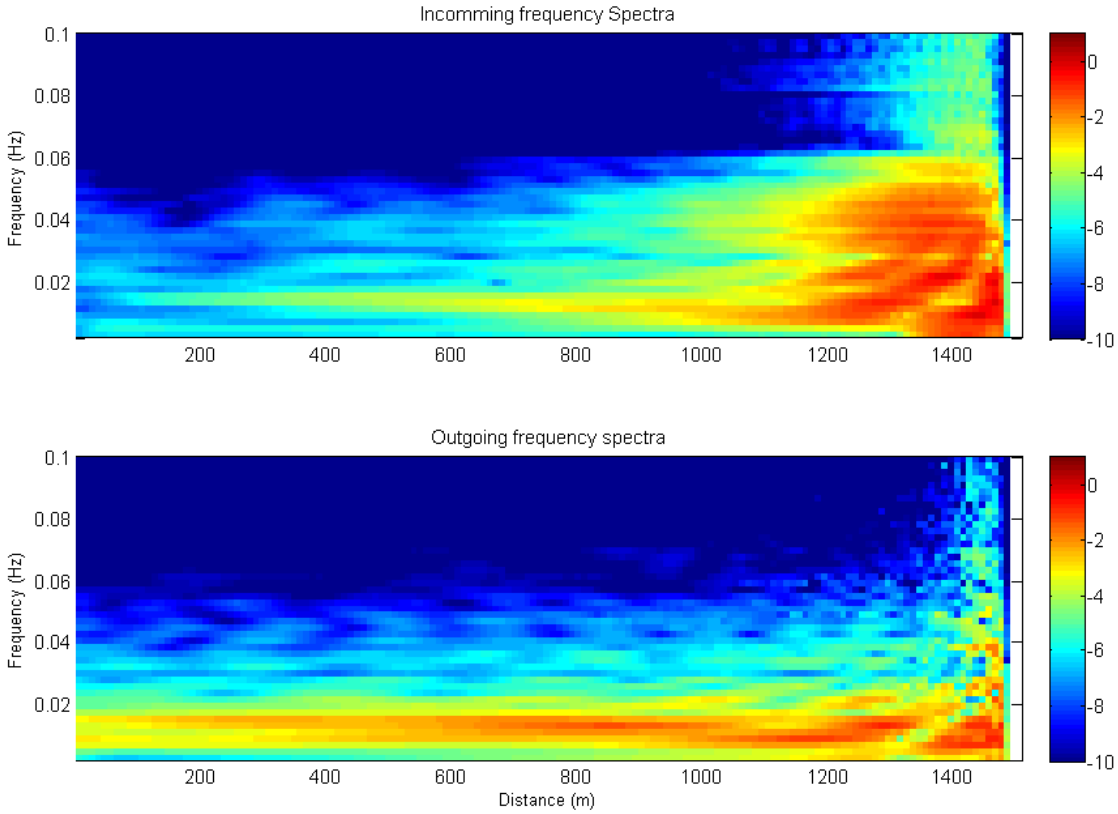

Figure 3.8 Evolution of the frequency spectrum for shoreward (top) and seaward (bottom) travelling low frequency waves from a 4m, 12.5 s JONSWAP sea forcing with a spread of 10 on a 4% sloping bottom. The shore is centered at the 1500m position. The units are in log(m^2s)

The growth of incoming IG waves can be easily seen, from being very low at the incoming boundary to a maximum with an approximately flat spectrum in the surfzone. The variation of the outgoing IG energy seems to be less marked, especially outside the surfzone.

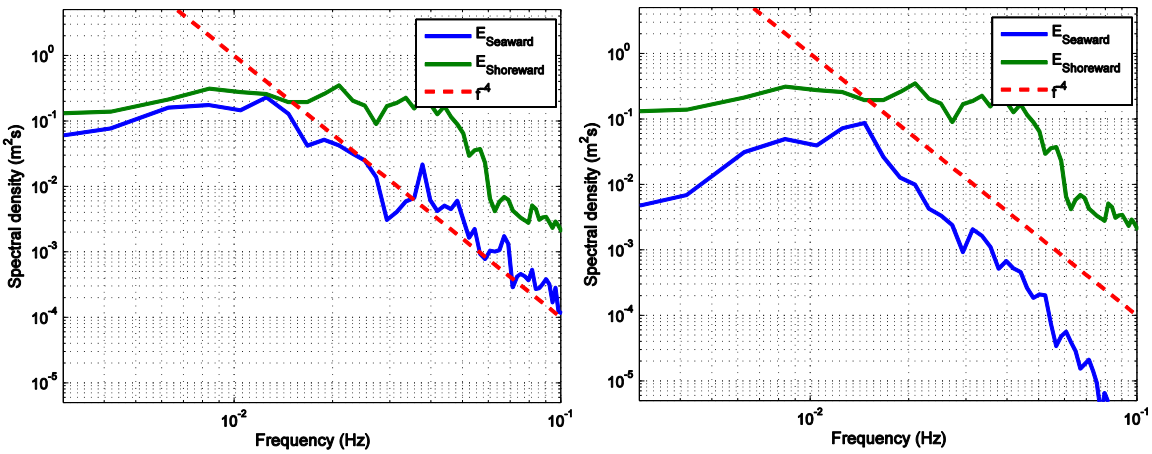

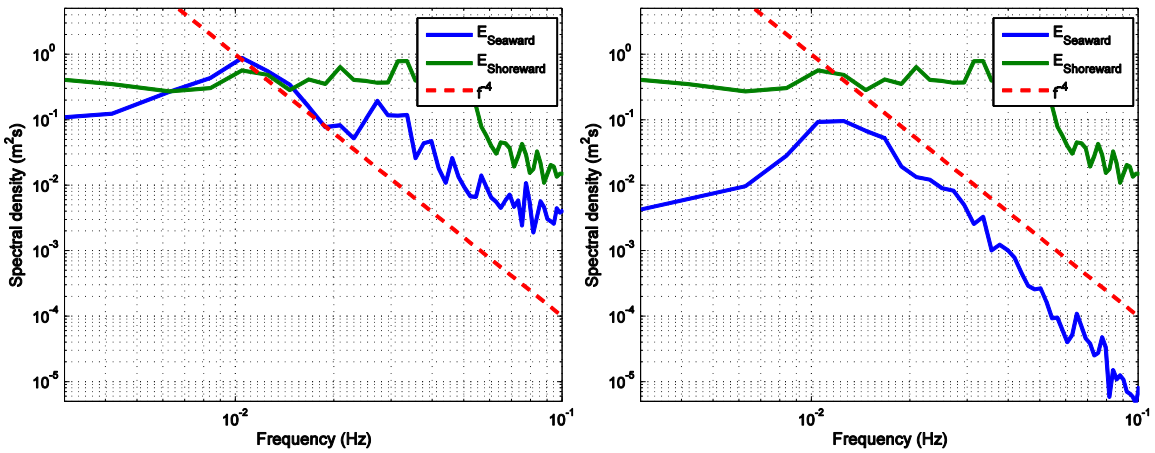

Figure 3.9 Average spectra for shoreward (green lines) and seaward (blue lines) IG waves within the surf zone (left figures). Right figures compares shoreward spectra in the surf zone to seaward spectra outside the surf zone (blue lines). Upper figures are for 4% slopes and bottom figures for 2% slopes. Red dashed lines show the f^{-4} variations. All cases were forced with a 4m, 12.5 s JONSWAP sea with a spread of 10.

In the surf zone the incoming spectra (consisting mostly of forced waves) tend to be broader and 'flatter' than the outgoing spectra. The outgoing spectra seem to be narrower with a bell shape both in the surf zone and outside. This bell shape, is typical of IG field observations (cf chapters 4 and 5).

For higher frequencies, the outgoing spectra seem to be modulated by an f^{-4} law both in the surf zone and outside. This seems to indicate that the shape of the outgoing free IG spectra is governed by the shoreline reflection coefficients (equations (2.16) and (2.19)). We can therefore make a link between this outgoing IG frequency distribution and both the incoming (mostly bound IG) frequency distribution and the bed slope via the normalized bed slope. The $D^{-1/2}$ asymptotic de-shoaling law still holds. The changes in the shape of the spectra between the surf zone and outside can be attributed to the k/c_g relation which is frequency dependent.

The f^{-4} dependence is similar to what is observed in wave runup spectra (Ruggiero et al., 2004; Senechal et al., 2011). We shall also see in the next chapter that this f^{-4} dependence can be seen in some IG observations, though it is often masked by a flatter background IG distribution.

3.3.5 Effect of bottom slope

Keeping other factors constant, the effect of a small variation in bottom slope (from 2% and 4%) on the outgoing IG spectra is small as shown on Figure 3.9. However increasing the slope to 10% has more noticeable effects on both the incoming and outgoing IG spectra is shown in Figure 3.10.

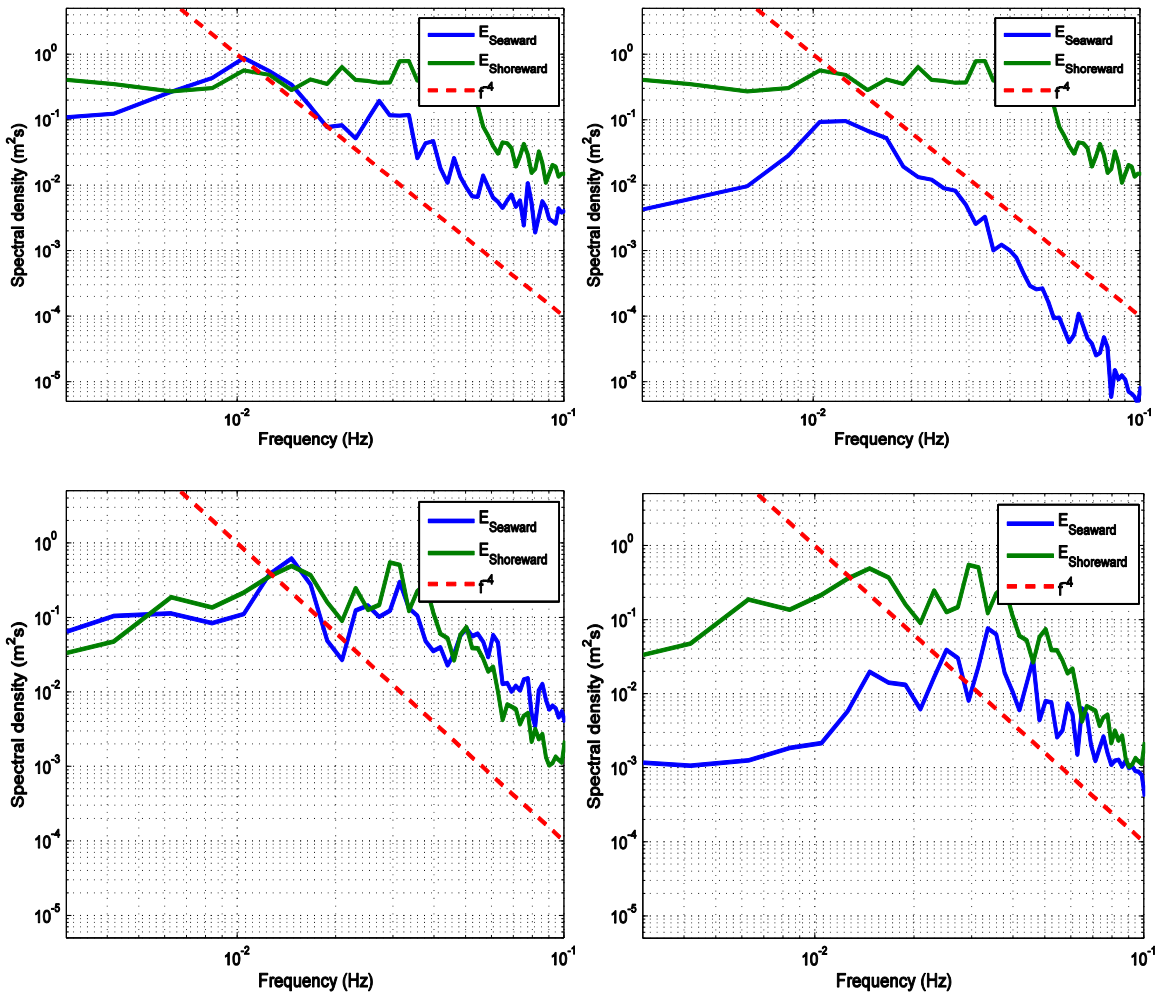

Figure 3.10 Average spectra for shoreward (green lines) and seaward (blue lines) IG waves within the surf zone (left figures)and outside the surf zone (right figures). Upper figures are for 2% slopes and bottom figures for 10% slopes. Red dashed lines show the f^{-4} variations. Both cases were forced with a 4m, 12.5 s JONSWAP sea with a spread of 10

Varying the slope not only affects the outgoing far-field IG levels, but also the incoming IG spectra within the surf-zone. For a 10% slope, the incoming IG spectrum is more 'bell shaped'. The spectral peak(s) also seem to have shifted to higher frequencies. Also, within the surf zone, the incoming and outgoing spectra are very similar.

This could be the effect of a different bound IG growth or it could be that the IG energy comes from a different mechanism, such as breakpoint generation mechanism.

The effect of the higher slope on the outgoing far-field IG levels is also very noticeable. The spectral peak(s) seem to have shifted to higher frequencies. The f^{-4} variations are still present but are less pronounced and have also shifted towards higher frequencies. Also both the spectrum of the outgoing far-field IG and the incoming IG spectrum within the surf-zone seem to become similar for higher frequencies.

3.4 Variability of free IG level

Using the same logic as Ardhuin et al. (2014), we postulate an empirical relationship for the IG wave height HIG radiated from the shoreline as

$$H_{IG} \approx \alpha_1 H_s T_{m0,-2}^2 \sqrt{\frac{g}{D}} \tag{3.9}$$

where H_s is the significant wave height of wind seas and swells, Tm0,-2 is the mean period given by the -2 and 0 moments of the surface elevation spectrum, g is the apparent acceleration of gravity, D is the local mean water depth, and α1 is a dimensional constant. The choice of wave period $T_{m0,-2}$ is relatively arbitrary. Basically, it is less noisy than the usual peak period, and gives more importance to the low frequency part of the spectrum than other mean periods defined from the -1 or +1 moments. The important aspect of this model is the empirical source of IG free waves, which was inferred from coastal measurements in Hawaii, North Carolina and France. In our XBeach runs using a JONSWAP short wave spectrum, Tm0,-2 has been replaced by the T_p parameter of the spectra.

Under most circumstances, the variation of Hig in terms of of $H_s T_{m0,-2}^2 \sqrt{\frac{g}{D}}$ seems to be linear. Varying most parameters does not seem to affect the value of α_1 except for the directional spread of the incoming spectra. We are hence going to investigate mostly the effects of directional spread and also of the shelf width on the outgoing IG levels.

3.4.1 Effect of directional spread

In this section we are going to investigate the effect of varying the angular spread of the incoming short waves spectrum on the offshore free IG level. We use XBeach with a 2D coastal configuration: a square domain with a constant slope of 10% and a 10m grid. Other aspects are kept constant. An incoming 4m, 12.5s JONSWAP spectrum with a principal direction of 10° (260° from the north) normal to the shore was imposed, with the angular spread varying from 5 to 200. The directional spreading coefficient is given in terms of the cosine law, $\cos^n$. Higher values indicate lower directional spread.

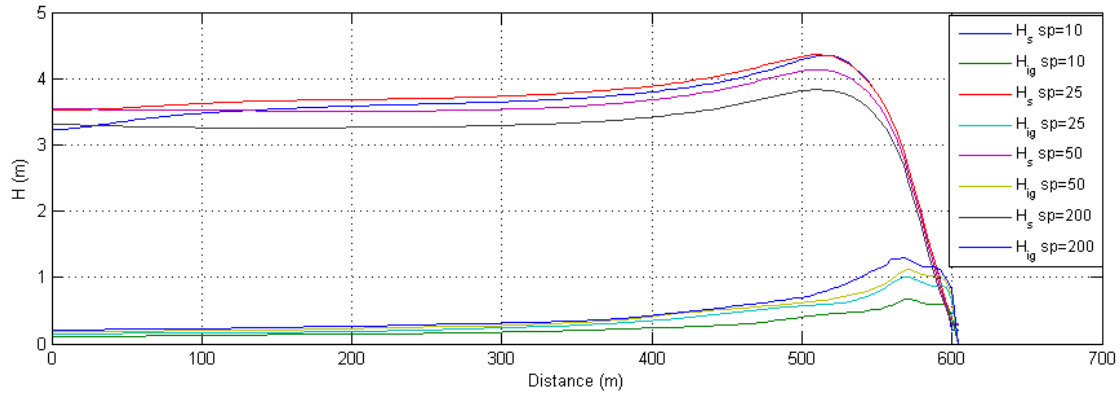

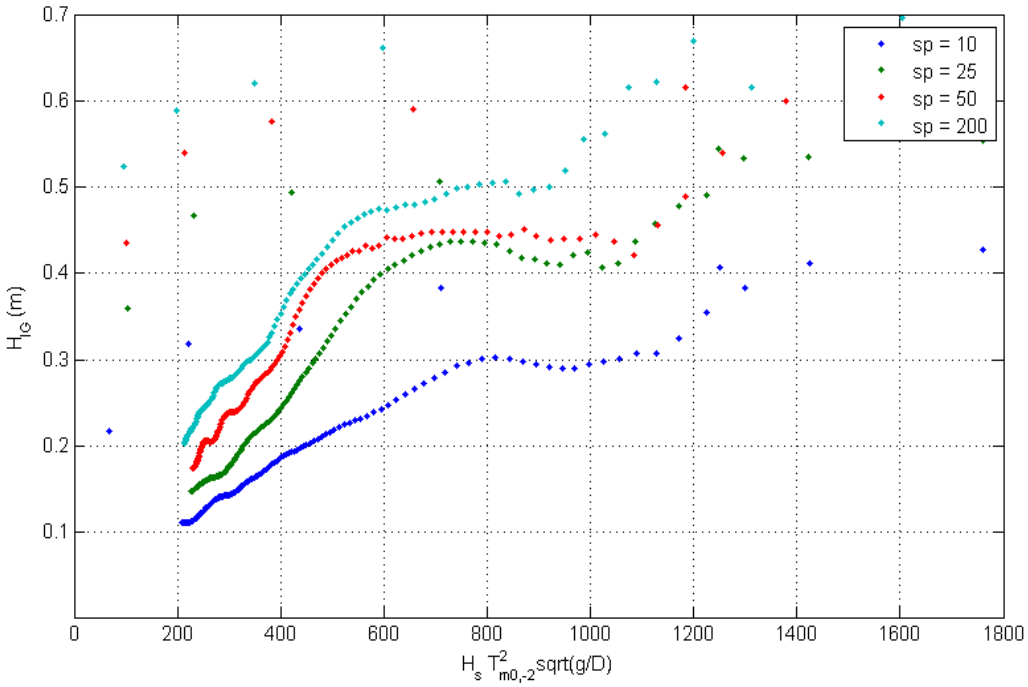

Figure 3.11: Results for incident 4m JONSWAP spectrum with varying angular spreads for (top) IG levels and (bottom) the variation of outgoing Hig in terms of $H_s T_{m0,-2}^2 \sqrt{\frac{g}{D}}$ (α is the gradient).

The values of alpha obtained are summarized in Table 3.1 below.

Slope	Hmo	Dir	Angular Spread	Tp	Alpha
10.0%	4m	260	200	12.5	0.00088
10.0%	4m	260	100	12.5	0.00083
10.0%	4m	260	50	12.5	0.00077
10.0%	4m	260	25	12.5	0.00067
10.0%	4m	260	17	12.5	0.00058
10.0%	4m	260	10	12.5	0.00043
10.0%	4m	260	5	12.5	0.00035

Table 3.1Summary of XBeach runs for different values of angular spread.

As expected, the angular spread coefficient, *sp* of the incoming short waves field, has a large influence on the outgoing long wave height. This seems to be quite logical given the sensitivity of the 2nd order coupling coefficient with respect to the angular difference between interacting primary waves. We shall try to integrate this parameter appropriately in the empirical model (Ardhuin et al., 2014) for Hig.

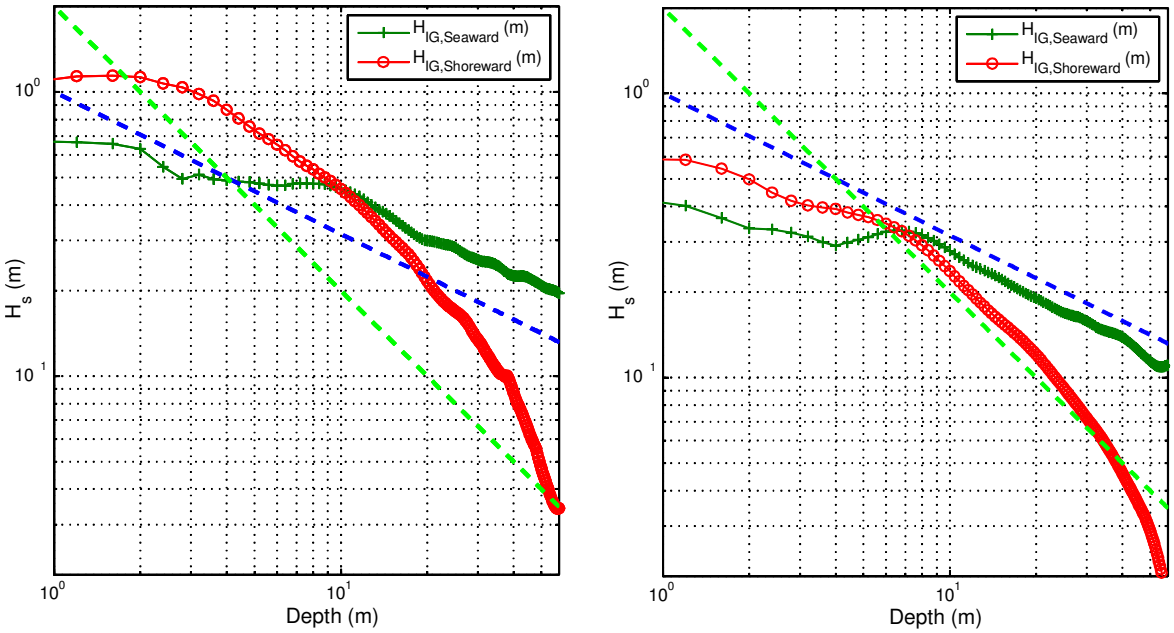

Figure 3.12: Evolution of seaward (green) and shoreward (red) IG wave heights for model runs with a spread of 200 (left) and 10 (right). Blue and green dashed lines represent $D^{-1/2}$ and D^{-1} asymptotes respectively.

As can be seen in Figure 3.12, changing the spread not only changes the outging IG levels but also the point at which the liberation seem to occur. Liberation tends to occur in deeper waters when the incoming spectrum is directionally narrow. As noted previously, past the turning point, the level of free IG is consistent with a $D^{1/2}$ variation in accordance with (Herbers 1995).

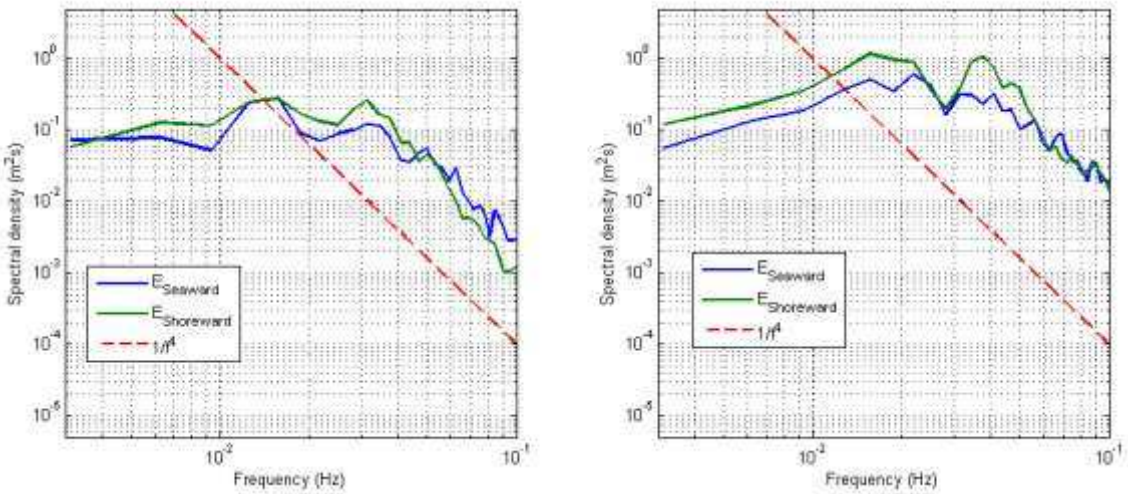

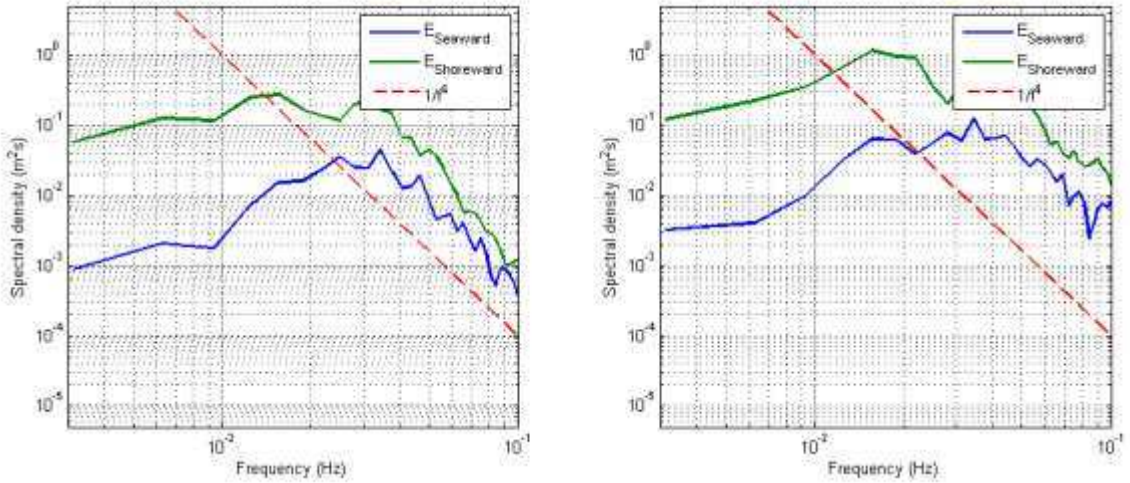

Figure 3.13: Average spectra for shoreward (green lines) and seaward (blue lines) IG waves within the surf zone (top figures) and between surf zone and outside the surf zone (bottom figures) for a spread of 10 (left) and 200 (right) on a 10% slope. Red dashed lines show the f^{-4} variations.

The angular spread also seems to influence on the shape of both the incoming and outgoing IG spectra in the surf zone. The IG peak appears to occur at a higher frequency when the directional spread is narrow. Also both incoming and outgoing IG spectra are flatter when the incoming short waves spectra have more spread. Since both the incoming and outgoing IG spectra are influenced in the same manner, this should facilitate the estimation of outgoing free IG from incoming bound IG.

3.4.2 Effect of shelf width

In this section we are going to test the hypothesis of whether the width of the shelf plays an important role in the free IG level offshore. To investigate this aspect, the XBeach model will be used using 2 coastal configurations in 2D, so as to fully capture refractive and trapping effects. In this experiment, we have tried to keep all aspects constant and try to vary only the width of the shell.

As can be seen on Figure 3.14, the general shapes of the profiles are kept constant, with piecewise similar slopes. Only the width of the shelf has been roughly doubled. The profiles are similar in shape to those found at Duck, except that they have been smoothed, the depth at the incoming boundary are limited to 250m and the general width of the shelves are much lower. The aim was to reproduce a typical continental shelf but at a smaller scale. The domain was roughly square in shape so as to capture refractive and trapping effects, and has a grid resolution of 10m. The forcing was applied at an angle of 10° from the perpendicular.

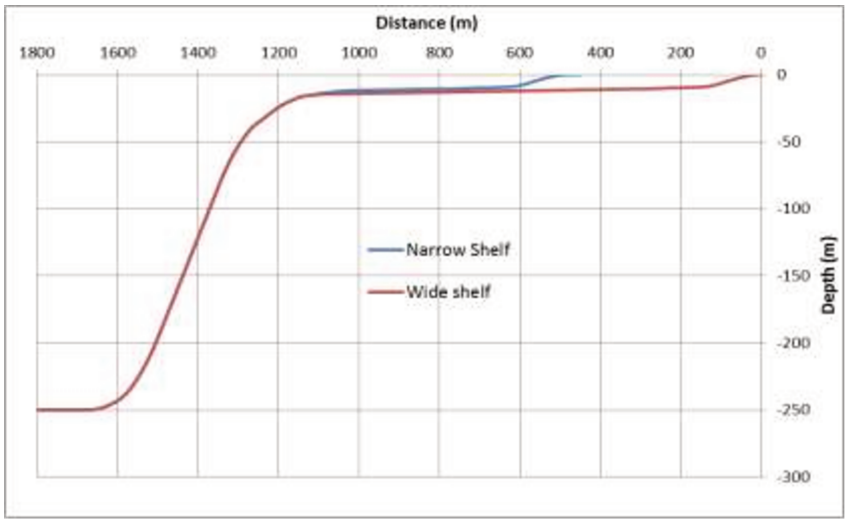

Figure 3.14: Different Profiles used

The 'deep sea' here is limited to 250m so as to have fairly measureable IG levels at the boundary. Too much de-shoaling will give IG levels that are too low. Although we have tried to keep all aspects constant and try to vary only the width of the shell, the overall average slope does inevitably vary.

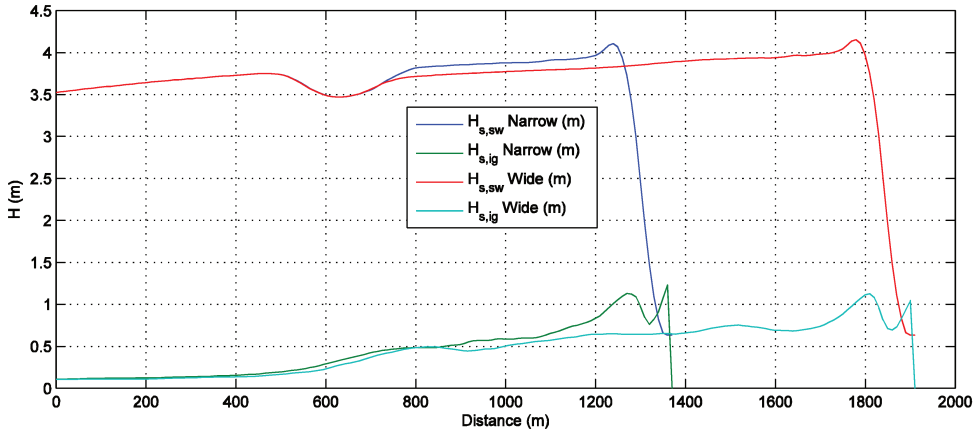

Figure 3.15: Results for incident 4m JONSWAP spectrum on a narrow and a wide shelf

The far-field IG level seems to be not much affected by the width of the shelf contrary to what was suggested by Herbers et al. (1995). However in our case, bottom friction was low. It is however expected that for higher friction coefficients, the outgoing IG should decrease in the case of a wider shelf. There might also be an issue with deeper waters as the conditions might not still be considered shallow water for the IG waves, for example in the case of 30 seconds waves. That means XBeach is not representing the motions properly.

3.5 Modelling of IG waves around Bannec Island

Having conducted a few experiments and stuied different aspects of IG waves, we now seek to test the modeling of IG waves using XBeach in a regional context for which there exists some ground-truthing. It will also be interesting to test a case which has been previously studied, and which shows some interesting aspects such as extreme sea conditions and complex topographies.

We have thus chosen to study the IG wave field in the Iroise Sea off the coast of Brittany with a focus on Bannec. Bannec is a small island about 1 km long and 200 m across, and is the only island in the Molène archipelago to be directly exposed to ocean swells, due to the presence of a steep cliff on its western side. It is otherwise partly protected from north-west waves by the bigger island of Ouessant. The lowest points along the cliff crest are 5 meters above the highest astronomical tide, which is 10 m above mean sea level. At the top of these slopes, the bedrock is fractured. Cyclopean blocks are found to be displaced every few years during severe storms that occur with spring tides (Fichaut and Suanez, 2011), and sometimes even transported across the whole island, over distances of up to 200 m.

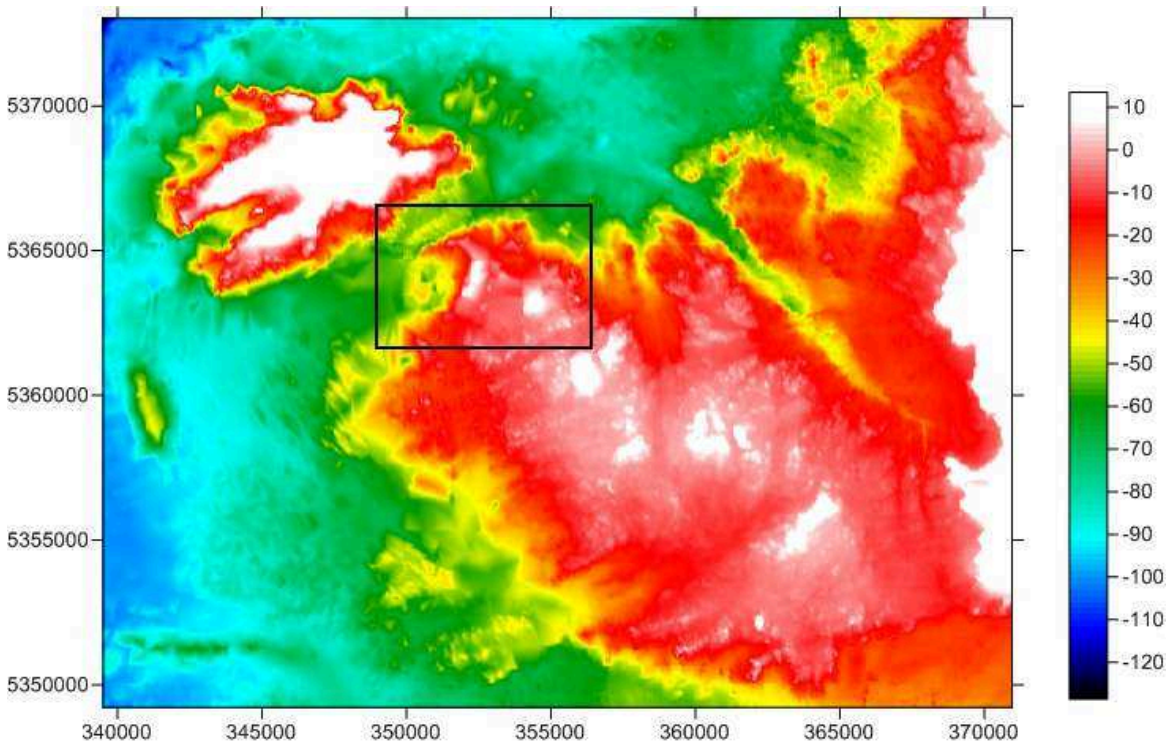

Figure 3.16: Bathymetry around Molène archipelago off the coast of Brittany, France. Coordinates are in UTM.

This particular case of "cliff top storm deposits" (CTSDs) has motivated an investigation of extreme water levels on the cliff as part of the ANR-funded "HEXECO" program. Sheremet et al. (2014) established that the very high water level reached on the cliff face were largely due to some of the highest ever measured infragravity waves with heights reaching 3 meters. These conclusions may be relevant to other cases of CTSDs

documented by Hall et al. (2008) in Shetland, or not, depending on how specific the IG wave response is to the shoreline geometry.

Measurements of water levels on the exposed cliff of the island were performed in the winter of 2008-2009 to investigate the relation between storms and extreme water levels that lead to the quarrying of blocks from the top of the cliff and their deposition across the island. The most extreme event was recorded in February 2009. The records were also used in Ardhuin et al. (2011a).

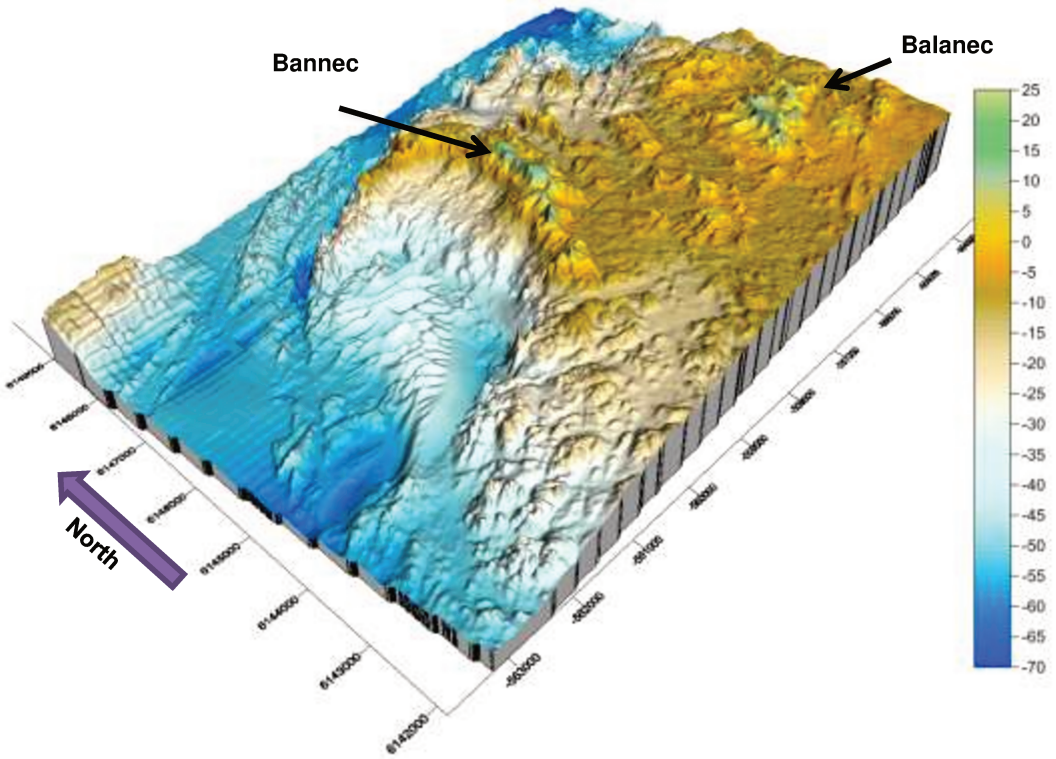

Figure 3.17: Topography of Bannec and Balanec Islands showing the steep cliff on the western coast of Bannec, and the shallow bathymetry between Bannec and Balanec. Coordinates are in UTM (meters).

During storms, the Island of Ouessant is fully exposed to North Atlantic waves, with significant wave heights (Hs) of the order of 12 m, but it also partially shelters Bannec. Even then, the recorded levels of IG waves at these locations, particularly in the 300s band, were particularly high during the February 10, 2009 storm.

It should be noted that for the case of a complex topography such as Bannec, a high IG variability is expected and even then, the empirical formulation of Ardhuin et al. 2014 seems to be working very well.

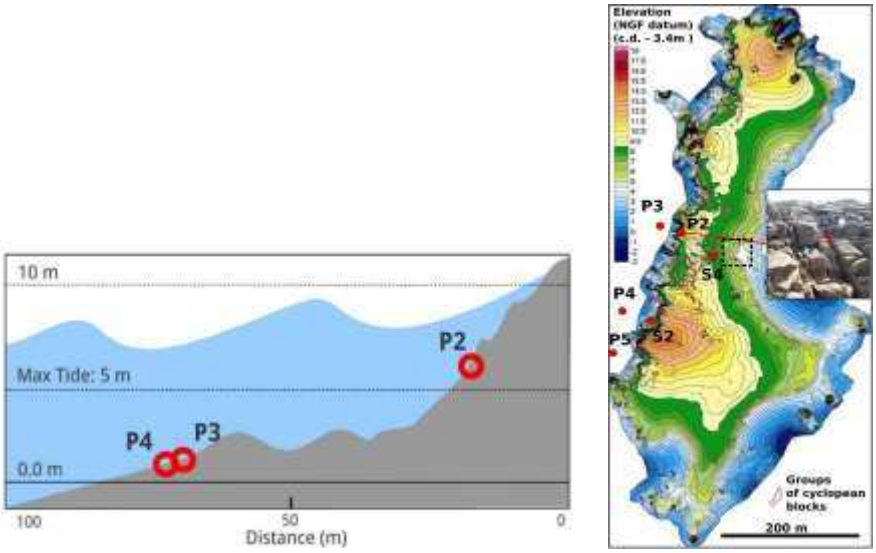

Figure 3.18: Bathymetry and position of sensors for the experiment

Several pressure gauges (P2 to P5: Ocean Sensor System model OSSI-010-003C) were mounted on stainless steel plates bolted into the rock. The results used here comes mainly from two sensors, P3 and P2, which were installed along a cross-shore transect, at elevations of 1.30 and 7.52 m above chart datum as shown on Figure 3.18(a). P2 is directly on the cliff and P3 is about 40 meters offshore.

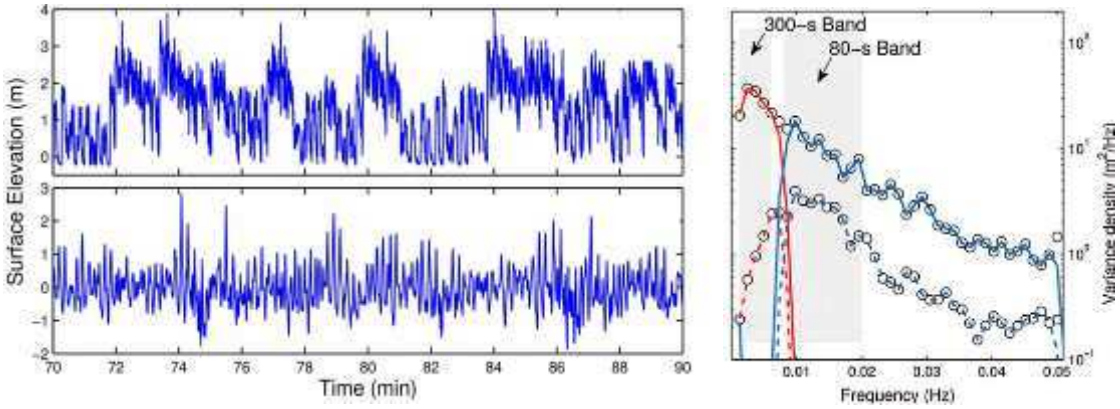

Figure 3.19 Recorded water level observations at P2 (top left) and P3 (bottom left) around 04h00 on February 10th 2009. The right figure shows the spectral level at P2 (continuous line) and P3(dashed line) with red and blue lines representing the 300-s and 80-s IG band respectively (adapted from Sheremet et al., 2014)

The observations at these two points are of interest because of the unusual difference in IG levels between them, despite them not being very far apart (Figure 3.19). The difference was noted for both for spectral shapes and the amplitude. In the 300s band (0.001Hz to 0.005Hz) the spectral energy ratio was approximately 36 which corresponds to a six-fold increase in amplitude (Sheremet et al., 2014). This difference in observed IG levels was investigated by Sheremet et al. (2014) and modelled using a non-linear shoaling model but on a local scale. However they did not succeed in reproducing the spectral difference in observed IG levels, concluding that shoaling was

probably not the main explanation.

Our main challenge is to reproduce these observations both qualitatively and quantitatively, which is the aim of this section. In order to achieve this, we shall use XBeach on local and regional 2D configurations with different forcing.

3.5.1 Modelling on a local scale

We start with a regular configuration with uniform15m resolution run on high tide conditions around Bannec as shown in Figure 3.20.

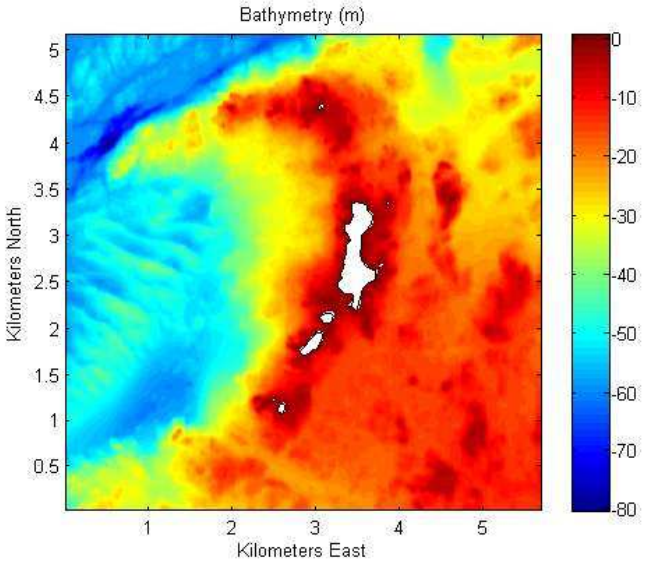

Figure 3.20 Water depth with high tide conditions as used in model setup.

The model is forced with a 5m, 12s peak period and 250° angled JONSWAP spectrum with a ($\cos^n$) spread of 10. This domain size and forcing is similar to the modelling of Sheremet et al. (2014). Results are shown in Figure 3.21.

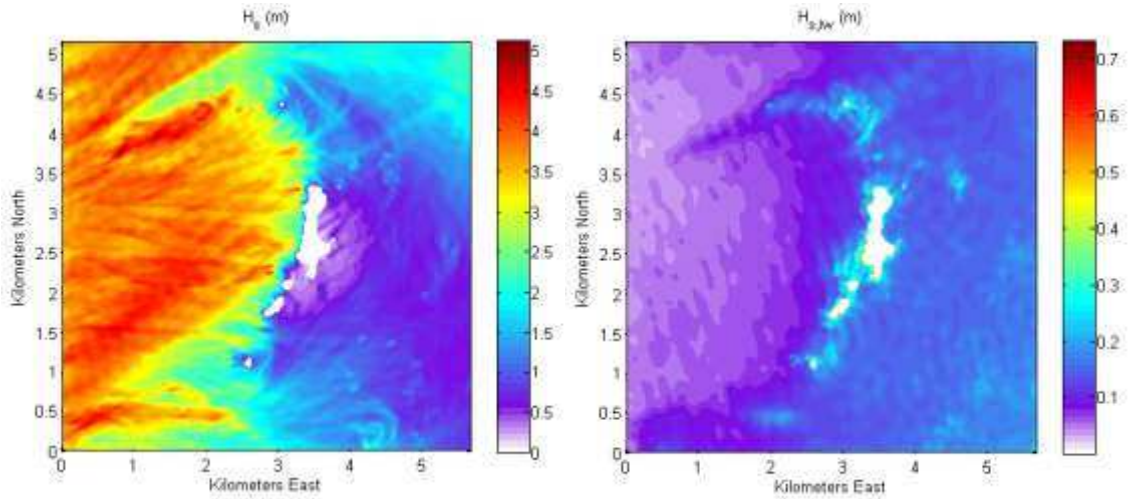

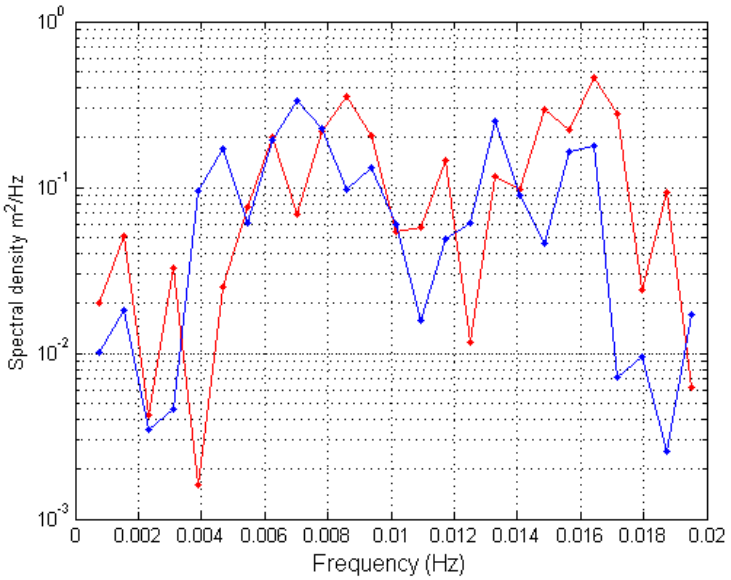

Figure 3.21 XBeach results showing the average short wave field (top left) and the average IG wave field (top right) for a 4m, 12s peak period and 250° angled JONSWAP forcing. The bottom figure shows the spectral results at points P2 (red) and P3 (blue).

It can be seen that although the short waves are directly reaching the Bannec coast with Hs over 3 meters, the IG levels are quite low. Also the IG levels observed at points P2 and P3 seem to be quite similar, and flat. Spectral energy levels below 0.005Hz (300s band) is even lower than the rest of the spectra. This does not corroborate well with the field observations. However it can be observed that IG levels on the east of the island are higher than on the west coast.

3.5.2 Modelling on a regional scale

As we were not able to match the observed spectra at this scale, we chose to carry on with a larger regional domain so as to capture other processes which might influence the IG levels around Bannec.

We setup a non-uniform rectilinear grid on a regional scale with the complete group of Islands and part of the continental coastline and run on high tide conditions. The resolution was about 10m around Bannec and 50m near the boundaries, totalling about 400,000 nodes.

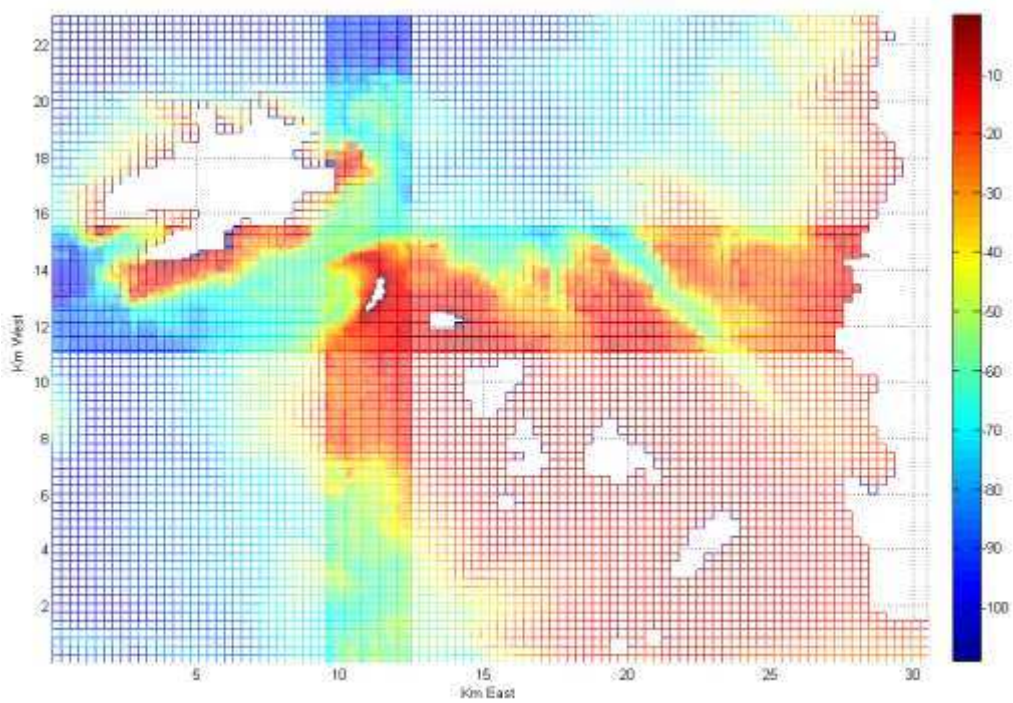

Figure 3.22 Rectilinear grid used in model setup. The grid resolution has been exaggerated fivefold for clarity.

Sheremet et al. (2014) forced their model with a 5m, 13s peak period and 250° angled JONSWAP spectrum. The Island of Ouessant was however fully exposed to North Atlantic waves, with maximum significant wave heights (Hs) of the order of 12m coming probably from the north-west direction.

3.5.3 Case 1: 5m, 13s, 250° continuous JONSWAP

In line with Sheremet et al. (2014), the model is forced with a 5m, 13s peak period and 250° angled JONSWAP spectrum with a ($\cos^n$) spread of 20. This configuration ensures that maximum wave energy reaches the coastline of Bannec, without much shielding from Ouessant. Results are shown in Figure 3.23 below.

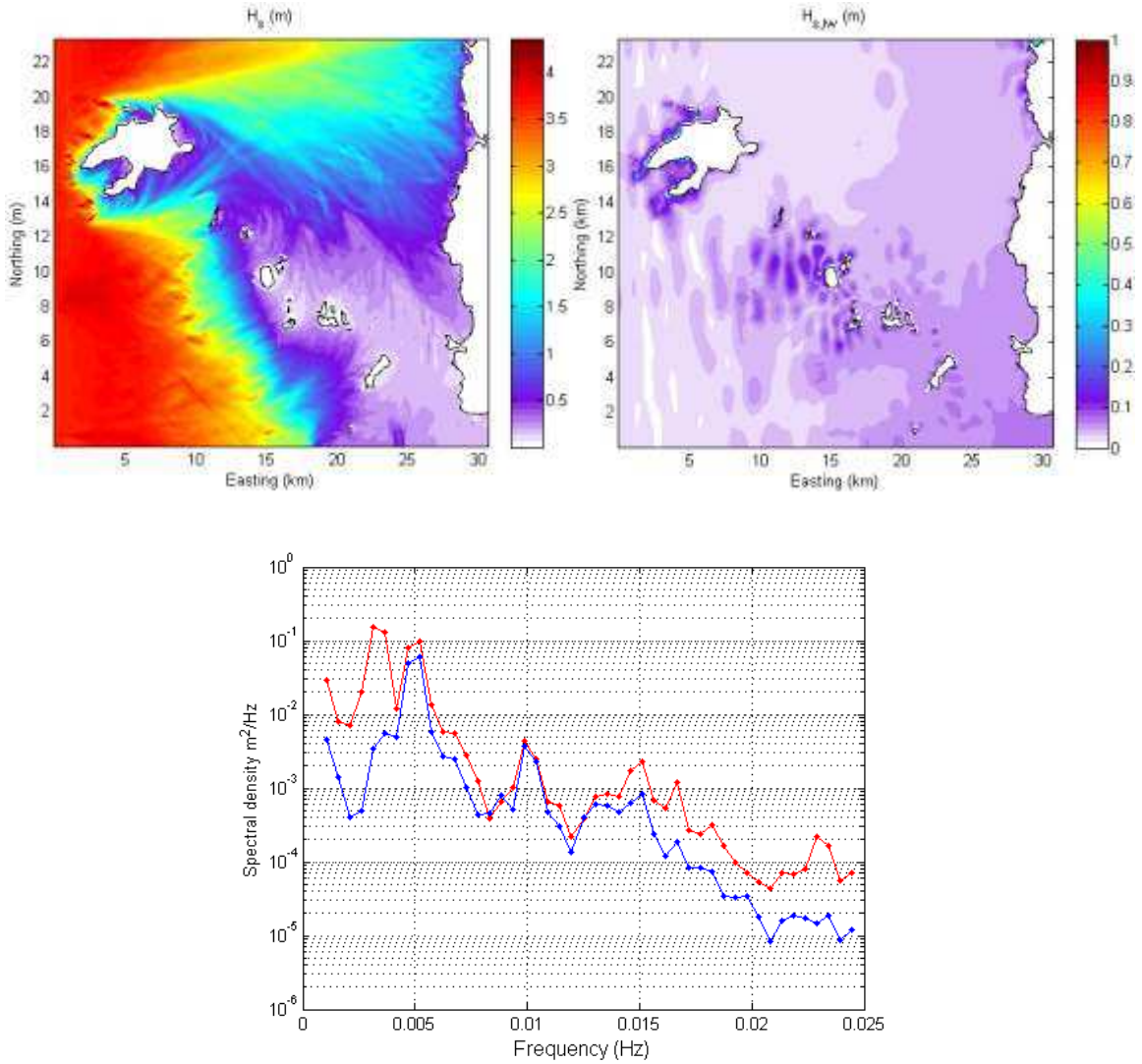

Figure 3.23 XBeach results showing the average short wave field (top left) and the average IG wave field (top right) for a 4m, 12s peak period and 250° angled JONSWAP forcing. The bottom figure shows the spectral results at points P2 (red) and P3 (blue).

Here also, although the short waves directly reach the Bannec coast with Hs reaching 3 meters, the IG levels are less than 1 m. More importantly, the IG levels observed at points P2 and P3 seem to be quite similar, with differences seen mostly below 0.004Hz. Qualitatively the spectral difference does not relate to what was recorded by the field measurements. This configuration also does not seem to capture the processes that resulted in the recorded observations.

3.5.4 Case 2: 10m, 13s, 300° JONSWAP

In order to understand the possible causes of these extremely high levels of IG waves on the coastline of Bannec Island, we now proceed with an offshore forcing corresponding to the presumed sea state off Ouessant: a JONSWAP spectrum of 10m Hs, 13s peak period and 300° direction with moderate spread ($\cos^n$ with n=20). Results are shown in Figure 3.24 below.

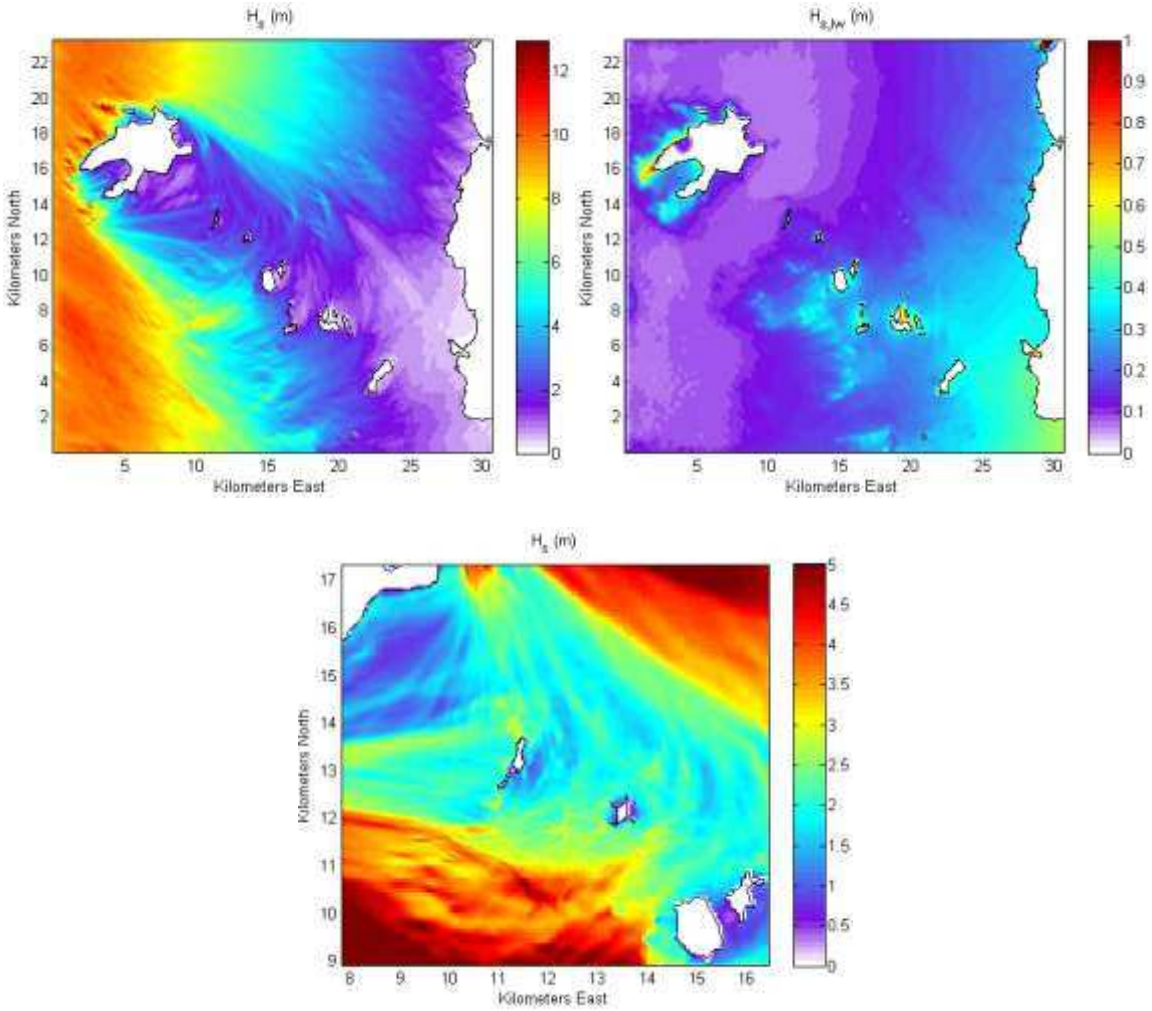

Figure 3.24 Average short wave field (top left) and the average IG wave field (top right) for a 10m Hs, 13s peak period and 300° angled JONSWAP forcing. The bottom figure is zoom over Bannec and Balanec for the average short wave field.

In this case, although the Hs off the Island of Ouessant are around 10m, those reaching Bannec are less than 3.5 meters. The waves reach Bannec, Balanec and Molène indirectly and from multiple directions, mostly from the north and south. The forcing around Bannec is thus quite different from the previous case, and the IG response is expected to be different as well.

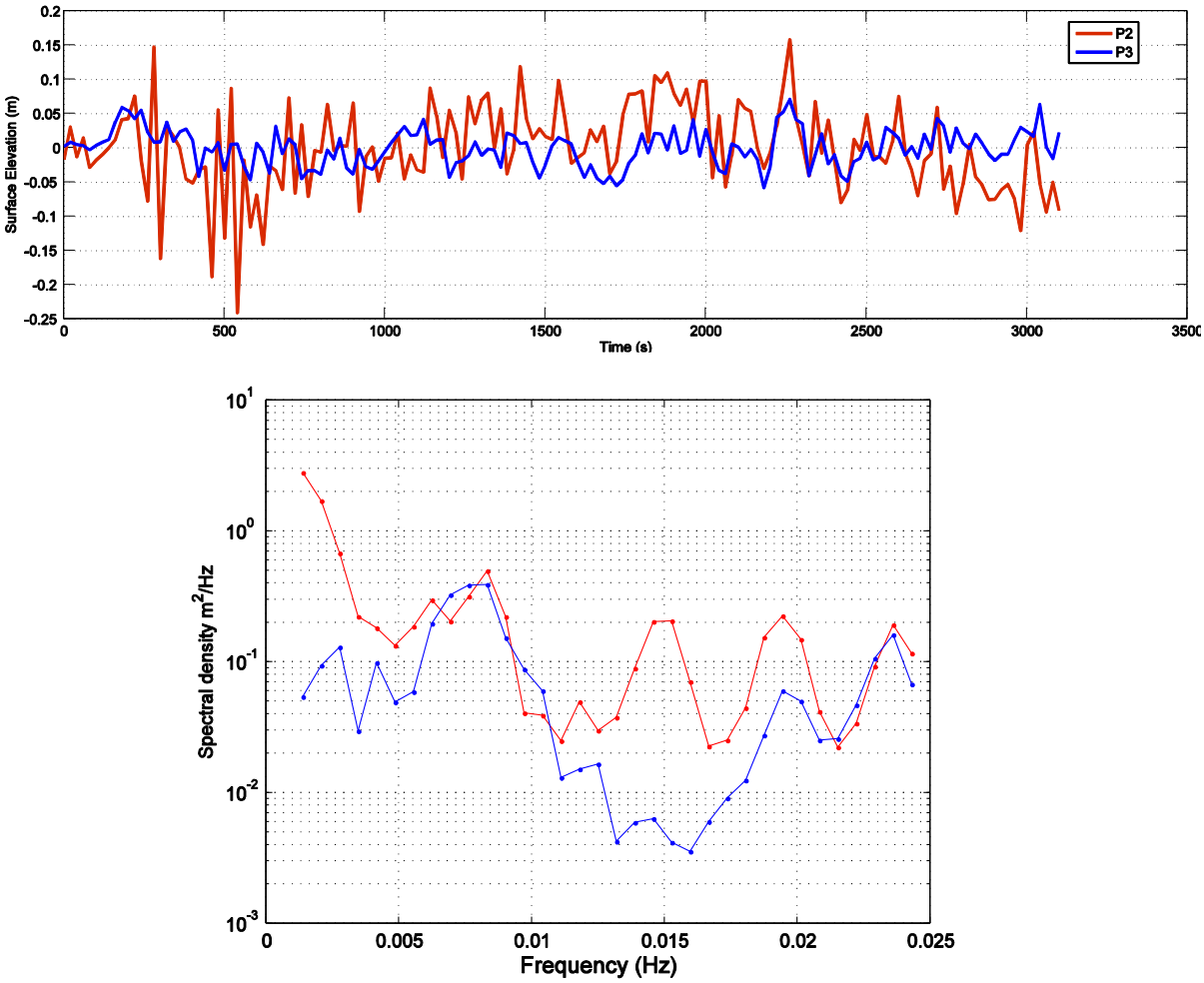

Figure 3.25 Time series of surface elevations (top) and spectral levels (bottom) at points P2 (red) and P3 (blue).

Qualitatively, this time the spectral IG distribution seems to be in line with the observations. Quantitatively though, both are a bit lower (Figure 3.25) than the observations. This could be because the 50 m resolution is cutting off some of the wave group forcing at the boundary. But the difference in IG levels below 0.005Hz (300s band) between P2 and P3 is consistent with what was observed and described in Sheremet et al. (2014).

3.5.5 Discussion

Spectral analysis of the computed surface elevation from the previous simulation over the whole domain reveals a standing oscillation of the whole archipelagic system including part of the continental coastline. This is similar to the analysis of (Munger and Cheung, 2008) in the context of tsunami excitation over the Hawaiian archipelagic system.

An analysis of the average IG wave field integrated in the frequency band of 1mHz to 5mHz (300s band) is shown in Figure 3.26.

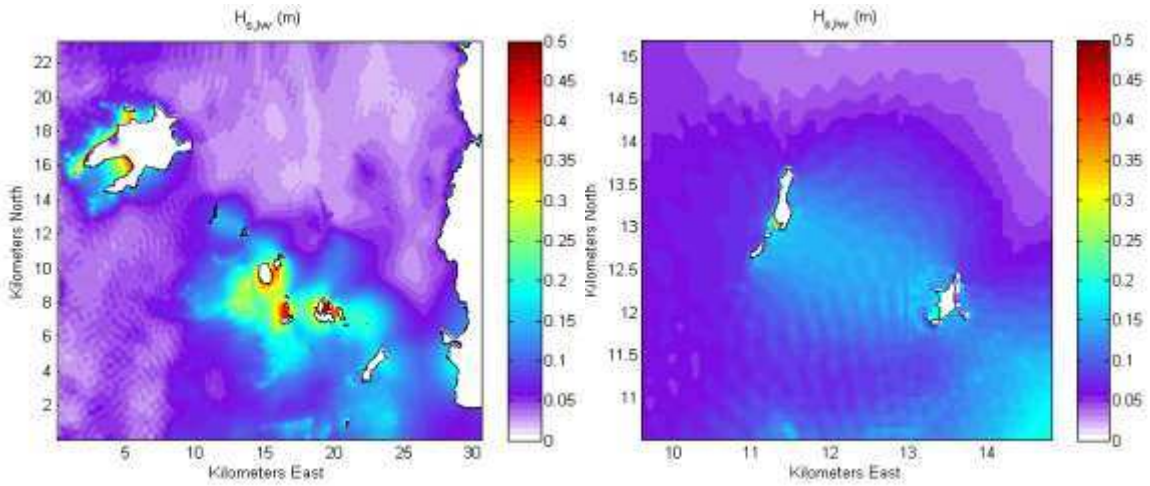

Figure 3.26 Average IG wave field (in meters) integrated in the frequency band of 1mHz to 5mHz (300s band) over the whole archipelago (left) and a zoom over Bannec and Balanec (right). Notice the abrupt decrease in IG levels off the west of Bannec and the absence of a standing wave between Bannec and Ouessant.

There seem to be a standing wave corresponding to the 300s band, as suggested by Sheremet et al. (2014), but rather between the islands of Bannec and Balanec. This oscillation mode is probably excited by long and short waves going around Ouessant and later focusing on this region. Bannec and Balanec act as nodes with an antinode between them. The shallow bathymetry in this area allows for more non-linear interactions to occur, such as more bound IG generation and non-linear shoaling, which could explain the high excitation.

Low energy level in this area between Ouessant and Bannec, indicate that the standing wave is absent there. This explains the lower levels observed at sensors offshore west of Bannec. The standing IG wave in this mode seems to travel by refraction as an edge wave around Bannec from the east to the west side around the southern part and possibly also around the north. It is quite possible that the wave even completely submerges the middle narrow part of the island at times. Field measurements between the islands of Bannec and Balanec during winter storms could help confirm this standing wave.

Edge waves are known to decrease exponentially from the shoreline and together with the abrupt de-shoaling helps explain the high IG levels observed at P2 and not at P3. The other peak of 80s which was singled out by Sheremet et al. (2014), doesn't seem to be present in this configuration though peaks at 0.008Hz and 0.015Hz are present.

To further substantiate these results however, and match the observed results quantitatively, it would be interesting to build another configuration with a rotated grid in the direction on the incoming waves. This grid would have allowed more focus on the region of interest. Also a higher sea state of 12m Hs and 13s period from 300° would have been more realistic.

3.6 Natural oscillation modes and Decay of IG energy

One of the questions asked is about the time decay of IG levels in a complex coastal region when excited by incoming waves. Incoming long waves and also probably bound IG from short waves can excite coastal modes and resonate, and this would 'keep' the energy near the coast before being more gradually leaked or dissipated. Lippmann et al., (1999) estimated the half-life decay timescale to be of the order of 10–30 edge wave periods.

In order to study the decay of IG energy and the natural oscillation modes the previous configuration was run with a Heaviside type excitation, where a forcing is applied until steady conditions are reached and then switched off. The on-going oscillations are then studied (Figure 3.27)

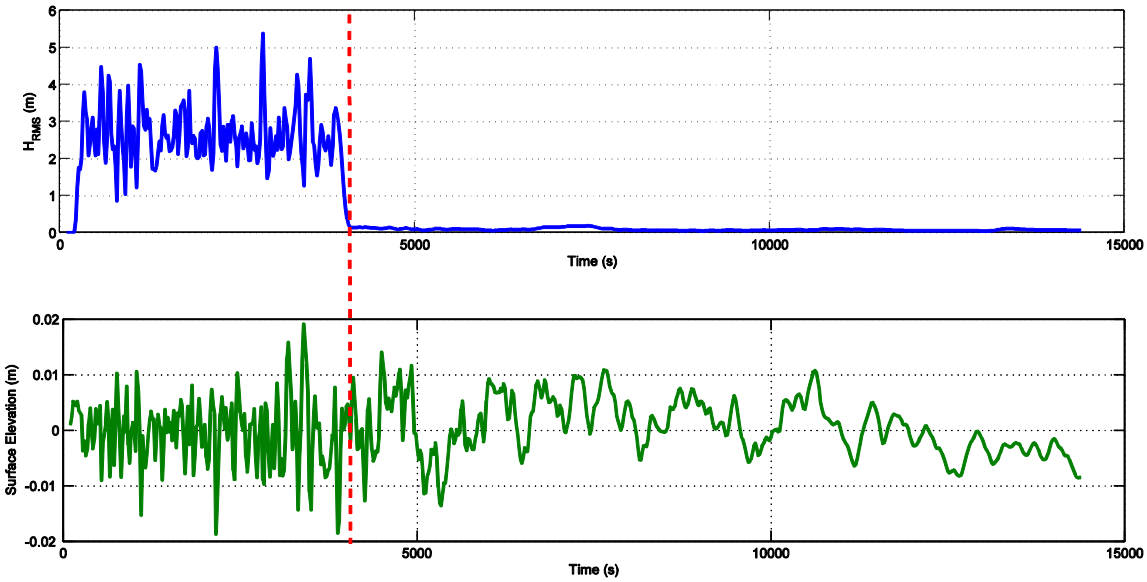

Figure 3.27 Time-series of the rms wave height (top) and the surface elevation at a point near the forcing (western) boundary of the domain. The dashed red line represents the instant where the forcing was stopped.

An interesting observation is that low frequency oscillations can last for quite a long time (hours) after the excitation has been shut down. However this seems to concern mostly very low-frequency motions, (around 1000s) which tend to coincide with the lowest natural modes of the coastline system. In case of resonant interaction with the incoming short waves excitation, this effect could be further amplified. What is being observed at the boundary when the excitation is turned off is the escaping IG energy. Figure 3.28 shows the spectra extracted at a few points of interest

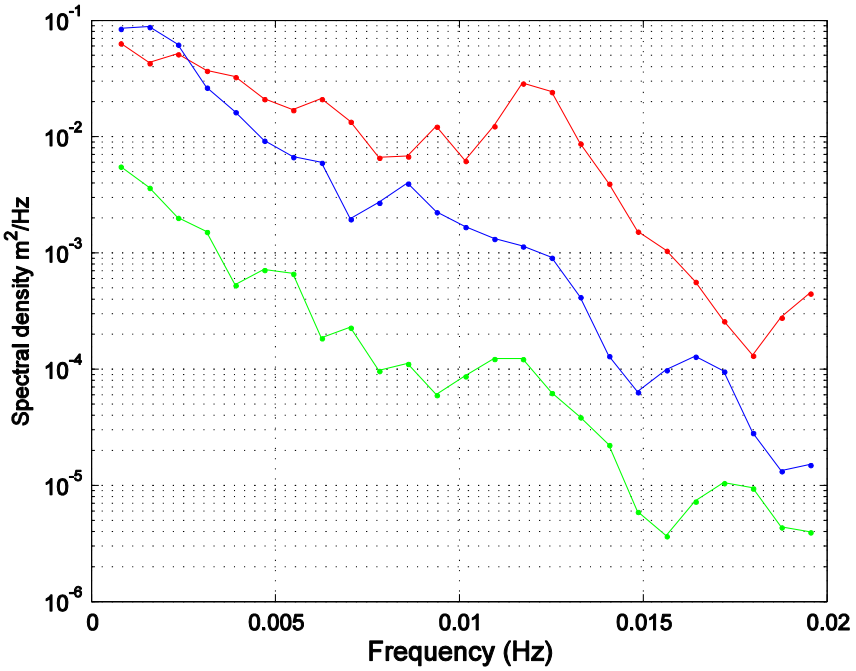

Figure 3.28 Spectral results at points P2 (red), PBB which is a point midway between Bannec and Balanec islands (blue) and P-Boundary (green) which is a point near the forcing (western) boundary of the domain.

We notice here a spectral peak around 0.0125Hz at P2. From the free oscillations of the water surface, we can also obtain the natural oscillation modes of the system. Figure 3.29 shows an example of the 320s and 80s modes.

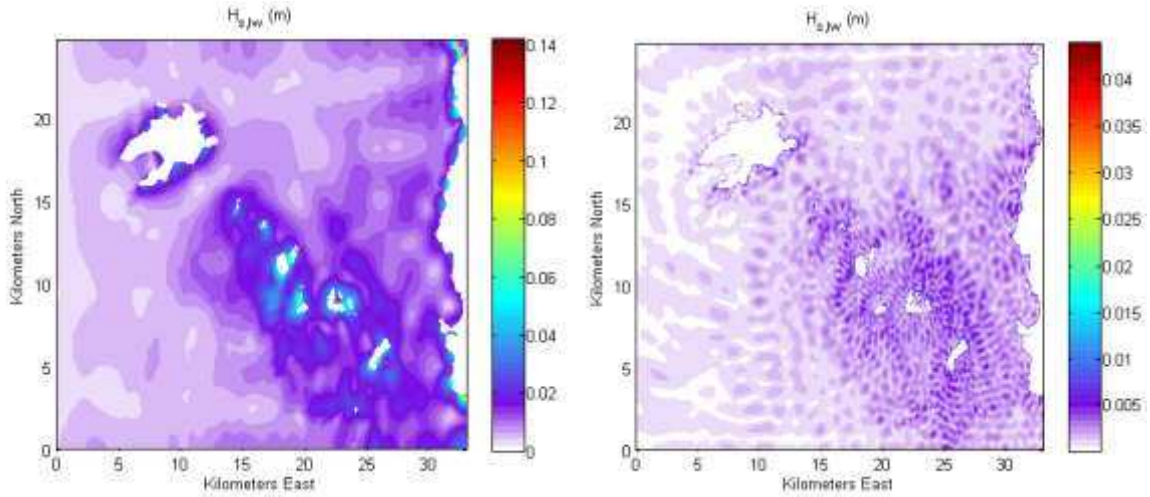

Figure 3.29 Natural oscillation modes in the Iroise Sea. On the left is the 320s mode and on the right the 80s mode.

Although the motions with highest energies are lower in frequency than our classical IG band, (300s) they might still impact on the general IG level going out of the system. This would be through subsequent transfer of energy into higher frequencies due to non-linearities, topographic scattering and the non-stationarity of the resulting motions.

3.7 Conclusion

Phase-resolving methods appear to successfully describe the processes concerning IGW formation, transformation and propagation. SWASH is able to capture the right IG processes without much parametrization especially on 1D scale, but investigation on 2D scales could not be properly carried out due to parasitic back reflection of IG waves at the incoming boundary.

XBeach provides a complementary modelling approach with good results and lower computational costs arising mainly from the non-necessity to completely resolve the water surface with grid resolutions in the order of short waves . XBeach proved to be especially suitable for a long wave studies. This allowed us to use XBeach for the investigation of factors influencing the offshore free IG levels and the verification of the IG parameterisation proposed by Ardhuin et al. (2014).

The role of the reflection coefficient, governed by the normalised bed slope, was highlighted for the offshore IG levels with the liberation mechanism. This will be useful for the parametrizations of the free IG spectra in the upcoming chapters. The role of this reflection coefficient seems to be less important for higher bed slopes, probably due to the breakpoint mechanism.

XBeach also allowed the modelling of regional domain sizes such as the Iroise Sea with the Molène archipelago, where we have found a plausible explanation for the presence of high level 300s band IG waves around the cliff of Bannec Island during extreme storms. We also studied the possible IG accumulation and decay in such complex coastal configurations, which might impact modelling on a global scale with grid sizes in the order of the shelf width.

However even the surf-beat modelling approach would prove to be too expensive for modelling IG waves on a global scale. Thus the next objective would be to implement a spectral approach which should be usable on a global scale, as will be investigated in the next chapter.

4 Observation of IG waves

In order to implement the free IG wave model using a spectral approach, we are going to make use of various sets of observations. It is important to have observations with different regional settings in order to firstly calibrate and then validate the parametrizations of free IG levels in the model. Different regional datasets will be used ranging from the Duck 94 campaign carried out near Duck, North Carolina, to the IGALTI campaign around Oahu Island in Hawaii.

We will also explore additional measurements of IG waves in deeper waters and on oceanic scales using historical tsunameter data as well as from seafloor mounted OBS hydrophones. This will be later used for testing the model on a global scale.

4.1 Observation on the shelf: Duck94 campaign

The first set of observations analyzed here was recorded on a wide continental shelf near Duck, North Carolina. The dataset are from the Duck94 campaign where the variability of infragravity motions on a wide continental shelf was examined with data from bottom pressure recorders. Several bottom pressure recorders were deployed along a 100km-long cross-shelf transect extending from the beach (6m depth) to the shelf break (87 m depth) for 4 months during the fall of 1994. A summary of the locations and depths of the sensors are given in Table 4.1 Location coordinates of pressure sensors for Duck94 and their location map are shown in Figure 4.1

The observed infragravity motions in this region are a mixture of forced waves, phase-coupled to local wave groups, and free waves. Although the contribution of forced waves to the infragravity energy increases with both increasing swell energy and decreasing water depth, the shelf is usually dominated by free waves (Evangelidis, 1996). Detailed 1Hz sampled measurements are available which would allow for a first validation of the methodology.

Station	Longitude	Latitude	Depth (m)
'A'	-75.737297	36.1900000	10.1
'B'	-75.69960	36.2040667	20.0
'C'	-75.586403	36.2467533	25.2
'D'	-75.424332	36.247005	30.3
'E'	-75.267502	36.387497	34.2
'F'	-75.151337	36.414997	31.9
'G'	-74.949502	36.501167	43.0
'H'	-74.829002	36.569337	48.7
'I'	-74.764657	36.596168	85.3

Table 4.1 Location coordinates of pressure sensors for Duck94

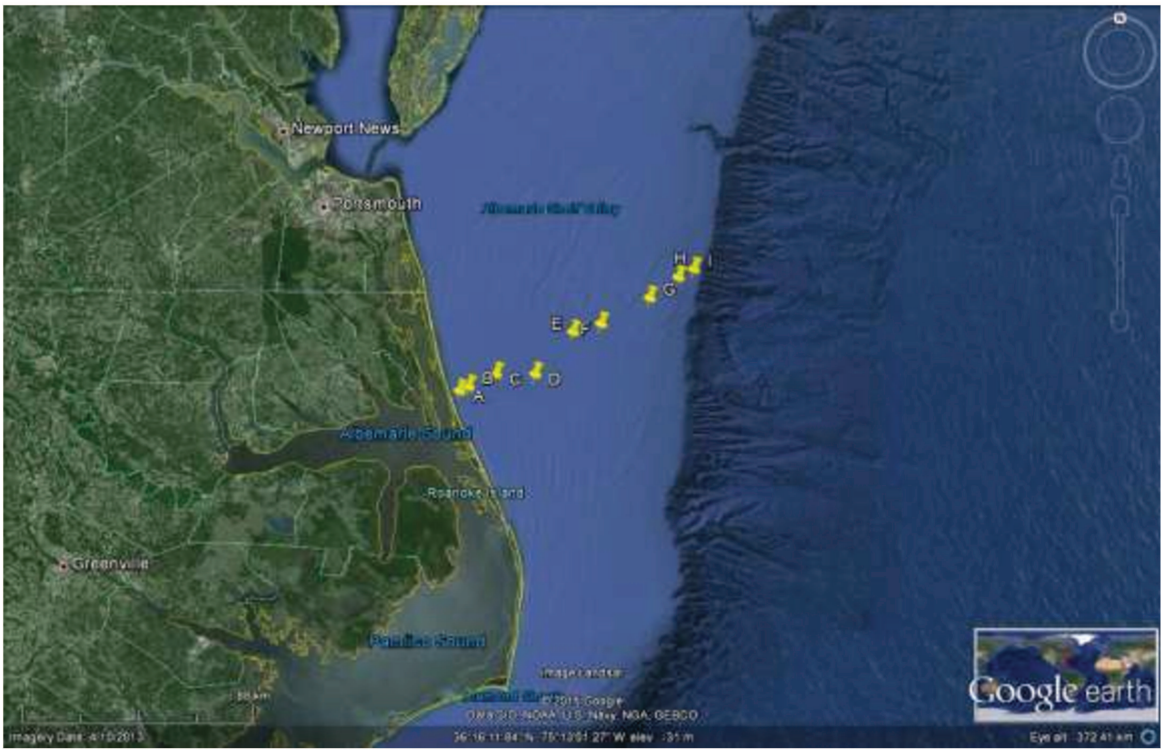

Figure 4.1: Location map of pressure sensors used in Duck94.

We calculated the wave spectra over 3-hour windows. The time series of the measured energy spectra over the deployment period recorded at stations A, C, G and I are shown in Figure 4.2.

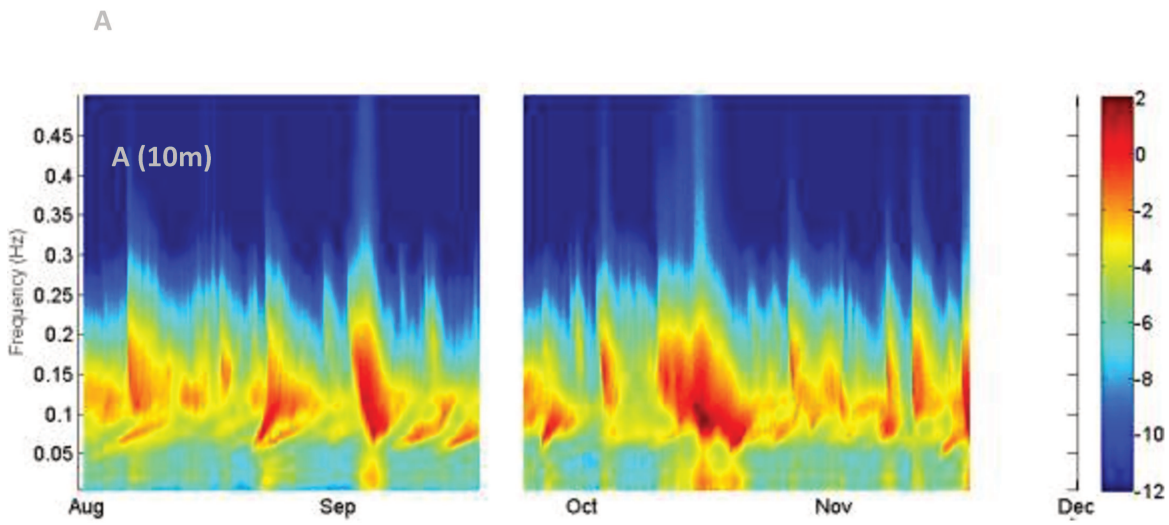

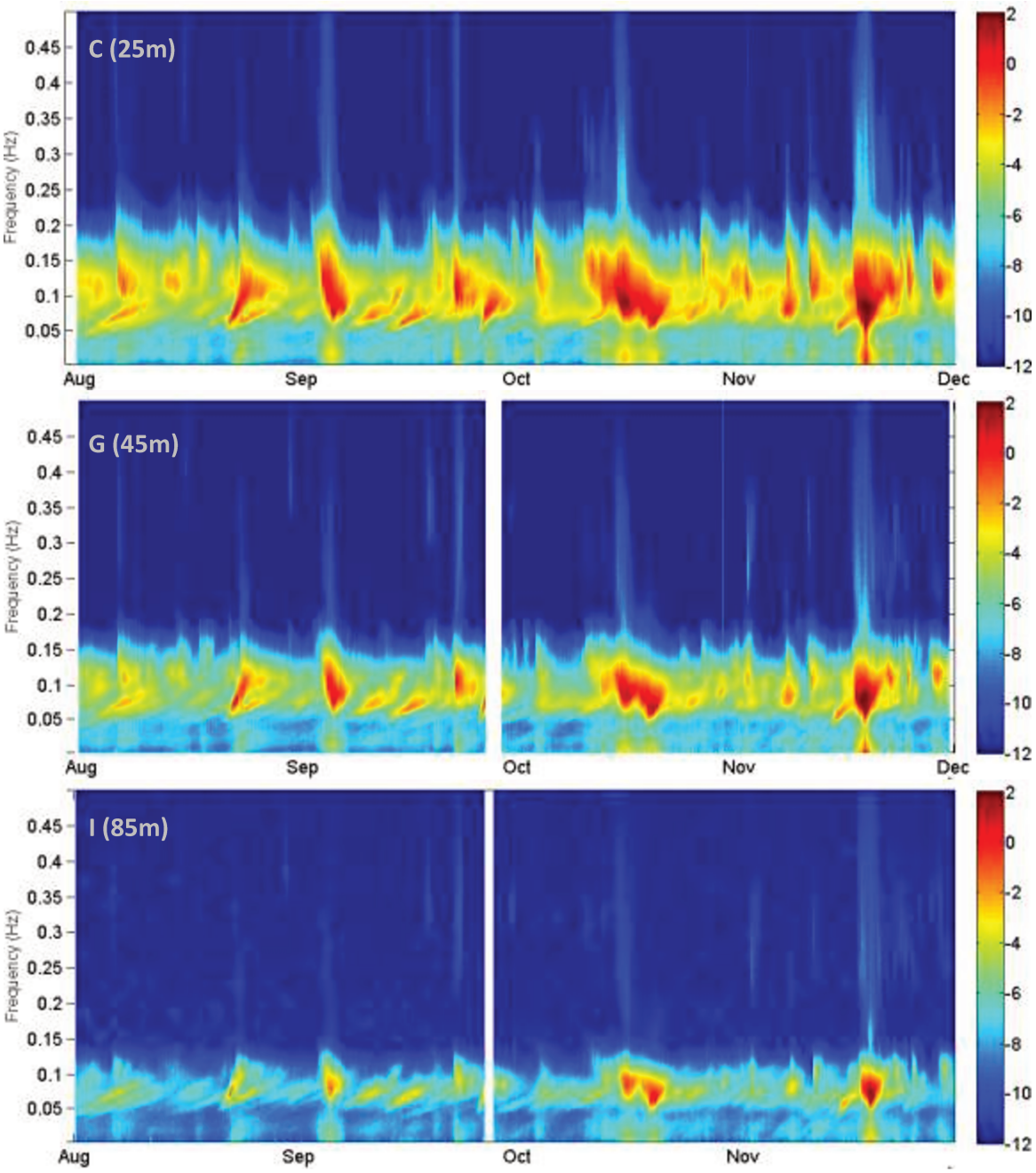

Figure 4.2 Time series of the bottom pressure spectra for the months of August to November 1994 for different stations (in log m^2s). The faint signals being observed above 0.15 Hz at stations G and I are the double frequency signal. Also at station I, numerous peaks of far IG can be seen. These are more difficult to observe in shallower records due to the higher 'ambient' IG levels.

The average spectra calculated for stations A, C, G and I are shown below.

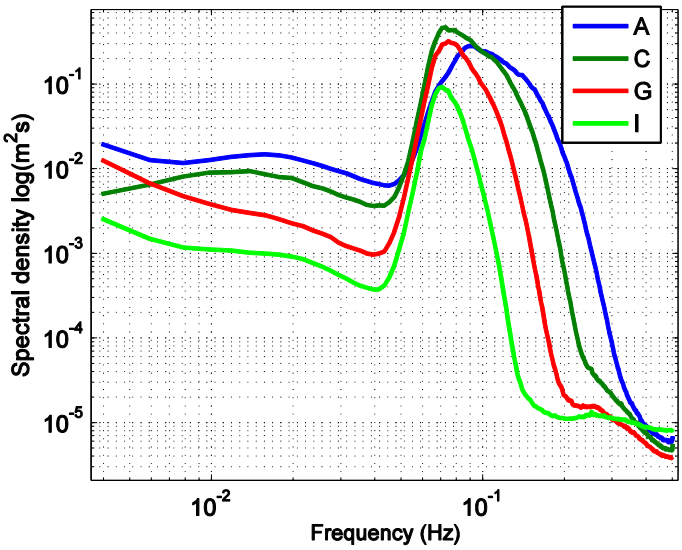

Figure 4.3 Average measured spectra at stations A, C, G and I.

The time series of the measured significant IG wave height over the deployment period recorded at stations A, C, G and I are shown in Figure 4.4. The significant IG wave height H_{IG} was defined from a partially integrated spectrum as

$$H_{IG} = 4\sqrt{\int_{fmin}^{fmax} E(f)df} \tag{4.1}$$

We choose to set $f_{\min}$ to 5 mHz and $f_{\max}$ to 40 mHz so as to exclude possible low frequency swell and compare only IG waves.

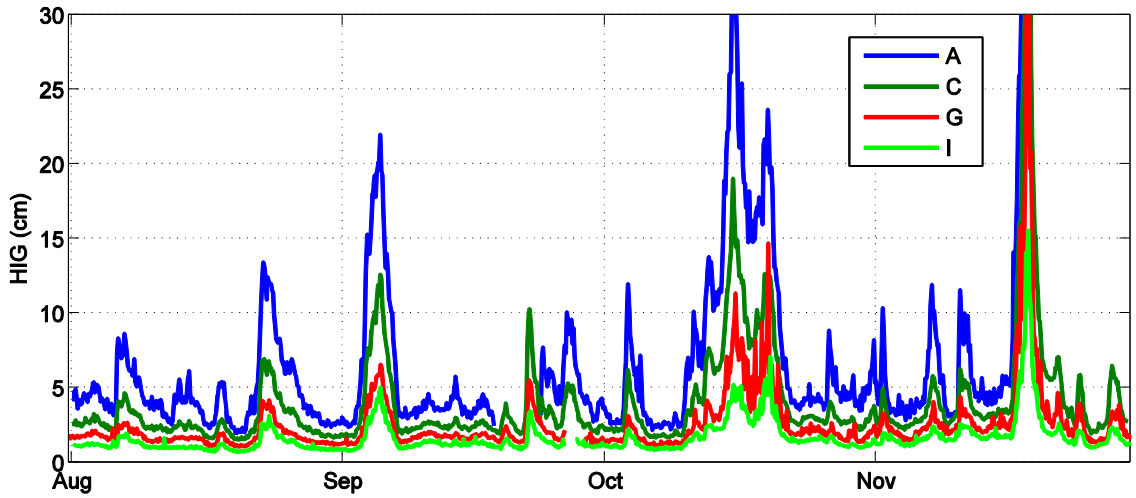

Figure 4.4 Time series of significant wave heights measured by the BPR in the frequency range of 0.005Hz to 0.04Hz

4.1.1 Linear theory depth correction

It can be observed from Figure 4.2 and Figure 4.3 that higher frequencies tend to fade out as the sensors get deeper. This is because the higher frequencies are being more and more attenuated by the water column. To be able to normalise the different measurements, the recorded pressure spectra must be converted to equivalent sea surface elevation spectra using a linear theory depth correction.

For a free monochromatic wave of wavenumber k, the bottom amplitude of pressure p_b is related to the surface elevation amplitude a, by a transfer function M that depends on the wavenumber and the water depth D, (e.g. Aucan and Ardhuin, 2013)

$$p_b = aM = a\frac{\rho g}{cosh(kD)} \tag{4.2}$$

where ρ is the water density, g is gravity acceleration. The wavenumber k, is related to the wave frequency f by the dispersion relation. A Fourier analysis was performed on each bottom pressure record to obtain the bottom pressure power spectral densities $Fp(f)$. The transfer function M, is then applied to obtain the surface elevation spectral density $E(f)$,

$$E(f) = F_p(f)\left(\frac{cosh(kD)}{\rho g}\right)^2 \tag{4.3}$$

The correction is small at infragravity frequencies and shallow water depths as shown in Figure 4.5 for sensor I which was deployed at a depth of about 85 meters. The correction becomes significant for deeper waters as will be seen later.

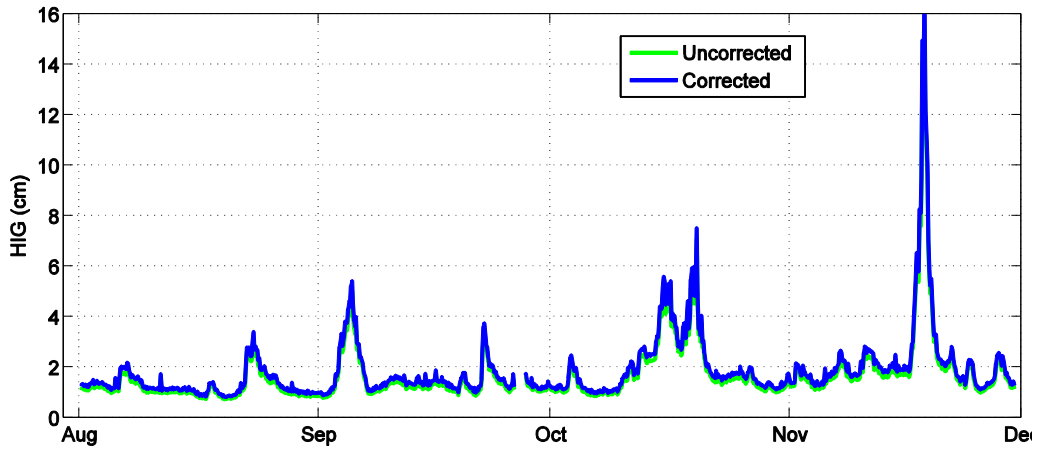

Figure 4.5 Effect of linear theory depth adjustment on the measured wave heights for a depth of 85m, integrated in the frequency range of 0.005Hz to 0. 04Hz.

4.1.2 Effect of background IG

It is suspected that the observed IG signals contain a certain level of background 'noise' which, apart from instruments noise, could be background IG energy from different

sources both inside and outside the region.

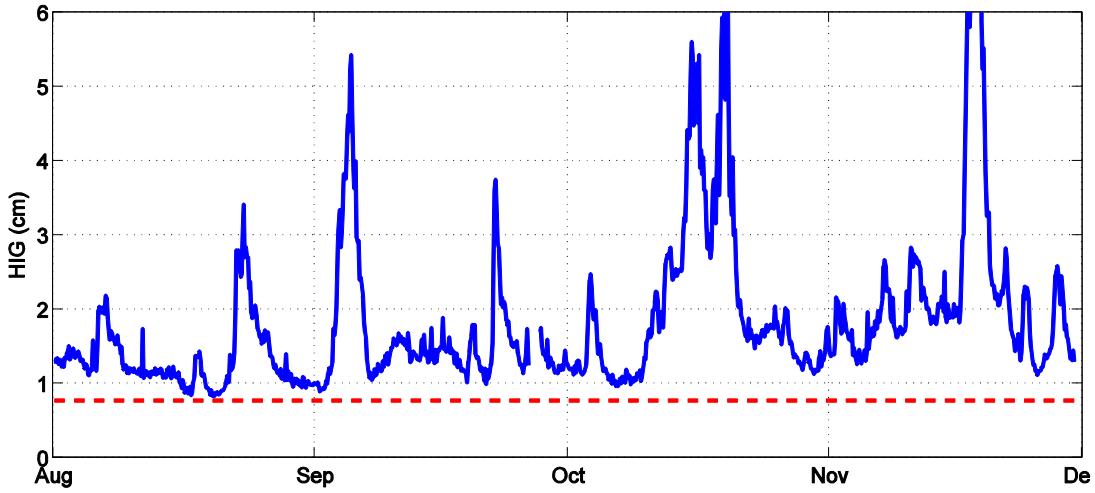

Figure 4.6 Time series of HIG at station I showing a level of background IG (red dashed line) that was defined as the lowest observed IG level during a certain time window.

As seen in Figure 4.2 and Figure 4.6 there seem to be a certain background IG level This is present even during relatively calm sea states and sometimes even where there don't seem to be free IG coming from outside. Although this background IG does not appear to be really constant, for simplicity can define it as the lowest observed IG level during a certain time window. Whichever the source of this background IG, and its spectral shape, it is going to modify the level and spectral shape of the locally generated IG as 'seen' in the observations. However estimating and filtering this background level is very difficult.

An interesting exercise would be to remove different levels of noise from the observed IG levels and see the effect on the IG frequency distribution. The simplest way would be to subtract white noise, assuming a flat noise distribution in the IG band. The effect of removing different amounts of white noise from the measure signal at station I is shown in Figure 4.7 below.

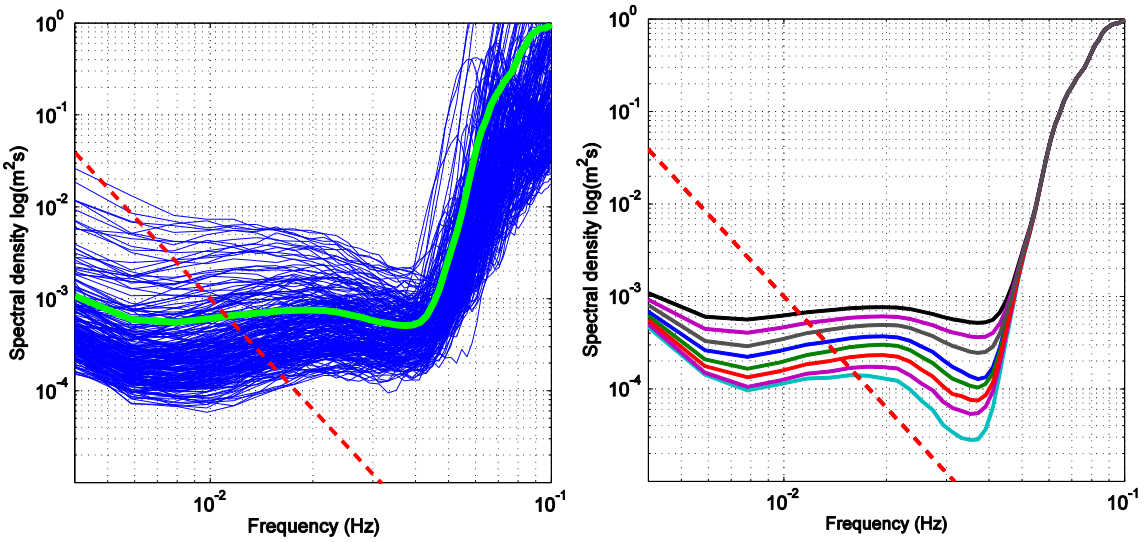

Figure 4.7 Shape distribution of 3 hour spectra at station I (left). The solid green curve shows the average spectra and the effect of removing white noise from the observed IG levels at sensor I (right). The noise was removed from each 3 hour spectra over the whole period before averaging. The black curve shows the original spectra and the red dashed line shows the f^{-4} variation.

Basically, the removal of increasing amounts of white noise from the observed spectra means that we are keeping only higher and higher energy (mostly local) IG events, and discarding smaller events. The convergence of the spectra between 0.015Hz and 0.02Hz towards the f^{-4} asymptote seem to suggest that the coastal generation of IG waves is at least partly driven by the normalised bed slope through reflection at the shoreline.

4.1.3 Estimating bound IG using the Bispectra

Due to the relatively shallow depths at which the observations were made, the recorded IG levels are expected to contain a certain proportion of bound IG energy. Two possible methods for estimating the forced part of the IG spectrum were proposed by Herbers et al., (1994). Firstly, the bound IG part could be directly calculated from the directional spectra using the 2nd order coupling coefficients. Alternatively bispectral analysis can be used to differentiate the bound part from the total IG spectra. Both methods should yield comparable results according to Herbers et al. (1994) but here as no collocated directional short waves spectra were available we use the bispectral method.

The method is based on the fact that forced waves are phase-coupled to local swell, while free waves do not contribute to the bispectrum (Herbers et al. 1994). Bispectra fall in the category of higher-order spectra, or polyspectra and provide supplementary information to the power spectrum. The bispectrum is by definition the two dimensional Fourier transform of a third order cumulant. Analogous to the second-order energy density spectrum the third-order bispectrum $B(f, \Delta f)$ is defined as (Hasselmann et al . 1963) :

$$B(f,\Delta f)df d\Delta f = 2E\{dP(f)dP(\Delta f)dP(-f-\Delta f)\} \tag{4.4}$$

where $E\{\ \}$ is the expected value, Δf the difference-frequency in the infragravity band, f the whole frequency band, and $dP(f)$ is the Fourier- Stieltjes transform of the pressure time series $p(t)$

$$p(t) = \int_{-\infty}^{\infty} dP(f)\exp(2\pi i f t) \tag{4.5}$$

An estimate of the contribution of forced waves to the total infragravity variance (over the frequency range Δf from 0.005Hz to 0.05 Hz) is obtained by integrating the bispectrum $B(f, \Delta f)$ over all pairs of swell components (frequencies f, Δf) (Herbers et al., 1994) for details).

$$b_i(\Delta f) = \frac{2\int_{\Delta f}^{\infty} df\ B(f,\Delta f)}{\left[2\int_{\Delta f}^{\infty} df\ \ E(f+\Delta f)\,E(f)\,E(\Delta f)\right]^{\frac{1}{2}}} \tag{4.6}$$

The ratio between the non-linearly bound and total infragravity energies for each frequency bin is then approximately given by

$$\frac{E_{IG\ forced}(\Delta f)}{E_{IG\ total}(\Delta f)} \approx \alpha_i(\Delta f)|b_i(\Delta f)|^2 \tag{4.7}$$

The coefficients α_i (defined in Herbers et al., 1994) are assumed to be 1, even though a small negative bias ($\alpha_i > 1$) was noted. The method should be valid up to 0.05Hz. Figure 4.8 presents the estimated mean levels of bound IG at sensors A, C, G and I, obtained using this method.

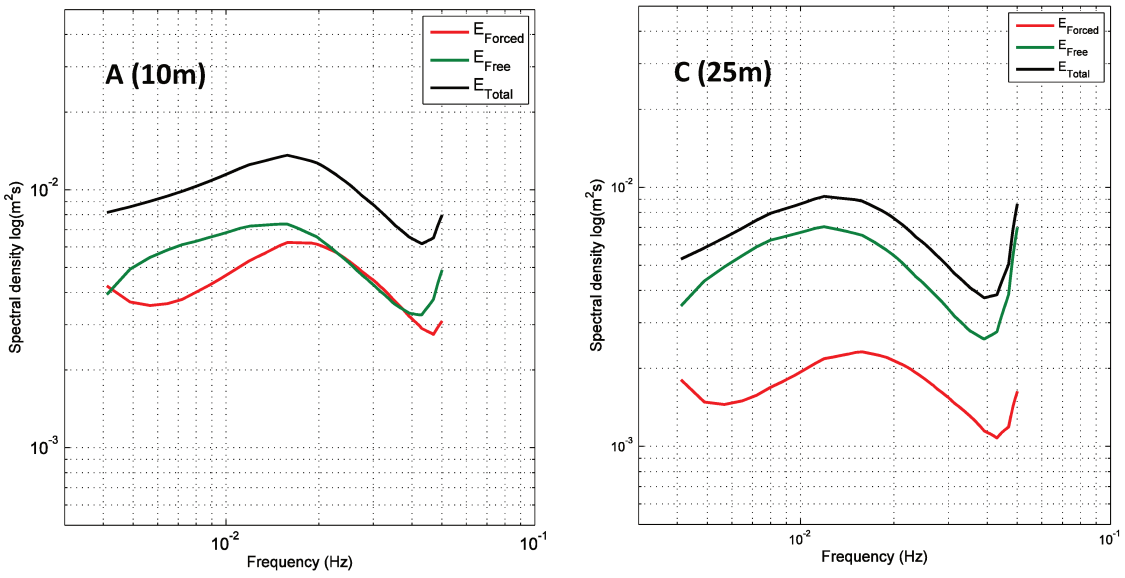

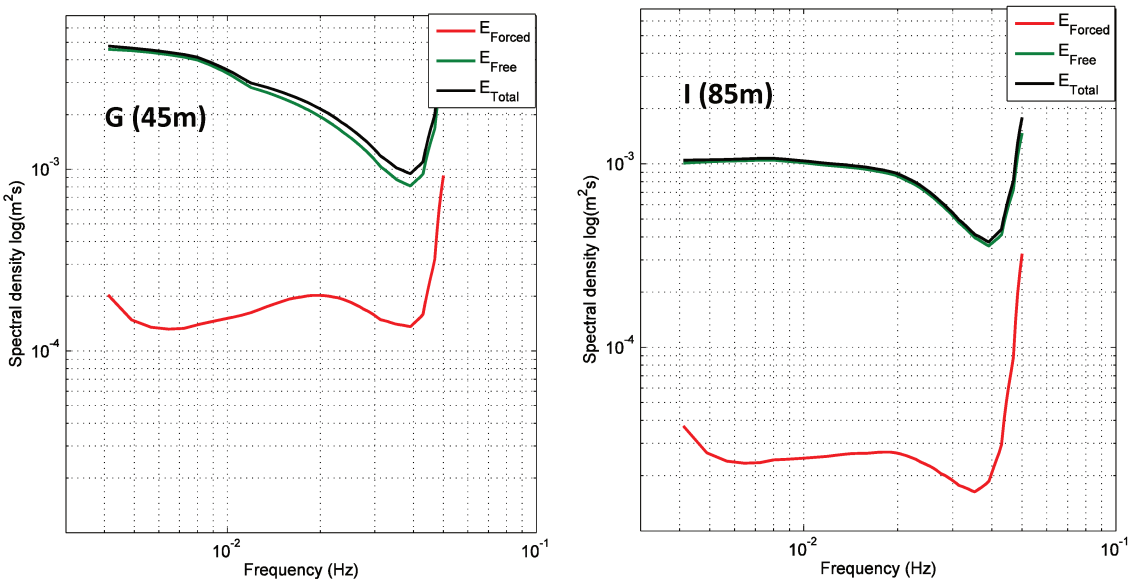

Figure 4.8 Average levels of total (black curves), forced (red curves) and free (green) IG wave energy at sensors A (top left plot, 10m deep), C (top right plot, 25m deep), G (bottom right plot, 45m deep), and I (bottom plot, 85m deep), estimated using the bispectral analysis.

The estimated bound IG levels are consistent with the depth variation indicating that they are being correctly estimated, although it would be difficult to verify these values. The bound IG levels vary from being in the same order of magnitude as the free IG levels at sensor A to being negligible at 85m depth at sensor I. The average bound IG level at sensor A seems to be at the same level as free IG in the frequency band 0.02Hz - 0.04Hz.

It should be noted that the bound IG time series is quite noisy but averaging the spectral distribution over time gives a smooth average. The error margin is probably quite high though, and it would be difficult to remove the bound IG from the measurements.

4.2 Observation in Intermediate Depths: Hawaii

In this section we explore observations from the on-going IGALTI pilot experiment (Aucan and Ardhuin, 2013). The experiment consisted in the deployment around Oahu Island of several bottom pressure recorders (BPR) since the beginning of 2012 in a cross-shore line from the surf zone to the deep-ocean. Deployment locations consisted of one site near the surf zone (~ 15 m), one site at intermediate depth (~165 m), and two sites in the deep ocean, on the abyssal slope at around 2000 m.

The first phase of the IGALTI pilot experiment started with the deployment of an intermediate depth SBE 26+ pressure sensor off the coast of Waimea. This was done at a depth of about 165m under an existing moored directional wave measuring buoy (Waimea Bay waverider buoy). This phase lasted about 3.5 months (105 days) in

February-April 2012. The combined data from the BPR and the wave buoy would allow the estimation the bound IG energy in the recorded signal. The location map of the deployment is shown in the figure below.

Figure 4.9 Location map of pressure sensor deployed around Oahu during the first phase of the IGALTI pilot experiment

While the focus is primarily on free IG generated at the nearby coastline, we will also likely capture events of free IG generated at distant coastlines. Given the island topography and the location of this field study, free infragravity waves impinging on the island from all directions will refract around the island and will be measured at this site. Due to the depth, the IG signal is expected to contain mostly free IG with low levels of forced components.

4.2.1 Bottom mounted pressure sensor

The self-contained pressure recorder measured pressure continuously at 1 Hz for the duration of the experiment. The mooring consisted of an anchor, a pair of acoustic releases, a chassis supporting the pressure recorder, and flotation for the recovery of the mooring. The acquired measurements included the pressure (in cm equivalent) totalling 209 bursts of 12 hours each sampled continuously at 1Hz.

The first step of the data processing was to calculate the wave spectra. 3-hour windows were chosen as the best compromise between noisiness and smoothing. The time series of the energy spectra over the deployment period is shown in Figure 4.10 below.

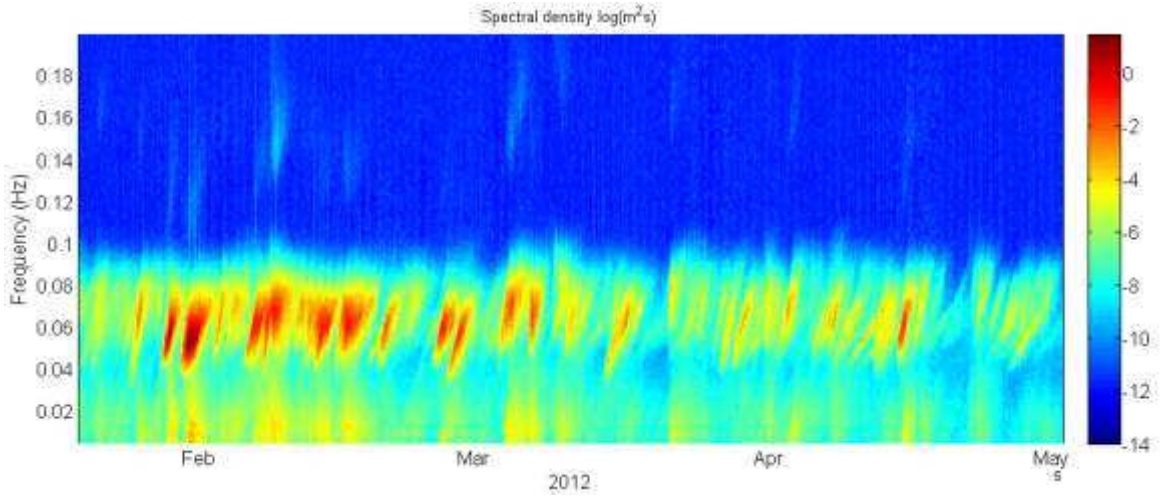

Figure 4.10 Time series of the bottom pressure spectra over the deployment period (in log m^2s). The faint signal being observed above 0.1 Hz is the double frequency signal.

It should be noted that although a sampling frequency of 1Hz was used, the spectrum shows noticeable energy up to only around 0.1 Hz with only very weak energy observed between 0.1 and 0.3 Hz. Most of the higher frequency signal is attenuated by the water column.

The next task was the conversion to equivalent sea surface elevation spectra using the linear theory depth correction (equations (4.2)and (4.3)). As shown in Figure 4.11, the correction can be quite significant for this depth, especially for frequencies above 0.02 Hz. However for this depth the correction works correctly up to only 0.1 Hz, above which the depth-adjusted energy explodes, indicating that we are into instrument noise levels.

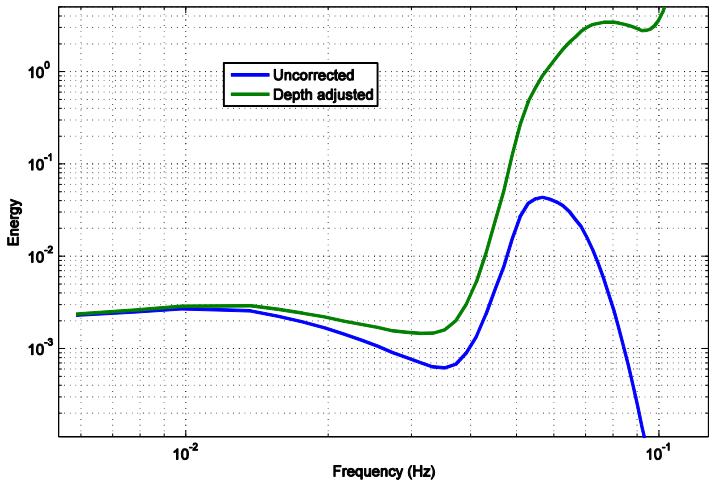

Figure 4.11 Effect of linear theory depth adjustment on the average spectra measured by the BPR (m^2s). The correction seems to be valid up to 0.1Hz.

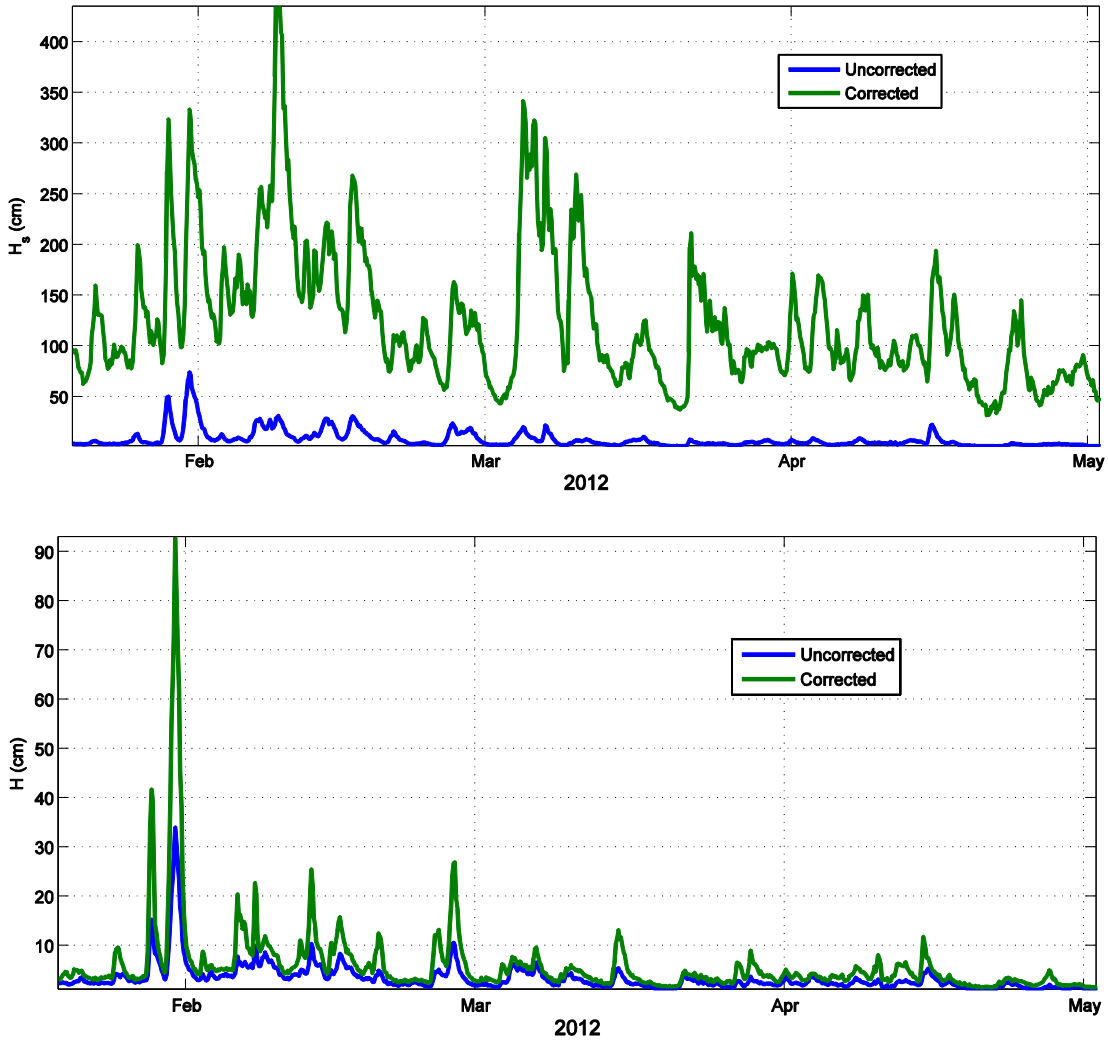

Figure 4.12 Total corrected (green curves) and uncorrected (blue curves) significant wave heights measured by the BPR in the frequency range of 0.002Hz to 0.1Hz (top) and in the frequency range of 0.002Hz to 0.05Hz (bottom)

4.2.2 Directional waverider

The directional waverider data come from Waimea Bay waverider buoy (CDIP 106, Waimea Bay) owned and operated by the Uiversity of Hawaii Sea-Level Center (UHSLC). This spherical buoy is equipped with a gimballed 3-axis accelerometers and a compass. After standard processing, it provides 30 minutes averaged spectra and co-spectra of the 3-axis displacements over the frequencies 0.03 to 0.6 Hz. This buoy was already in place at the beginning of the experiment and the data readily available at no cost.

The water surface (z) was provided in cm with time in datenum format while the 2D Spectra (buoy_S) were provided in m2/Hz/degrees, with 64 frequency steps from 0.025 Hz to 0.58Hz, and 72 directions. Figure 4.13 below gives the measured Hs and frequency spectra.

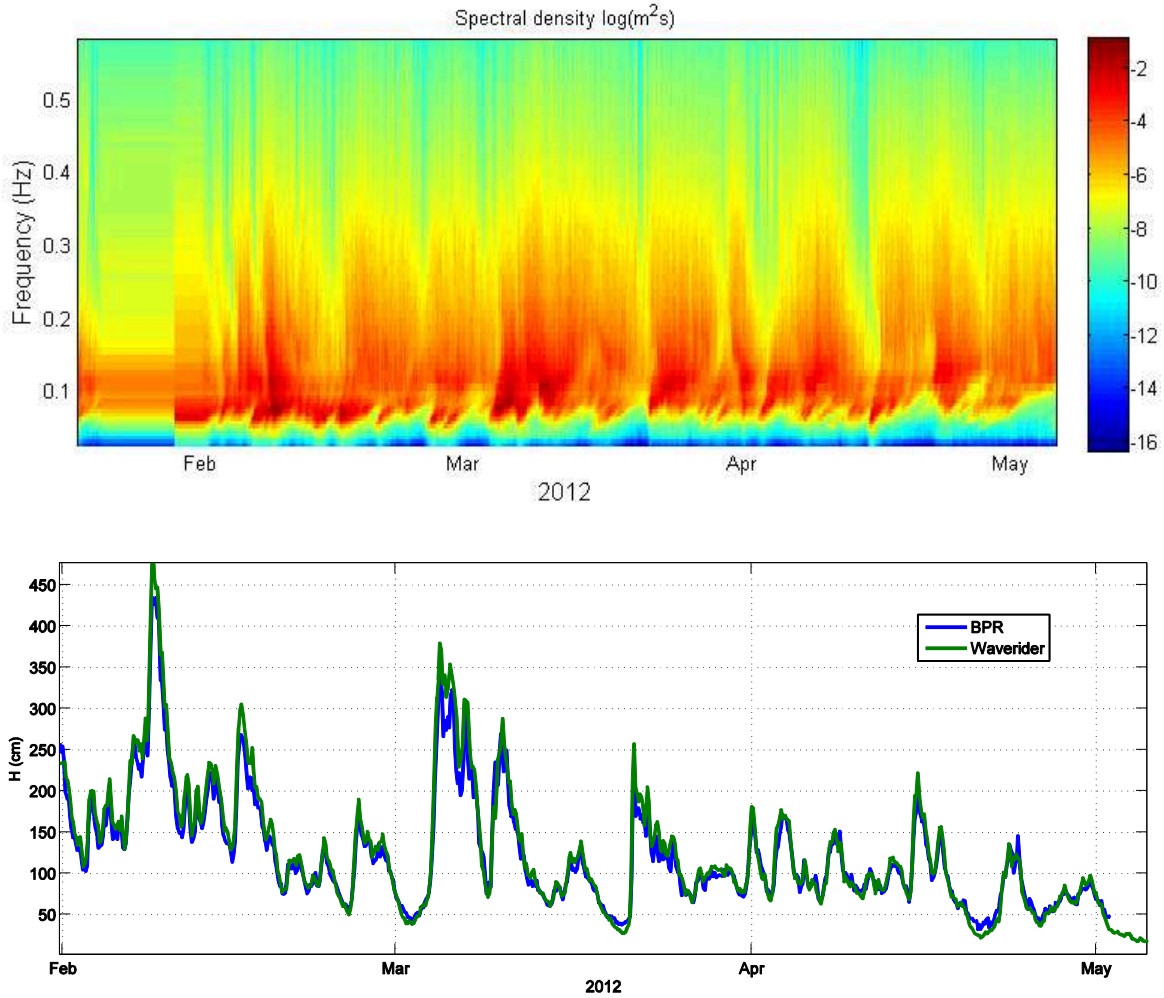

Figure 4.13 Time series of the waverider energy spectra (top) and Hs measured by the BPR (corrected for surface elevation) and the waverider integrated over 0.025 Hz to 0.1Hz (bottom). The convergence of both measurements indicates the validity of the linear theory depth correction.

4.2.3 Analysis of spectral shape

As with the Duck94 observations, it is quite probable that the observed IG signal contains a background 'noise' which, apart from instruments noise, could be background IG energy from different sources both inside and outside the region. As in the previous section, we remove white noise, assuming a flat distribution in the background IG band. The effect of removing different amounts of white noise is shown in Figure 4.14.

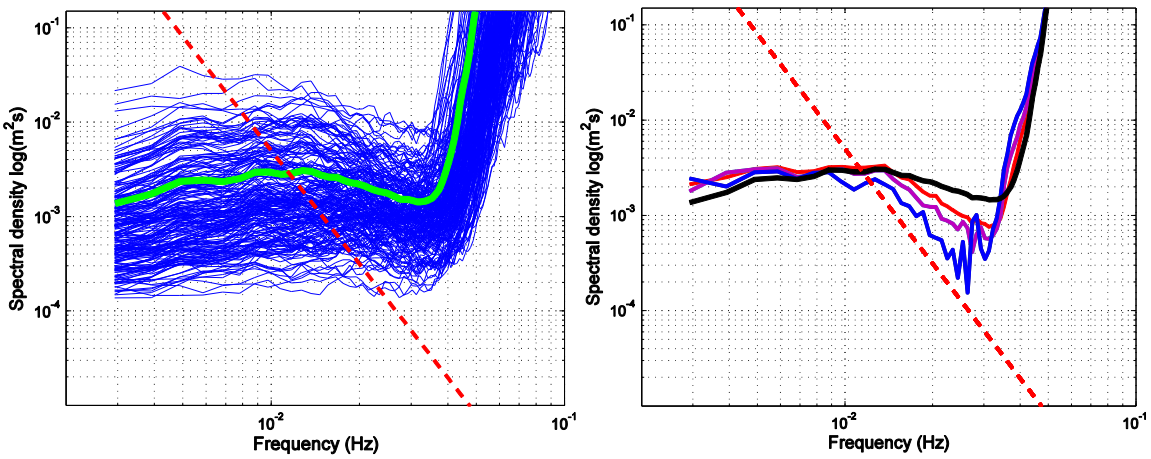

Figure 4.14 Shape distribution of 3 hour spectra (left). The solid green curve show the average spectra. Effect of removing white noise from the observed IG levels (left). The noise was removed from each 3 hour spectra over the whole period before averaging. The black curve shows the average of original spectra and the red dashed line shows the f^{-4} variation.

Here also, the removal of a certain amount of white noise from the observed spectra seem to make the spectra between 0.015Hz and 0.02Hz convergence towards the f^{-4} asymptote suggesting that the IG generation near the coast includes reflection diven by the normalised bed slope. This supports the IG liberation/reflection strategy, for at least the topography at Waimea. It should also be noted that in the case of Waimea, the tidal range in very low, about 0.5m, which implies that the variation of beach slope from high tide to low tide is also low.

4.2.4 Estimating levels forced versus free IG levels

The detailed sea-surface directional spectrum available throughout the duration of the experiment, allows the estimation of the bound IG part using equation (2.13). As previously, we use the surface elevation coupling coefficient (D_s). Figure 4.15 shows the corresponding bound IG Significant wave heights we computed from the directional waverider spectra (over the frequency range 0.005-0.04 Hz).

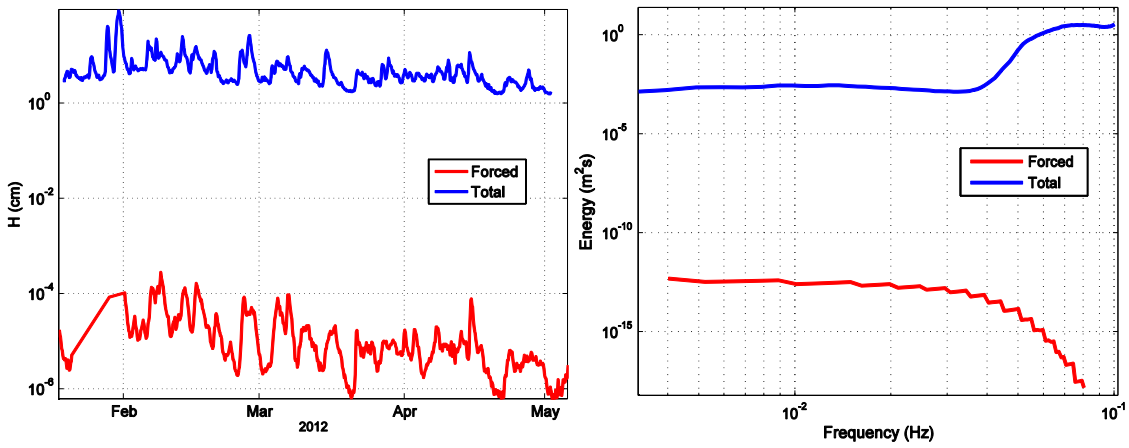

Figure 4.15 Predicted significant Bound IG computed from directional spectra and total IG wave heights (left) and non-directional spectra (right)

It can be observed that the forced-IG values are very low, remaining less than 0.5mm throughout the whole period of study. This indicates that free waves dominate the infragravity band and this location which is quite normal for the water depth being considered. Filtering bound IG is not really required for calibration purposes.

4.3 Observation in the open sea: DARTs and OBS

We are now going to analyse several available observations in the open sea which would then be used to validate the modelling of IG fields on the global scale. In the case of deep sea observations, the observable frequency band is very limited. At 4000m for example, the IG signal can be observed up to only 0.012Hz. Above this, the IG signal is too attenuated by the water depth. There is thus not much data on the shape of the whole IG band in the deep sea. Among the available observations are tsunameter data scattered across the globe as well as records from seafloor mounted hydrophones.

4.3.1 Deep-ocean Assessment and Reporting of Tsunamis (DART) systems measurements

On the global scale, historical tsunameter measurements provide a high-quality dataset. The Deep-ocean Assessment and Reporting of Tsunamis (officially abbreviated and trademarked as DART®) system is a component of an enhanced tsunami warning system. In the 1980s, NOAA's Pacific Marine Environmental Laboratory (PMEL) developed deep ocean tsunameters for the early detection, measurement, and real-time reporting of tsunamis in the open ocean. During normal operation, the DARTs measure and record the low-frequency movement of the water surface, offering valuable measurements of IG waves over extended periods.

A DART system consists of a seafloor BPR system and a moored surface buoy for real-time communications. In 2003, operational responsibility of DART transitioned from PMEL to the National Data Buoy Center (NDBC). There are currently 39 U.S. owned and

operated DART® buoys installed throughout the Pacific and Atlantic oceans. The international community has also taken an interest in DART buoys and as of 2009 Australia, Chile, Indonesia and Thailand have deployed DART buoys to use as part of each country's tsunami warning system. Historical high-resolution (15 seconds sampling rate), edited BPR Data, along with accompanying metadata, can be downloaded from the NDBC website.

However most of the high resolution data are not available from DART stations after the year 2008. For deployments after 2008, high resolution recordings were not continuous but were rather set off by alerts of an impending tsunami. They are hence not appropriate for the study of IG waves. Also the numerical wave model is most reliable for recent years when winds are best known (e.g. Rascle and Ardhuin, 2013). We have thus focused on the year 2008 for studying DART records.

A summary of the locations and depths of some DART records that are available for the year 2008 are given in Table 4.2 and their location map in Figure 4.16

DART	Longitude	Latitude	Depth	Location
21413	152.114	30.546	5827	West Pacific Near Japan
21414	178.270	48.940	5431	North Pacific
21418	148.695	38.707	5665	West Pacific Near Japan
32411	-90.685	4.999	3155	West-Southwest of Panama
32412	-86.392	-17.972	4326	Southwest of Lima, Peru
41420	-67.654	23.314	5667	East of Miami
41424	-72.466	32.922	5284	East of Charleston
42407	-68.215	15.256	4528	Gulf of Mexico
42408	-86.797	25.410	3259	South-Southeast of New Orleans
43412	-107.000	16.031	3155	Southwest of Manzanillo, Mexico
43413	-100.084	10.846	3399	Southwest of Acapulco, Mexico
44401	-49.986	37.551	5391	Bermuda
44402	-67.927	38.199	4328	US north-east coast
46402	-164.002	51.061	4712	Gulf of Alaska
46404	-128.776	45.863	2738	US west coast
46407	-128.894	42.595	3266	US west coast
46408	-169.848	49.623	5373	US west coast
51406	-125.017	-8.489	4473	Pitcairn Island
51407	-156.526	19.627	4718	Hawaii
51425	-176.241	-9.510	4960	Apia, Samoa
51426	-168.291	-23.301	5659	Southeast Tonga
52404	132.312	20.848	5925	West Pacific Near Taiwan
52406	165.002	-5.293	1826	Northeast Solomon
54401	172.963	-33.019	5851	Northeast New Zealand
55015	160.254	-46.840	5020	Tasman Sea 1

Table 4.2 Location coordinates of some available DART stations for the period of 2008

Most of the DART stations are on the deep sea floor (4000m-5000m), with only a few

below 3000m.

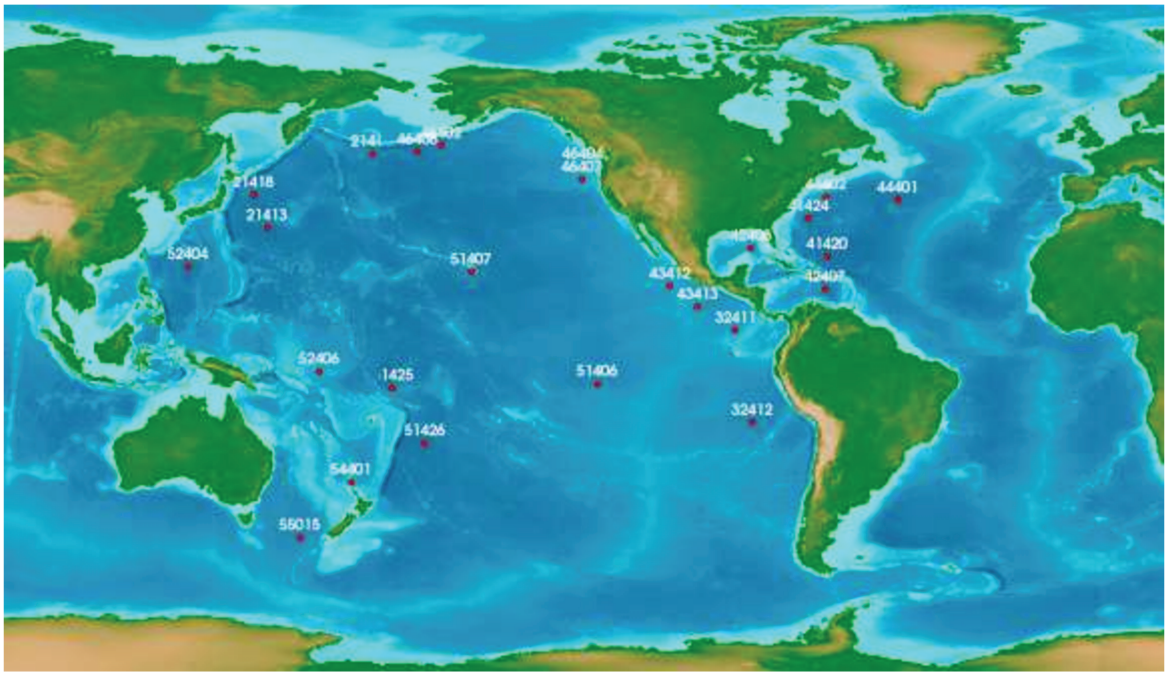

Figure 4.16 Location of available DART records for the period of 2008. Note the scarcity of these records in the in the Indian Ocean, and the South and East Atlantic oceans.

It should be noted that there are some regions such as the Indian Ocean, and the South and East Atlantic oceans where DART records are quite scarce for the 2008 period and even today. The time series of some of these available DART observations for 2008 is shown in figure below.

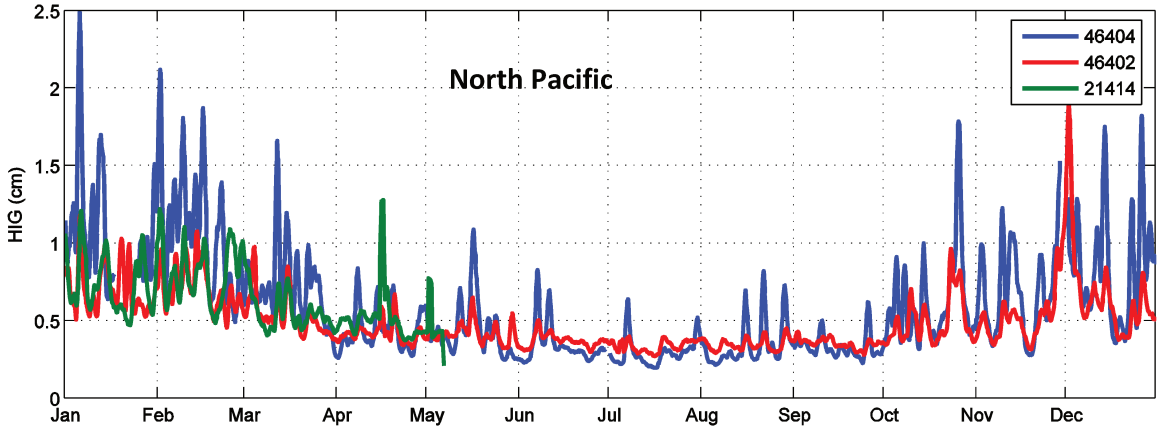

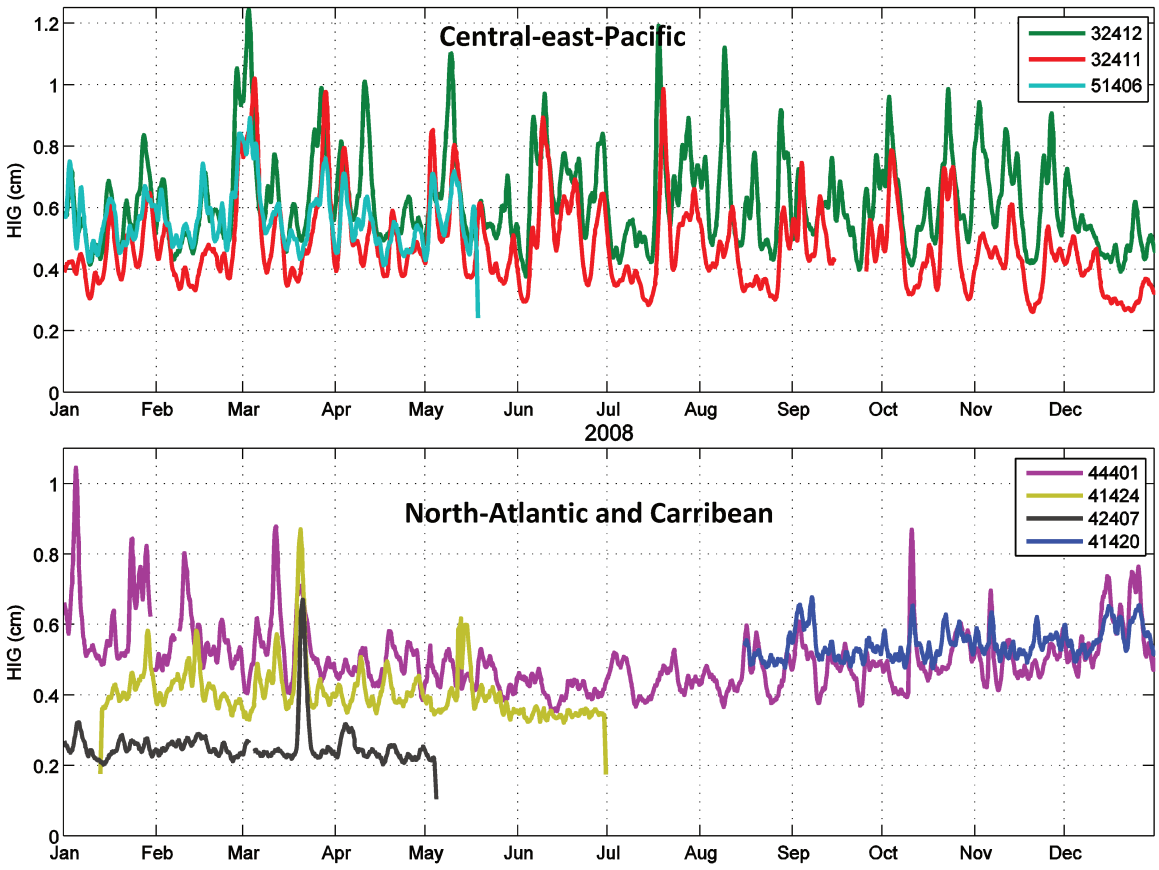

Figure 4.17 Time series of IG levels measured by DART stations at different parts of the Pacific and Atlantic oceans for the year 2008. Pressure values were translated into surface elevation for the frequency range 5 mHz to 12mHz and the temporal resolution is 3 hours.

It can be observed that the occurrence of IG peaks tend to be seasonal for most of the locations. In the northern hemisphere, the peaks tend to be higher and most frequent during winter in both the Pacific and Atlantic oceans. It seems to be also the case in the southern hemisphere during austral winter although the number of records is limited. It can also be observed that different locations can have different noise levels.

4.3.2 MOMAR Observatory

Another interesting dataset containing IG signals was obtained from seafloor monitoring seismometer deployment. The MOMAR (Monitoring of the Mid-Atlantic Ridge) Observatory (Ballu et al., 2006, 2009) was a project initiated by the international InterRidge Programme, to promote and establish a multidisciplinary long-term study of hydrothermal environments at the Mid-Atlantic Ridge (MAR) near the Azores (35°N to 40°N).

The 2007 GRAVILUCK cruise, which initiated an experiment to monitor the deformation of the Lucky Strike volcano used numerous instruments as shown in Figure 4.18. Several differential-pressure sensors measured bottom pressure throughout the duration of the project.

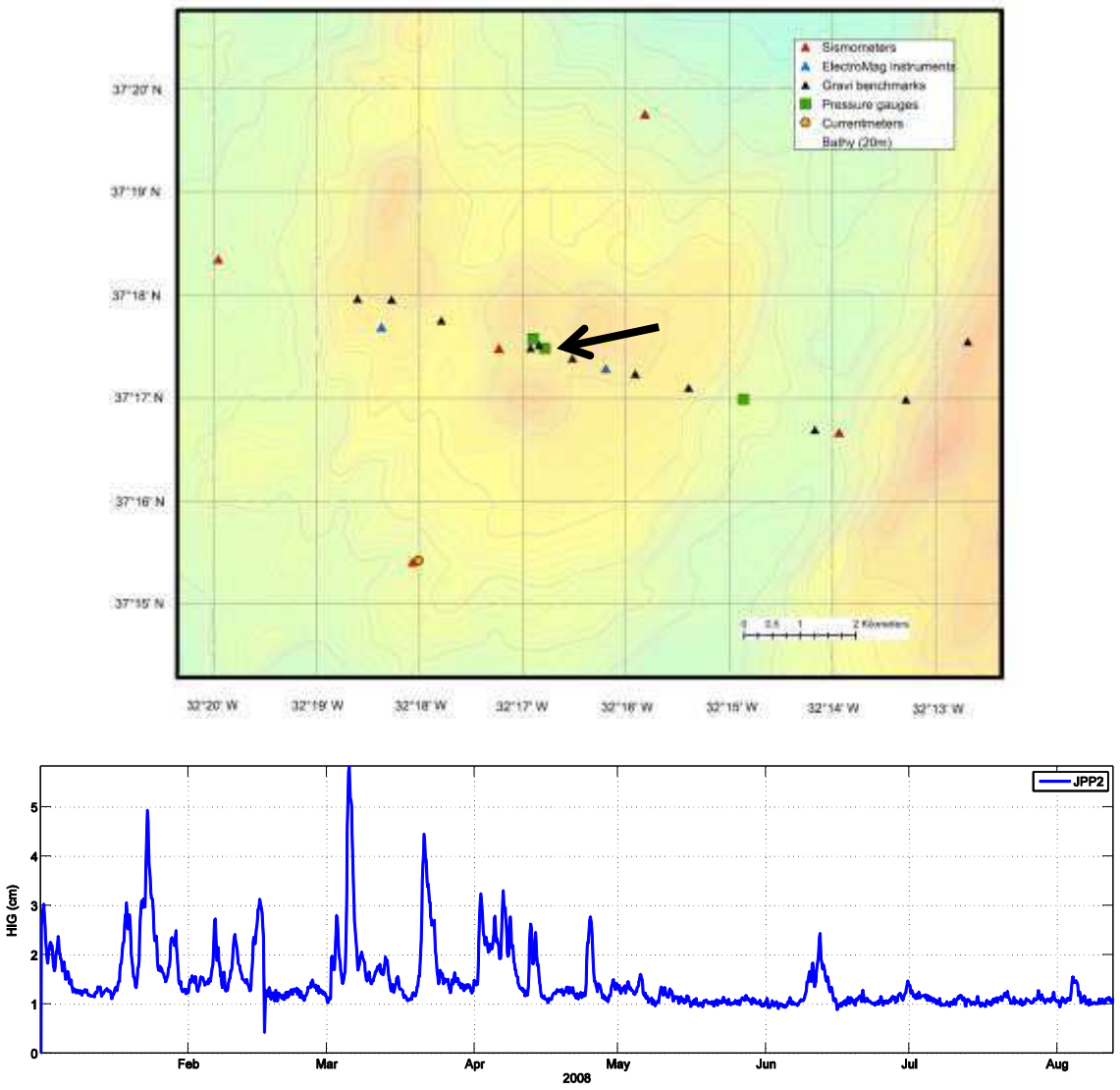

Figure 4.18 Location of various instruments deployed during the MOMAR project and HIG recorded at sensor JPP2 (black arrow) integrated in the frequency range 0.005Hz to 0.02Hz.

The measurement of sensor JPP2 which is located at a depth of about 1800m was used for the study of IG events in the Atlantic Ocean (cf chapter 6 and Rawat et al., 2014).

4.3.3 Observation of IG waves using hydrophones

IG waves can also be detected by hydrophones within ocean-bottom seismometers (OBS). In general, the impacts of oceanographic signals on OBS's records occur through different mechanisms. In the 1s to 20s band, the sea and swell waves are the principal seismic noise source for both terrestrial and ocean floor sites. The seismic noise spectra usually display two peaks in this band which are called primary (PM, 10-20s) and secondary microseisms (SM, 4-10s) (Figure 4.20). The primary and secondary microseism and infragravity waves are always present in the OBS records, however the energy grows in the presence of local and distant storms and higher levels of energy is attained with distant storms.

Other noise recorded in the ocean is the seafloor 'compliance noise' associated with pressure measurements. This noise is noticeable above 30s on the deep seafloor (4000m-5000m) and extends to lower periods at shallower depths. The origin of these elevated noise levels at long periods (greater than 20s) is believed to be the deformation of the seafloor under the pressure of the freely propagating oceanic infragravity waves.

In order to obtain normalized measurements, each hydrophone and the acquisition system need to be properly calibrated with their individual characteristics.

4.3.4 NEAREST project

In the context of the NEAREST project (Harris et al., 2013), continuous recorded data are available from 24 broad-band OBS, deployed in the Gulf of Cádiz. The project lasted from September 2007 to August 2008. The locations of the sensors are shown in Figure 4.19 below.

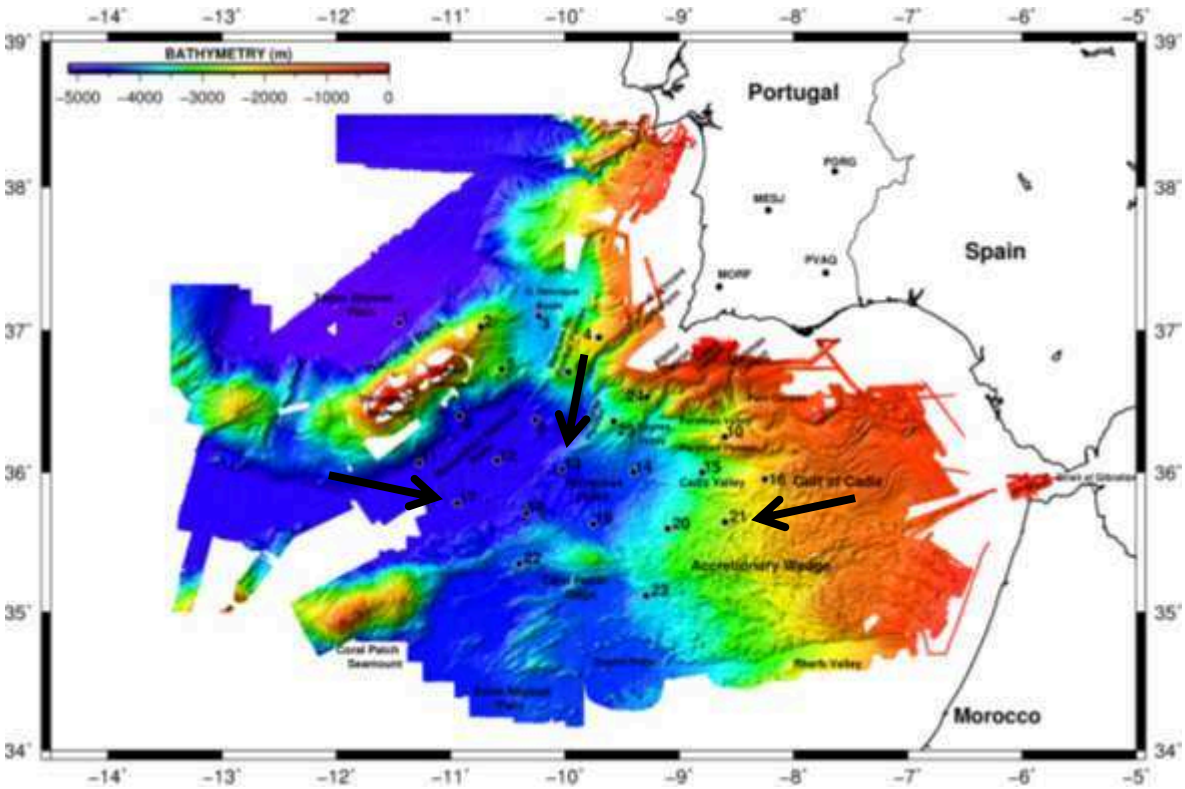

Figure 4.19 Location of the OBS's in the NEAREST experiment (black dots). The black arrows indicate the selected OBS's used for this study.

Data from three OBS stations were used in this study (OBS13, OBS17 and OBS21), after proper calibration of each hydrophone and subsequent normalisation of the data. Similar to bottom pressure sensors, hydrophone data lust be converted to surface elevation equivalence using the linear theory depth correction using equation (4.2).

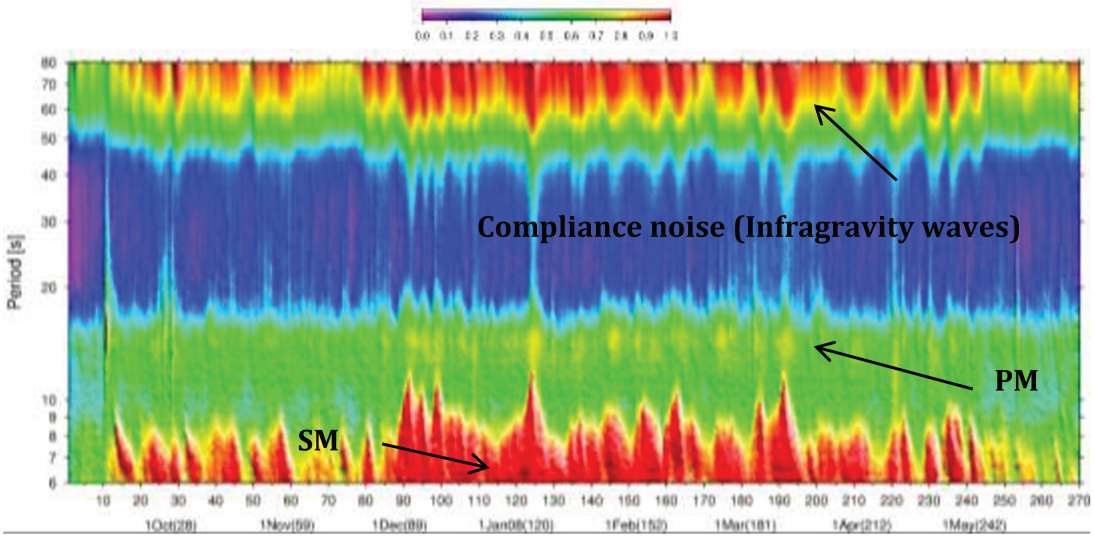

Figure 4.20 The recorded spectra of hydrophone on OBS-17 with secondary and primary microseism and infragravity waves from 3 September 2007 to 27 of May 2008.

In the context of the study of global IG events, discussed in chapter 6 and published in Rawat et al. (2014), this dataset was exploited for the period between 1st January to 15th January 2008. The time series of these three measurements and their average spectra are shown below.

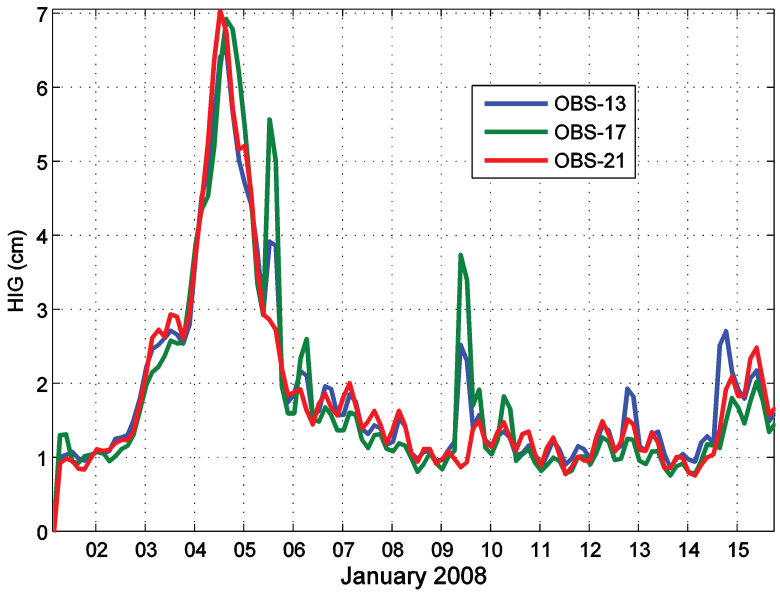

Figure 4.21 Time series of IG wave heights measured by the three stations with linear theory depth correction and integrated over the frequency 0.005Hz to 0.02Hz. The effect of tide cycles can be seen in all 3 observations.

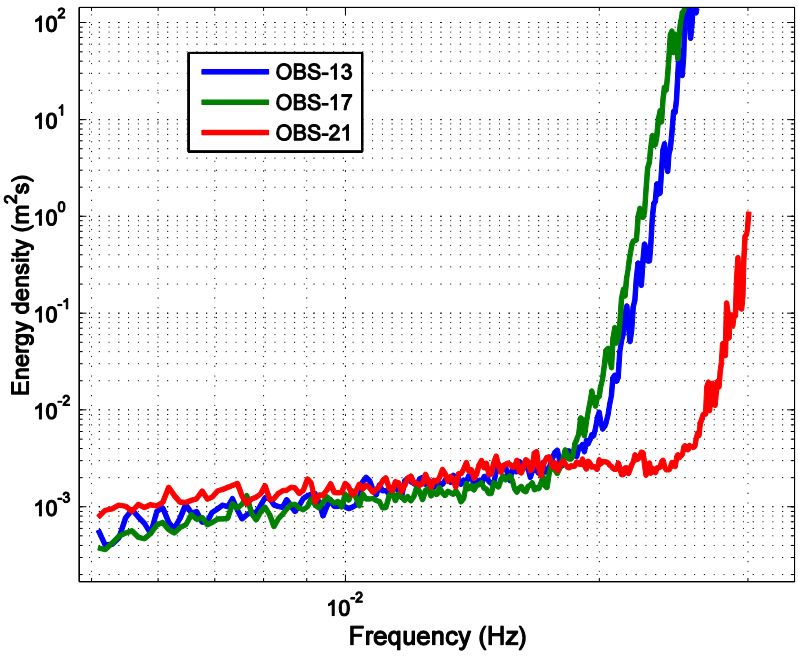

Figure 4.22 Spectra measured by the three OBS, adjusted to sea-surface elevation by linear theory and averaged over the period 1-15 January 2008.

Due to the depths of the instruments, the IG band is valid up to 0.02 Hz for OBS-13 and OBS-17 and up to 0.025 Hz for OBS-21.

4.4 Discussion

It was noticed that the observed IG signals seem to contain a certain background IG level. This is not to be confused with instrument noise, although this cannot be completely excluded. In intermediate waters, when white noise was subtracted from the observed signal, an f^{-4} asymptote seems to emerge. This let us to believe that at least part of the generated IG spectrum contains an f^{-4} signature which is then masked by a flatter IG spectrum.

The origins of this background IG can either be local or offshore. Locally it could probably be from frequency shifts due to nonlinear interactions between the IG waves themselves or with short waves or from interaction between the free IG waves and the topography. The offshore noise would be mainly from remotely generated far-IG. It could also be very low frequency swell overlapping into the IG band, although it is quite rare to have swell waves below 0.04Hz.

It is also possible that the observed signal is a combination of signals from different IG generation mechanisms with only the liberation mechanism containing the f^{4} dependence due to reflection at the shoreline. Also the effect of having IG generation from a wide range of bottom slopes could mask each slope's individual effect.

4.5 Conclusion

We observed the variability of IG wave energy in a wide range of environments, from a regional wide continental shelf to the deep sea. The analysis of the different field observations pointed to the role of the normalized bed slope in shaping the outgoing free IG spectra through the coastal reflection of IG waves.

In shallow waters, the full IG band is covered but the signal is polluted by bound IG (as seen on the shallower sensors in the Duck94 observations). With intermediate-depth bottom pressure measurements (85m-1000m), the full IG band is observable without much pollution from bound IG. As noted in Figure 4.15, the bound IG level contained in the 170m deep signal is negligible.

In the deep sea (>3000m) the bound IG signal is negligible, but the band of observable IG waves at the sea floor would however not exceed ~0.015 Hz. Above this, the IG signal is too attenuated by the water depth. For shorter IG wave periods, (0.015 to 0.04 Hz) we have at present no available observation for the IG energy levels in the deep sea, thus no certainty on the shape of the whole IG band in the deep sea.

The background IG level also seems to be less important in intermediate waters than in shallow waters. This makes the Hawaiian intermediate depth observation ideal for the calibration and testing of an IG model. In the next chapter we will use these observations and deductions to set up an IG parametrization in a spectral wave model, with the final aim of setting up a global IG wave model.

5 IG waves in a spectral model

Because we cannot afford the spatial resolution required to solve over large areas the non-linear phase-dependent evolution of the wave field on the scale of the few wavelengths closest to shore, we chose to use a spectral model which should allow modelling from these regional scale up to the global scale. To achieve this we use the WAVEWATCH III modelling framework (Tolman et al., 2014), which is well validated for wind-generated waves (eg. Rascle and Ardhuin, 2013). The usual sea and swell frequency band is simply extended to lower frequencies to allow for the propagation of free IG waves.

Propagating IG waves with the usual numerical schemes of WW3 poses no particular problem (here we use the third order upwind QUICKEST scheme of Leonard, with the garden sprinkler correction parametrization of Tolman (2002), although this is less efficient than a Lagrangian scheme). The real challenge is to quantify the free IG energy sources and sinks. We are going to parametrize the near-shore source of free IG waves as a function of the incoming short wave spectrum. As investigated in the previous chapter, apart from the incoming short wave field, the free outgoing IG field is expected to be dependent on several local factors including the bottom morphology and local dissipation.

We will in the first section of this chapter review the empirical parametrization proposed by Ardhuin et al. (2014). In the second section we propose another parametrization that uses the bound IG spectrum corresponding to the incoming short waves over a flat bottom. The expected benefit of the second method is that it should be able to reproduce some of the variability in the directional and spectral distribution of the free IG waves, and also try to link the empirical formulation to actual physical mechanisms. The modelled IG waves will be validated using data from the DUCK'94 field experiment (e.g. Herbers et al., 2000) as well as the IGALTI field experiment off Oahu in Hawaii.

5.1 General implementation in WAVEWATCH III

In WAVEWATCH III, the basic spectrum is expressed in terms of the wavenumber-direction spectrum $\mathrm{E}(k,\theta)$ instead of the frequency-direction spectrum $\mathrm{E}(f,\theta)$. The wavenumber-direction spectrum is preferred because of its invariant characteristics with respect to the physics of wave growth and decay for variable water depths.

Moreover the energy spectrum is not always conserved. For example in the presence of currents, work is done by the current on the mean momentum transfer of waves. However the wave action spectrum $\mathrm{N}(k,\theta;\mathbf{x},t) = \mathrm{E}(k,\theta;\mathbf{x},t)/\sigma$ is a conserved quantity even in the presence of currents. This makes the wave action density spectrum the spectrum of choice within WAVEWATCH III. The balance equation for the wave action spectrum $\mathrm{N}(k,\theta;\mathbf{x},t)$ is given as

$$\frac{\partial N}{\partial t} + \nabla_x \cdot \left(\mathbf{c_g} + \mathbf{U}\right)N + \frac{\partial}{\partial k}\dot{k}N + \frac{\partial}{\partial \theta}\dot{\theta}N = \frac{S}{\sigma} \tag{5.1}$$

$$\dot{k} = -\frac{\partial \sigma}{\partial d}\frac{\partial d}{\partial s} - \mathbf{k} \cdot \frac{\partial \mathbf{U}}{\partial s} \tag{5.2}$$

$$\dot{\theta} = -\frac{1}{k}\left[\frac{\partial \sigma}{\partial d}\frac{\partial d}{\partial m} - \mathbf{k} \cdot \frac{\partial \mathbf{U}}{\partial m}\right] \tag{5.3}$$

Where the vector quantity $\mathbf{c_g}$ is given by c_g and θ, s is a coordinate in the direction θ and m is a coordinate perpendicular to s. This equation is valid for a Cartesian grid. For large-scale applications, this equation is usually transferred to a spherical grid. S represents the net effect of sources and sinks for the spectrum. These include amongst others, wind-wave interaction terms, nonlinear wave-wave interactions and dissipation terms (whitecapping, breaking).

WAVEWATCH III also includes, since version 4.05, the representation of coastal reflection by a source term. This source term is zero except at nodes adjacent to land or nodes that are affected by sub-grid islands (Ardhuin and Roland, 2012). These nodes will be termed "coastline boundary points". It was thus natural to introduce free IG forcing in the reflected spectrum at the coastline boundary points. In practice the free IG wave energy is added to the spectrum before the reflection is applied.

As suggested by Herbers et al. (1994), incoming free IG energy from the outside will be fully reflected in most cases because of their perpendicular incidence. There would still be a frequency and bottom slope dependence according to Battjes et al. (2004), and dissipation processes should be accounted for. This incoming free IG energy should hence be added to the outgoing IG spectra after accounting for these processes.

The generated IG would come from either the liberation of bound IG or through the varying breakpoint mechanism, which would also be dependent on the coastal reflection, with the added complexity of trapping. For fine spatial resolutions, the trapping can be directly represented, but for coarse resolutions, it may have to be properly parametrized.

Physically, the generated IG comes from the transfer of energy from the short wave spectra (e.g. Reniers et al. 2010) with a possible feedback of long wave energy to the short waves (Henderson et al., 2006), but the evolution of the short-wave spectra is going to be treated independently using existing parameterisations in WWIII for source terms and reflection coefficients.

Dissipation of IG energy is expected to be due partly to bottom friction, nonlinear transfer mechanism (through triad interactions from low-frequency energy to higher-frequencies) and IG wave breaking at the shoreline. Here we use the existing dissipation

parameterisations in WWIII, which have been validated for short waves and which we assume would also be valid for IG waves (Ardhuin et al., 2014).

5.2 Empirical estimation of Free IG

The main aspect of the free IG model developed by Ardhuin et al. (2014), is the empirical source of IG free waves, which was inferred from coastal measurements in Hawaii, North Carolina and France (Figure 5.1). Based on these datasets, the IG wave height H_{IG} radiated from the shoreline was estimated by

$$H_{IG} \approx \alpha_1 H_s T_{m0,-2}^2 \sqrt{\frac{g}{D}} \tag{5.4}$$

where H_s is the significant wave height of wind seas and swells, $T_{m0,-2}$ is the mean period given by the -2 and 0 moments of the surface elevation spectrum, g is the apparent acceleration of gravity, D is the local mean water depth, and α_1 is a dimensional constant. The choice of wave period $T_{m0,-2}$= $(m_0/m_2)^{1/2}$ with the n^{th} moment, $m_n = \int_0^\infty \int_0^{2\pi} f^n E(f,\theta) df d\theta$, is relatively arbitrary (f being the frequency and $E(f,\theta)$ the directional wave spectrum). Basically, it is less noisy than the usual peak period, and gives more importance to the low frequency part of the spectrum than other mean periods defined from the -1 or +1 moments.

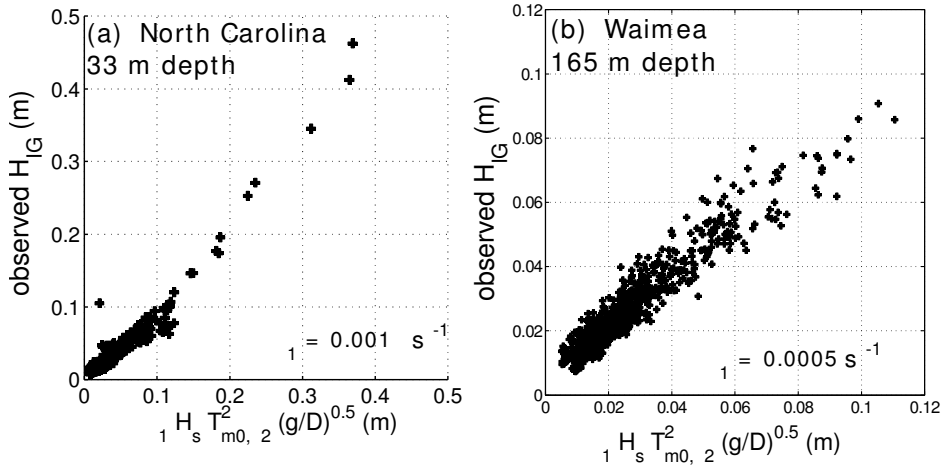

Figure 5.1Measured and parameterized infragravity wave heights at two sites off (a) North Carolina and (b) Hawaii. The measured H_{IG} is compared to the local value of the product of $H_s T_{m0,-2}^2 \sqrt{\frac{g}{D}}$ where α_1 is a locally adjusted parameter.

The observation analysed by Ardhuin et al. (2014), shows that, within a factor of 2, α_1 = 12.e^{-4} s^{-1}. This constant value was used in their global model. Equation (5.4) was extended to any water depth by replacing D by the proper amplification factor for a broad directional wave spectrum for which the energy is conserved.

It was further assumed that an equal amount of energy is radiated in all directions. This

and an empirical distribution across frequencies f provides a value of the directional wave spectrum $E_{IG}(f,\theta)$ that is prescribed in the model at all points adjacent to land,

$$E_{IG}(f) = 1.2{\alpha_1}^2 \frac{kg^2}{C_g 2\pi f} \frac{\left(H_s T_{m0,-2}^2/4\right)^2}{\Delta f} min(1, 0.015\, Hz/f)^{1.5} \sqrt{\frac{g}{D}} \quad (5.5)$$

$$E_{IG}(f,\theta) = E_{IG}(f)/(2\pi) \quad (5.6)$$

where C_g is the frequency-dependent group speed of linear surface gravity waves, the wavenumber k and frequency f are related by the dispersion relation $(2\pi f)^2 = gk\ tanh(kD)$. In practice, the near-shore values of the wave spectrum in the IG band are set to the maximum of $E_{IG}(f, \theta)$ given by eq. (3) and the value given by the reflection of the incident wave spectrum, before the free IG energy is added. This treatment allows for a smooth transition between swells and IG waves.

It should also be noted that with this parametrization, the incoming IG waves are not completely added to the outgoing spectrum and is sometimes completely absorbed at the shoreline. It is rather the maximum between the reflected and the locally generated IG that injected as a source term.

The frequency distribution of the IG spectrum is also empirically estimated by the $(min\ (1, 0.015\ Hz/f))^{1.5}$ factor, which gives a symmetrical bell shape. The model has been well validated on regional and global scales in Ardhuin et al. (2014), and has also been used in Rawat et al. (2014) and Ardhuin et al. (2015) for the modelling of global IG events.

5.3 Parameterizing free IG waves from incoming bound IG

The second approach that we propose here is to estimate the free IG field from the bound IG field, assuming proper spectral transformations that occurs during 'liberation' and reflection at the coastline. This can be done by calculating the bound IG via the 2nd order coupling coefficients near the coast (at the points where liberation occurs) and then to reflect a certain proportion of these calculated waves back as free waves.

The depths at which liberation occurs, $Depth_{IG}$ is assumed to coincide with the point of wave breaking, which can itself be estimated by the maximum wave height criteria, linked to the appropriate γ_{lib}.

The bound IG field is then calculated from the incoming short waves as either an isotropic or a directional spectrum (equations (2.14) and (2.15)). As it has been generally observed that outgoing free IG energy undergoes a high level of refraction, (Herbers et al. 1994) it can hence in some cases be approximated by an isotropic spectrum, in line with Ardhuin et al. (2014).

Once generated, the free IG waves are reflected, and this will determine the part that escapes to the open sea. As recalled by Elgar et al. (1994), Battjes et al. (2004) and Van

Dongeren et al. (2006), this reflection is governed by the normalised bed slope (equation (2.16)). The reflection coefficient, calculated by equation (2.19) is thus dependent of the local bottom slope, h_x, the frequency, f and also the significant wave height, H. We also assume that the reflection coefficient cannot be greater than 1.

We can thus implement this free IG model in WWIII by the following set of equations:

$$Depth_{IG} = \frac{H_s}{\gamma_{lib}} \tag{5.7}$$

$$E_{forced}(f) = \int_{\Delta f}^{\infty} df \int_{0}^{2\pi} d\theta_1 \int_{0}^{2\pi} d\theta_2 \, D^2(f + \Delta f, f, \Delta\theta, Depth_{IG}) E(f + \Delta f, \theta_1) E(f, \theta_2) \tag{5.8}$$

$$\beta_H(f) = \frac{h_x}{2\pi f}\sqrt{\frac{g}{H}} \tag{5.9}$$

$$R(f) = min(\, 0.1\pi\beta_H^2 \,, 1) \tag{5.10}$$

$$E_{free}(f, \theta) = R^2 \, . E_{forced}(f, \theta) \tag{5.11}$$

The reflection coefficient R has been defined for wave heights, and must therefore be squared when applied to wave energies. The angular dependency can optionally be removed if the angular spread of the free IG is assumed to be large. This might be the case for coarse spatial resolutions. We can then expect an isotropic spectrum. The outgoing IG energy would then be

$$E_{free}(f, \theta) = R^2 \, . E_{forced}(f)/2\pi \tag{5.12}$$

Similarly to the empirical approach, this computed outgoing free IG energy is then introduced as a source term in the reflection algorithm in WWIII. It should be noted here that contrary to the empirical source of IG free waves, the IG waves are not completely absorbed at the shoreline but rather added to the outgoing spectrum after going through the reflection coefficients. This appears to be a more realistic approach.

This parametrization was then implemented and calibrated using the Duck94 observations and configuration as described in the next section. For this parametrization, two main parameters need to be calibrated, namely the liberation depth, $Depth_{IG}$ which will affect the overall IG level and the bottom slope, which is not always known but which will affect the shape of the IG spectra

5.4 Testing and Calibration on the shelf: Duck94 campaign

In order to calibrate and validate the methodology for free IG levels from the incoming spectra using the 2nd order coupling coefficients, we will use observations recorded during the Duck94 campaign.

5.4.1 Model setup

We implemented a uniform grid on a regional scale in WWIII, enclosing the whole shelf up to 3000m. The grid resolution was 1 minute in both directions. The bathymetry used is shown in Figure 5.2. The model was forced by NCEP winds over the domain and by spectral outputs from global 0.5 degree runs interpolated over the seaward boundary. Similarly to Ardhuin et al. (2014), we make sure that the first wet nodes have a depth of at least 3 m.

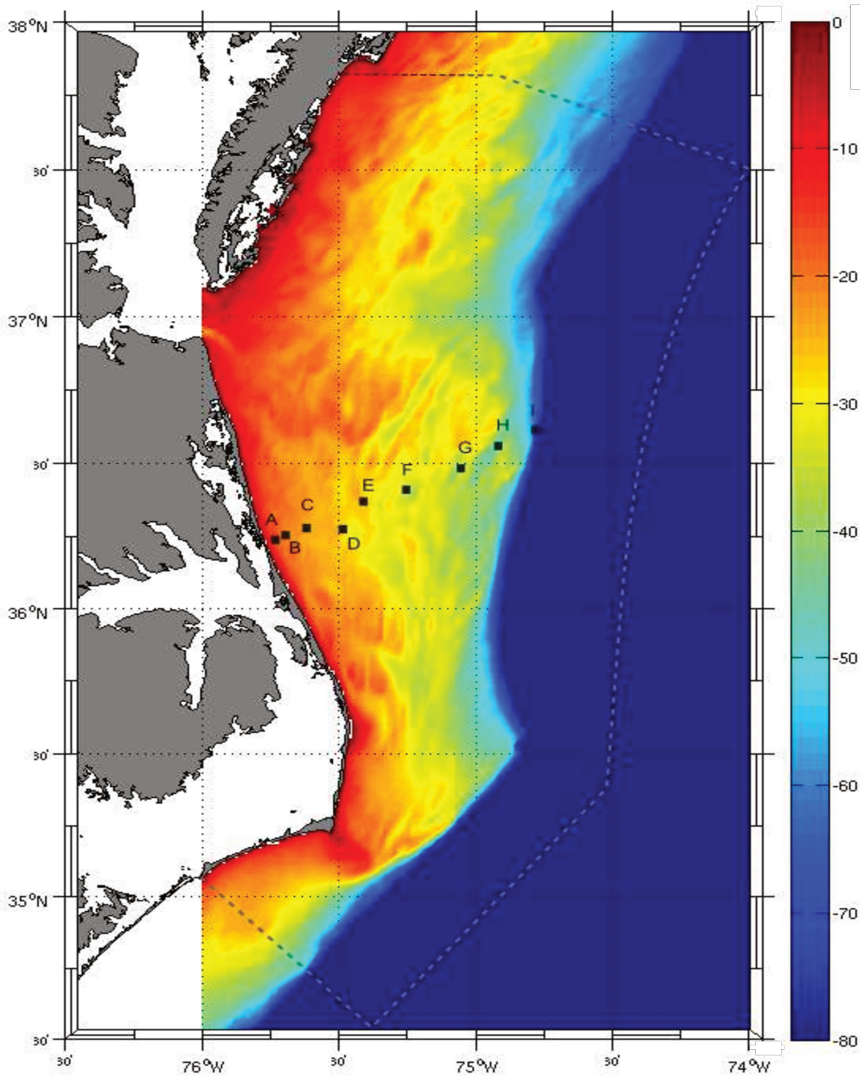

Figure 5.2: Location map of pressure sensors and bathymetry used for the Duck94 model setup. The grey dashed line show the limits of the computational domain.

Below are presented the overall results for the computed IG wave heights and the total wave heights, averaged over the whole period. The spectral results are also extracted at the location of the pressure sensors.

5.4.2 Model calibration and results

For this parametrization, the model has to be calibrated for the liberation depth, $Depth_{IG}$ and the bottom slope. Varying the liberation depth changes the overall IG level without affecting much the shape of the IG spectra. A liberation depth corresponding to a γ_{lib} of 0.8 was used here. The bottom slope mostly changes the shape of the IG spectra. We adjusted the slope so that the f^{-4} cut-off of the bound IG coincides with the maxima of the average IG spectra measured. Various amounts of background IG were taken into account for the calibration and the bound IG was removed from the observed spectra. The comparison between the average observed and calibrated modelled spectra at different locations is shown in

Figure 5.3.

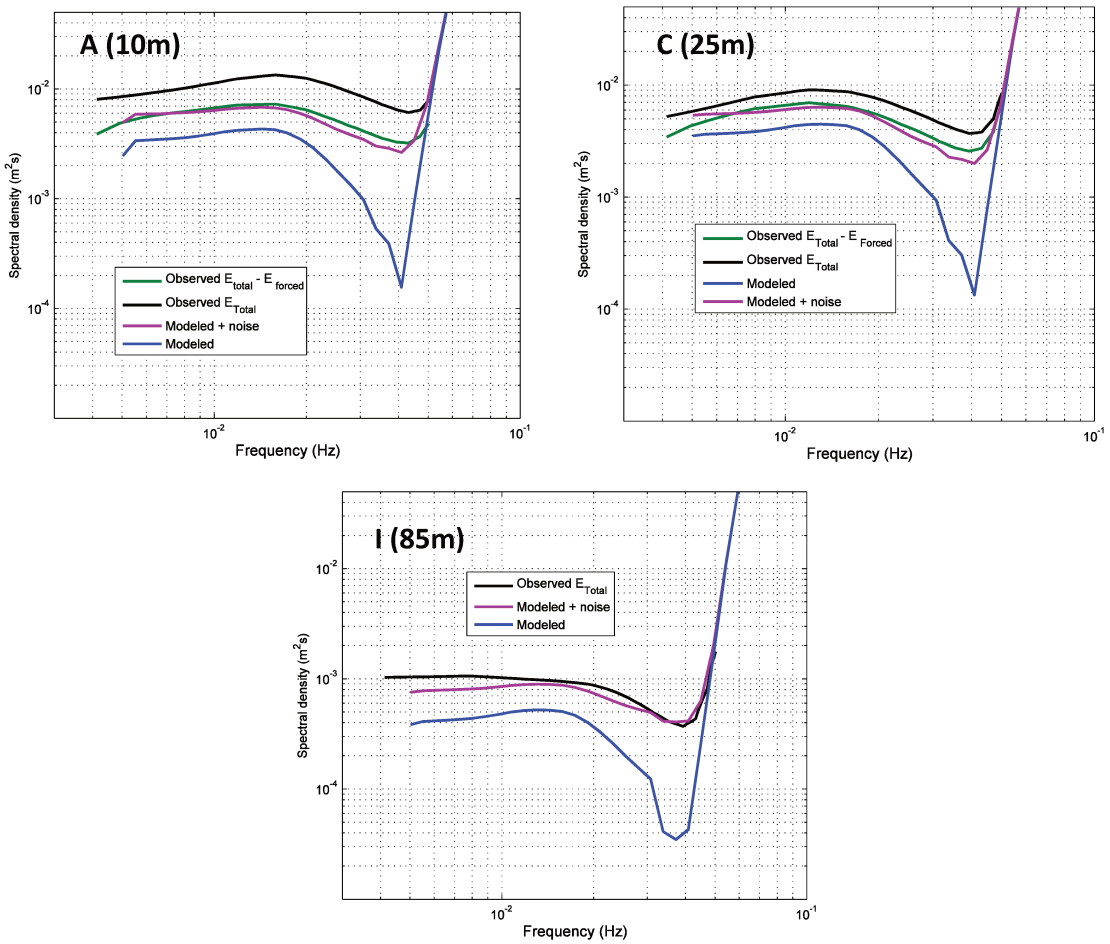

Figure 5.3 Average observed (black) and modeled spectra (blue) at locations A (top left), C (top right) and I (bottom). The green curves show the average observed spectra subtracted of the average bound IG estimation and the magenta curve shows the average modeled spectra with a white background IG added.

The average bound IG was subtracted from the average observed spectra at each depth. These were then made to coincide with the modeled spectra complemented with a

certain amount of white background IG.

5.4.3 Results

It took less than 24 hours of model run to complete the 4 months of simulation, including 5 days of spin up, on a 64 nodes cluster. The average significant wave heights and significant IG wave heights (integrated from 0.005 Hz to 0.04Hz) averaged over the simulation period are shown below.

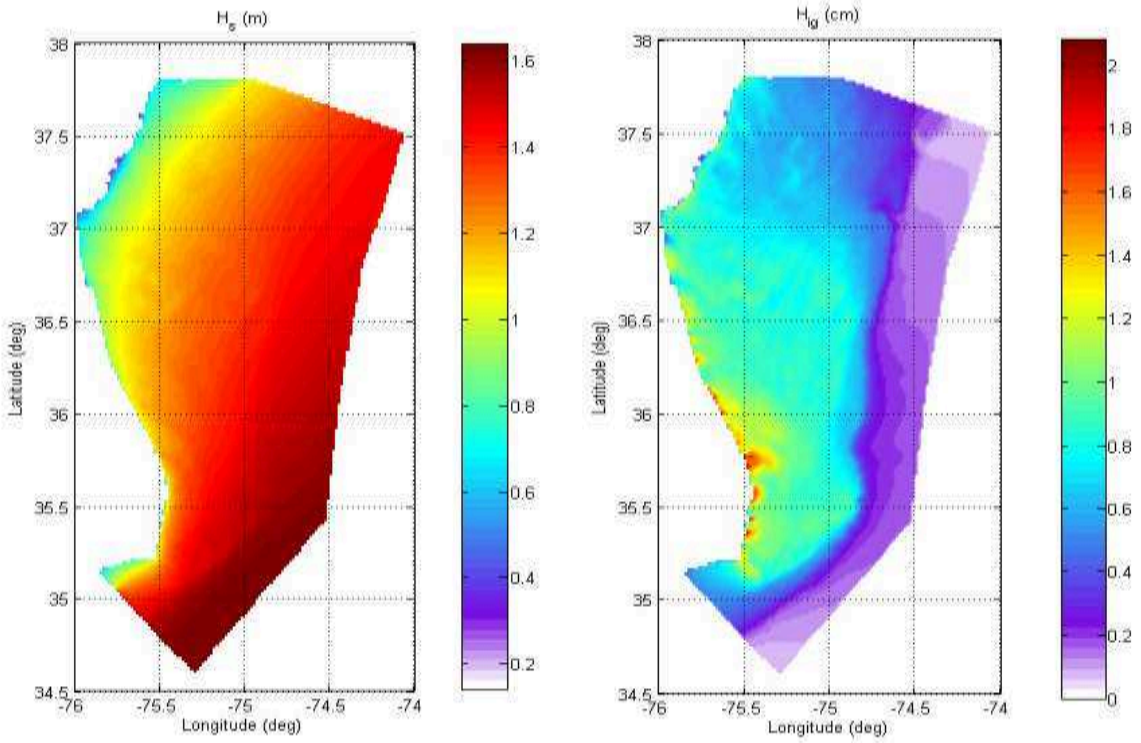

Figure 5.4 Modeled Hs field (left) and IG wave field (right) averaged over the period of simulation.

The IG levels are in general highest on the shelf and decrease towards deeper waters, as expected. Near the coastline, the IG levels are highest when there is direct impact of incoming sea and swell.

The time series of the measured and modelled HIG, integrated over the frequency range of 0.005Hz to 0.04Hz are shown in Figure 5.5. Over these frequencies the modelled infra-gravity wave height was defined as,

$$H_{IG} = 4\sqrt{\int_{f_{min}}^{f_{max}} E(f) + E_N df} \tag{5.13}$$

where E_N is a background IG level (assumed constant over time) that has been added to the modelled IG (green curves) for comparison. The background IG level was estimated in such a way to correspond to the lowest H_{IG} level measured each location throughout the period.

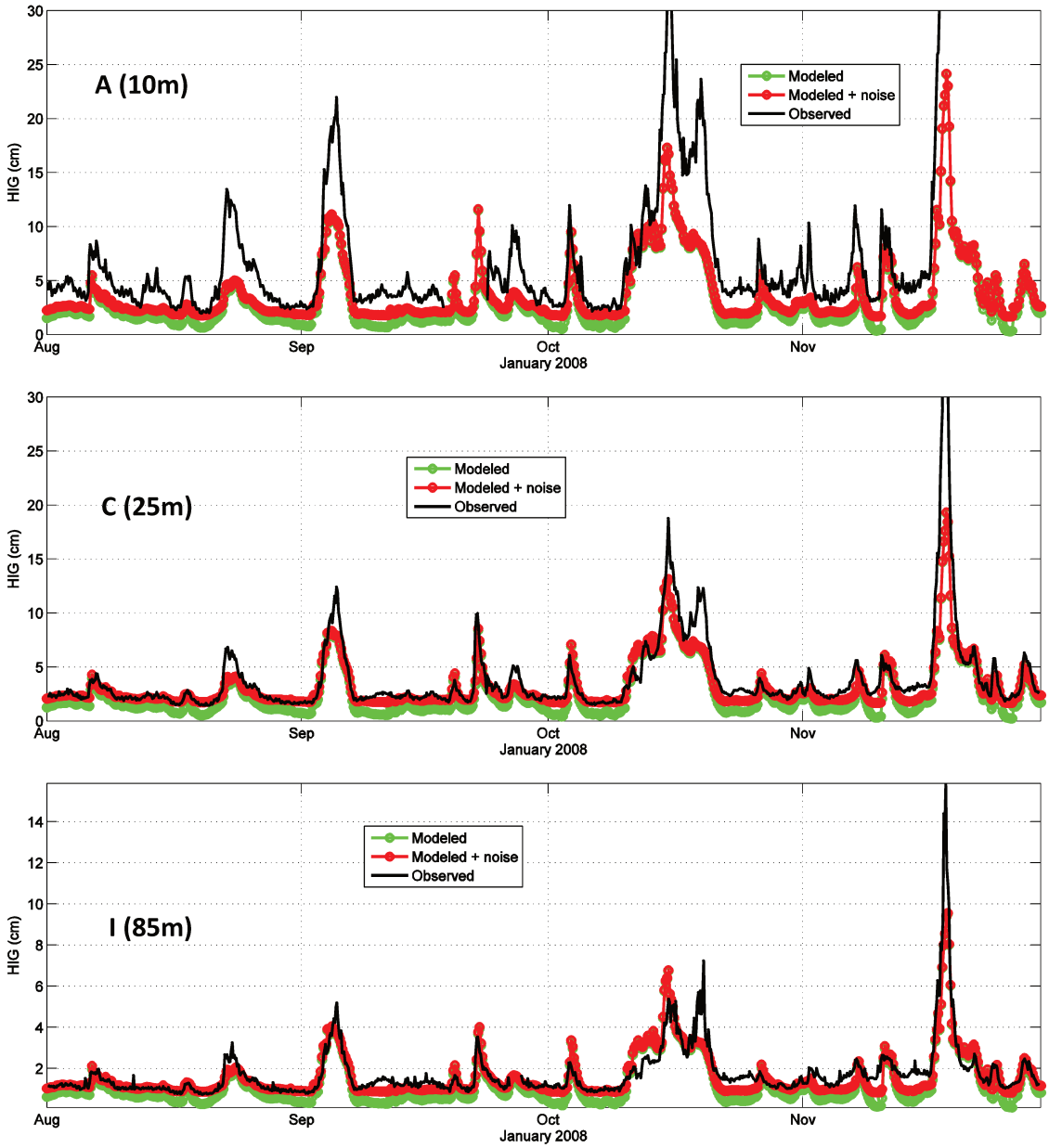

Figure 5.5 Measured (black curves), modeled (green curves) and modeled HIG with noise (red curves) integrated in the frequency range of 0.005Hz to 0.04Hz (top) at location A (top), C (middle) and I (bottom).

Keeping in mind the possible errors in the winds used as forcing, the free IG levels seem to be fairly estimated by the model, especially in deeper waters. The discrepancies between observations and model results for the peak events are highest for shallower depths (at location A), probably due to bound-IG waves. Bound IG hence seems to contaminate the observations particularly for peak events. The noisiness of the bound IG time series did not allow its filtering from the times-series of the observed signal. The noise (background IG) level seems to be slightly dependent on the water depth as well. This could indicate the possible role of non-linear effects (besides bound IG) on the

noise level. It should be noted that the addition of a little white noise does not influence the peaks very much. It only increases the IG level during 'calm' periods.

5.4.4 Comparison with empirical formulation

In Figure 5.6 and Figure 5.7 we compare runs made with both the empirical and the 2nd order formulations.

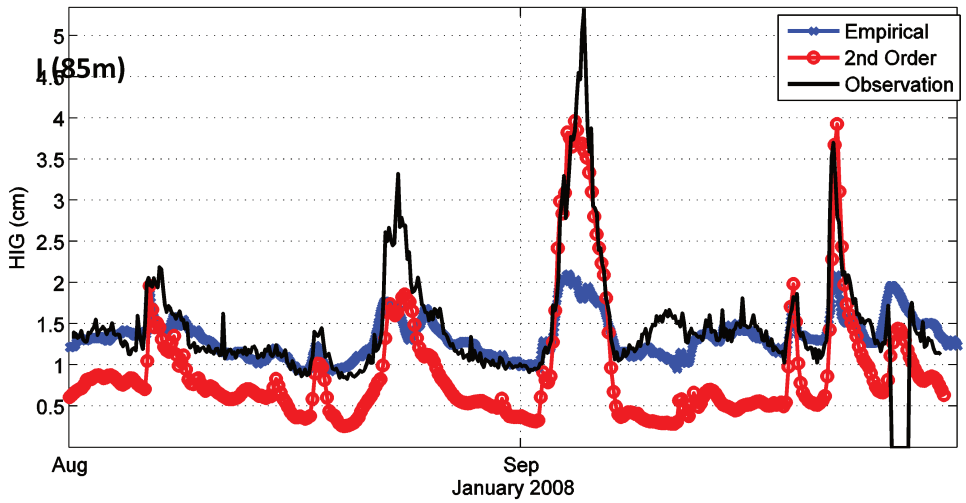

Figure 5.6 Measured (black curve) and modeled H_{IG} integrated in the frequency range of 0.005Hz to 0.04Hz at station I (85m). Blue stars shows model results from the empirical approach and red circles shows results from the 2nd order approach.

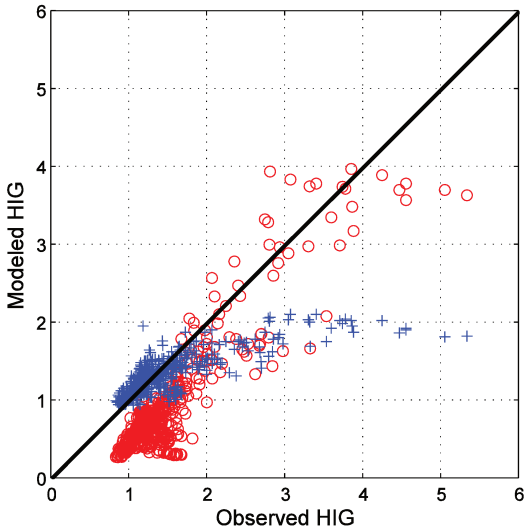

Figure 5.7 Correlation between measured and modeled H_{IG} (in cm)integrated in the frequency range of 0.005Hz to 0.04Hz at station I (85m). Blue crosses shows model results from the empirical approach and red circles shows results from the 2nd order approach.

We can observe that neither of the formulation works perfectly for the whole range of IG levels. The empirical approach has a better representation for lower IG levels (including

the previously described background IG) while underestimating peak IG levels. On the other hand, the 2nd order approach shows better correlation for higher IG values while underestimating lower values for IG.

5.4.5 Discussion

Both the empirical and the 2nd order formulation appear to correctly estimate the free IG levels in general but each formulation appears to work better for either high or low IG levels. There seem to be a certain complementarity between these two approaches which will be discussed later.

In the case of Duck, the comparison with observations is quite difficult due to the contamination with bound IG waves, especially for shallower waters (<30m). Also the wind fields for this period (more than 20 years back) are not very reliable, both for the global nesting run and the local forcing. We shall therefore use another more recent dataset from another region to improve the calibration and the testing the model.

5.5 Calibration and testing on unstructured grids with observation in Intermediate Depths

In this section we are going to implement and test the same free IG parameterization based on bound IG liberation but with unstructured grids. The validation will this time be carried out in intermediate water depths on a large regional archipelagic configuration: the Hawaiian Islands.

5.5.1 Model setup

An unstructured triangular grid was constructed on a regional scale, enclosing the whole Hawaiian archipelago up to the abyssal plain. The grid structure was generated and optimized using Polymesh (TU Darmstadt) by Ardhuin and Roland (2012), based on bathymetry assembled by the Hawaii Mapping Research Group.

The grid resolution was about ¼° near the outer boundary and 200m near the coast. The bathymetry and grid used are shown in Figure 5.8 below. The grid contains about 10000 nodes.

The model was forced by 2012 ECMWF winds over the domain and spectral outputs from the global 0.5 degree runs (also forced by 2012 ECMWF winds) interpolated over the whole boundary. Here also, in line with Ardhuin et al. (2014) we make sure that the water depths do not become less than 4 m, and introduce the IG wave as source terms at the first wet nodes neighbouring the land nodes. The specific numeric definition for the running of WWIII with unstructured grids is presented in Ardhuin and Roland, (2012).

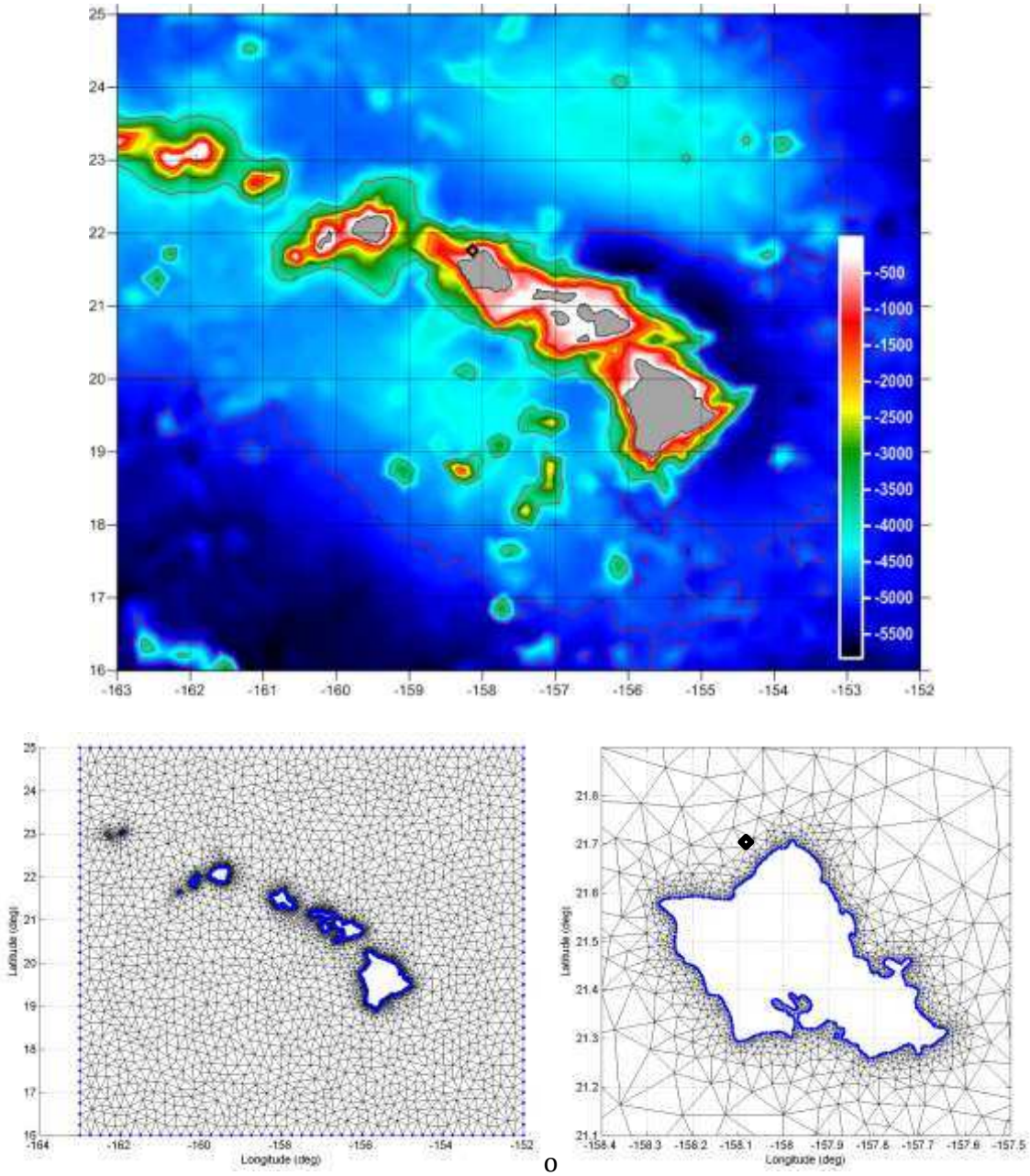

Figure 5.8: Bathymetry used for the Hawaii model setup (Top). Location of the pressure sensor deployment is indicated by a black diamond. The bottom left figure shows the mesh used over the region with a zoom on Oahu on the right.

5.5.2 Model results and comparison

It took less than 24 hours of model run to complete the 105 days of simulation on a 64 node cluster. The results are displayed and analysed below.

5.5.2.1 Average Hs and HIG fields

The average total significant wave heights and significant wave heights in the IG domain (0.005 Hz to 0.04Hz) are shown below.

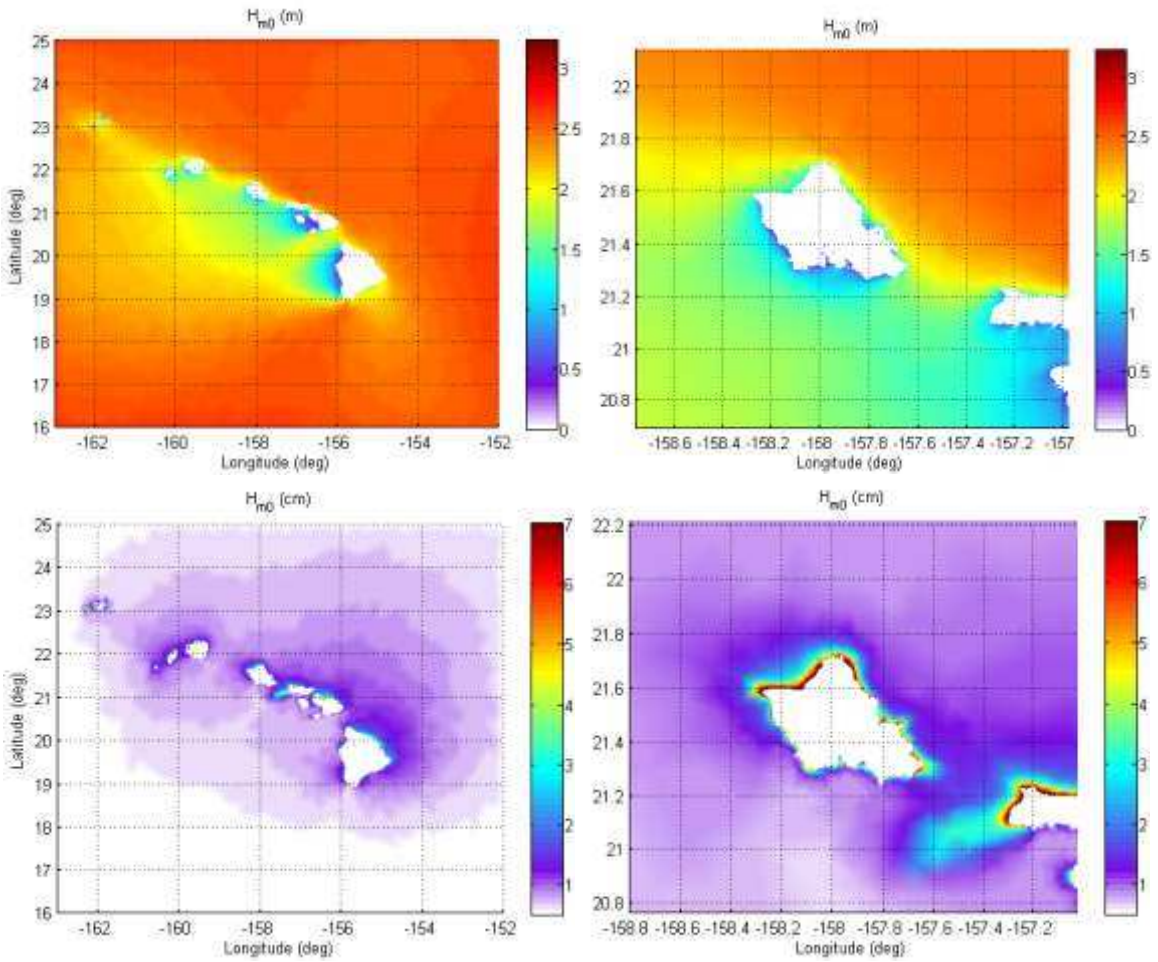

Figure 5.9 Modeled average Hs field (top) and IG wave field (bottom) with a zoom on Oahu Island (right) .

As expected, the IG levels are generally highest near the coastline and in regions of shallow bathymetry and decrease away from the shoreline towards deeper waters. This is characteristic of linear de-shoaling and the inverse square law due to the lateral spreading of the IG wave fronts far away from the islands. This decrease of the IG wave field corresponds to the conservation of the energy flux away from a localized source. The mean nearshore IG levels for example decay from about 12 cm in 4 m depth to less than 1 cm in 4000 m depth.

5.5.2.2 Time series and correlation with observations

The time series of the measured and modelled total Hs and H_{IG}, are shown in Figure 5.10.

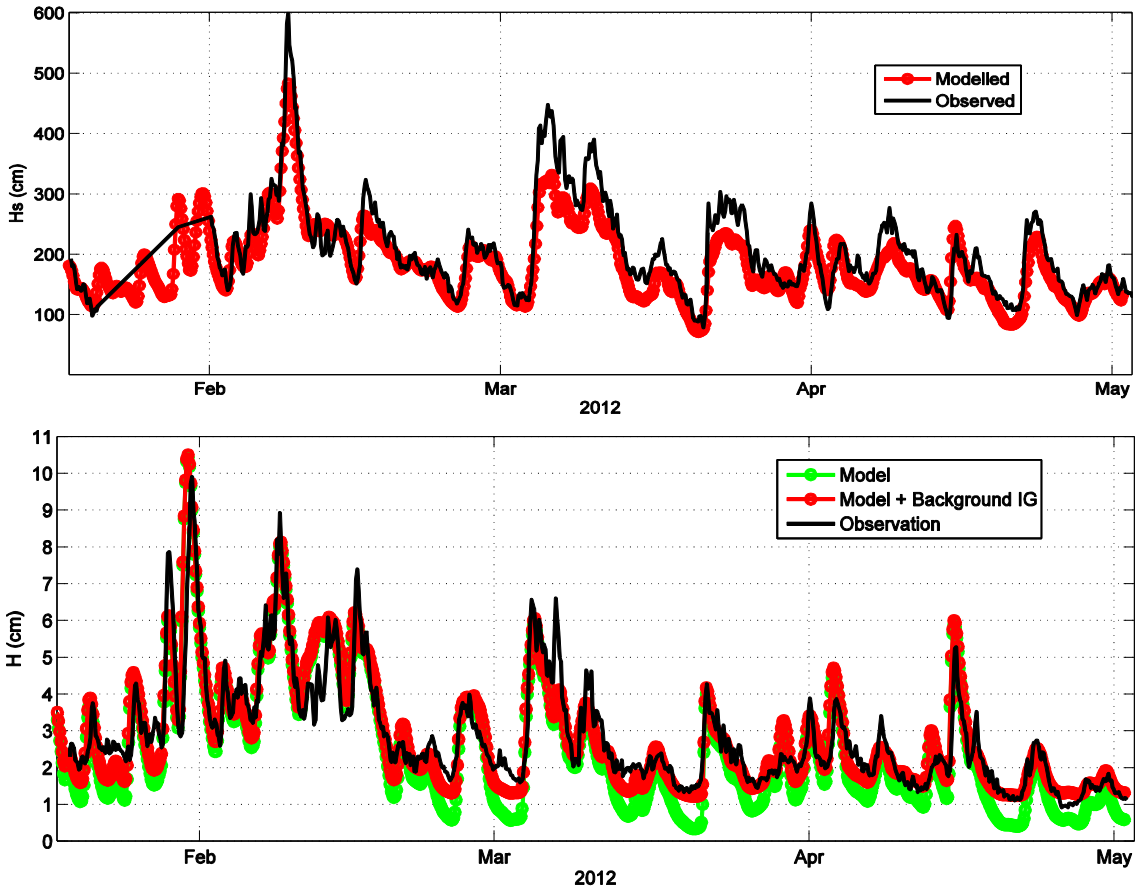

Figure 5.10 Measured and modeled total Hs integrated in the frequency range of 0.025Hz to 0.58Hz (top) and HIG, integrated in the frequency range of 0.005Hz to 0.04Hz (bottom). The green curve shows the modelled HIG without any addedbackground IG.

Short wave parameters are well estimated by the wave model, with typical errors on Hs of the order of 10%, similar that noted in Ardhuin et al. (2014).

5.5.2.3 Spectral comparison

Figure 5.11 compares spectra of the average observed and modelled IG energy

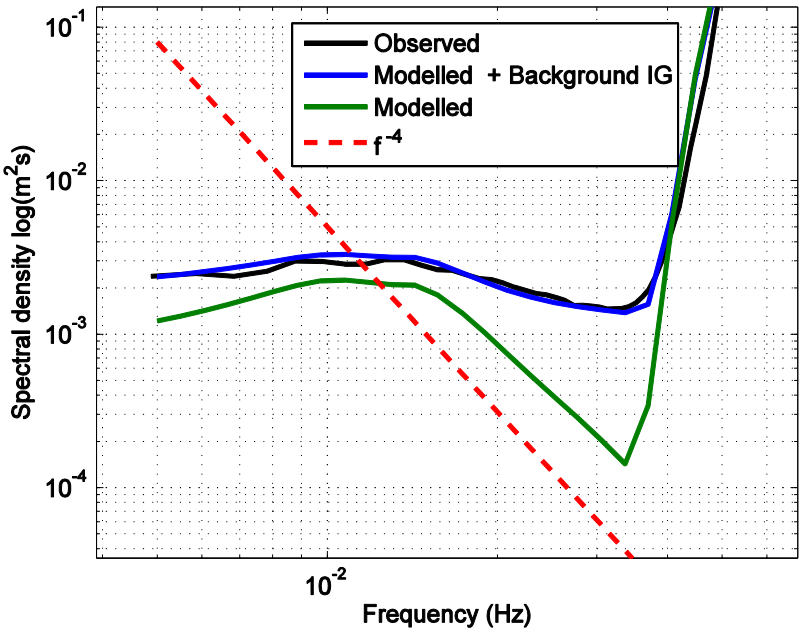

Figure 5.11 Average observed (black), modeled spectra (green) and modelled spectra with a little white background IG added (blue).

In this case, less white background IG has to be added in order for the spectra to corroborate. Both the IG levels and spectral shape then match almost perfectly.

5.5.3 Discussion

Since the estimated level of bound IG is very low, and from the reasoning in the previous paragraph, we can deduce that the small discrepancy between the observed and modelled average spectral shape is indeed due to a certain background IG level with a flatter spectral shape. Compared to the Duck94 configuration, here the amount of background IG needed to match the observed IG is much lower, suggesting a depth dependence of this background IG.

The presence of this background IG level has a tendency to flatten the IG frequency distribution and mask the shape of the locally liberation-generated IG wave spectra. The spectral shape of this background IG was assumed to be flat, but this might not necessarily be the case.

Similarly to Ardhuin et al, the model was calibrated using different regional configurations, including Duck and Hawaii. These two configurations are quite different, one being a large shelf and the other being a steeper volcanic configuration. Both these configuration would however have the inconvenience of having background IG in the field observations. In this sense, the empirical method would have the advantage of having this background IG included in the calibration, hence probably explaining the better correlation for lower IG levels. Using the second order method, this IG noise has to be accounted for in order to obtain a better correlation.

Also as noted from the Duck modelling, there seem to be a certain complementarity between these two approaches. It is also possible that this is linked to different complementary underlying generation mechanisms.

In the next section we are going to verify the 2nd order approach using additional observations from the open sea and hence validate the model on the global scale.

5.6 Setting up global model

Having calibrated the parameterization of free IG sources, notably across a wide continental shelf and around an island, we can now setup and test the model on a global scale where the model will be validated using observations from historical tsunameter and other BPR as well as from seafloor mounted hydrophones.

Due to limitations in computing power and the availability of an existing fine-tuned global configuration, we are going to setup a global 0.5° structured grid, similar to the one used for operational global wave modeling within Previmer (Lecornu and De Roeck, 2009). However, there are several aspects that need to be taken into consideration for the setting up of IG waves in a global 0.5° model.

- Accounting for sudden depth changes

The parameterized IG source will be put in the numerical 0.5° wave model at all points adjacent to the land. There the depth may have any value, especially for regions with steep slopes or narrow shelves. It is for example possible to jump from land to the deep sea floor in less than 0.5°. We thus have to adjust the outgoing IG energy level to reproduce the expected shoaling of a broad directional wave spectrum, using a factor k/C_g

$$E_{first\ wet\ node}(f) = E_{free}(f)\frac{k}{C_g} \tag{5.14}$$

5.6.1 Model results and comparison

The global runs are more computationally expensive. Only 60 days of simulation can be carried out in 24 hours of model run on a 64 node cluster, including 10 days of spin up. The average significant wave heights in the IG domain (0.005 Hz to 0.04Hz) are shown below for the months of January and February 2008 and for the months of July and August 2008, attempting to represent typical winter scenarios in the northern and southern hemispheres.

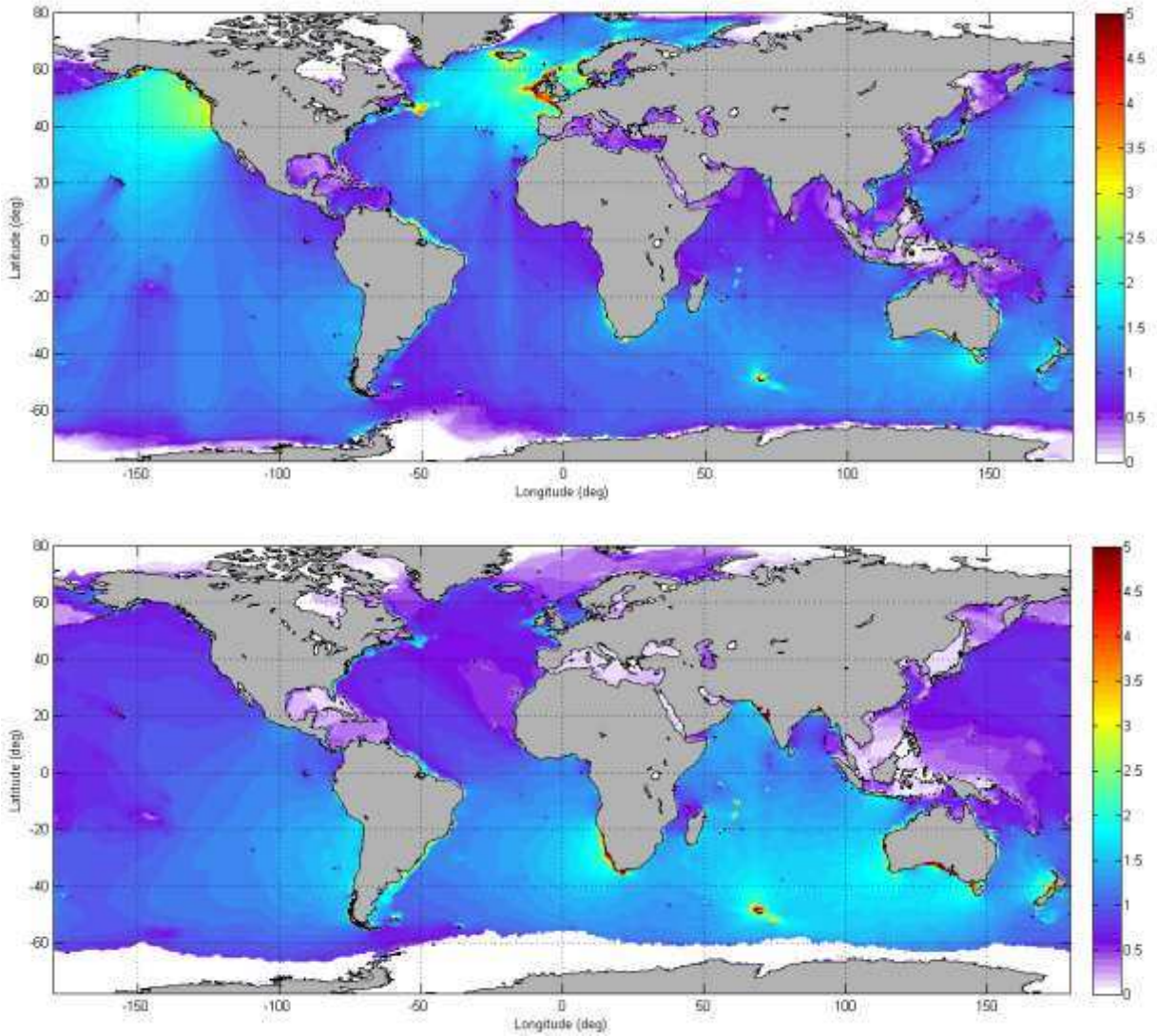

Figure 5.12 Modeled average IG wave field for the months of January and February 2008 (top) and for the months of July and August 2008 (bottom), integrated in the frequency range 0.005 Hz to 0.04 Hz.

Figure 5.13 and Figure 5.14 show the time series of the measured and modelled H_{IG} for a few DART stations in early 2008, integrated over the frequency range of 0.005Hz to 0.010Hz

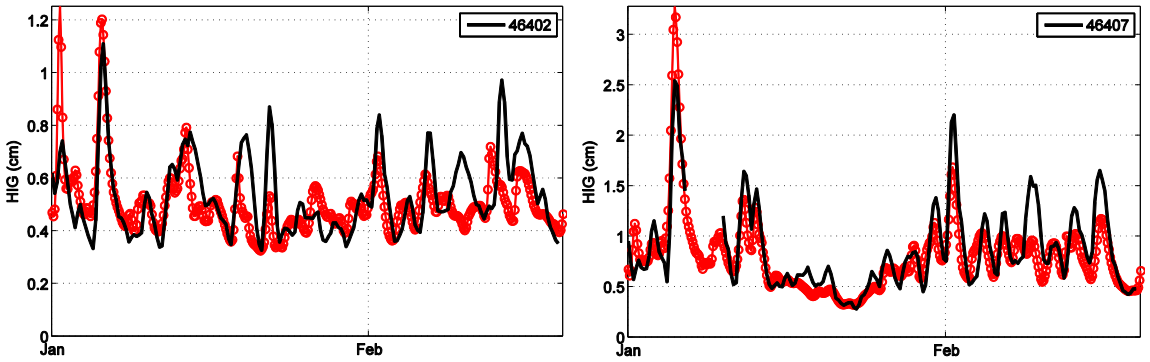

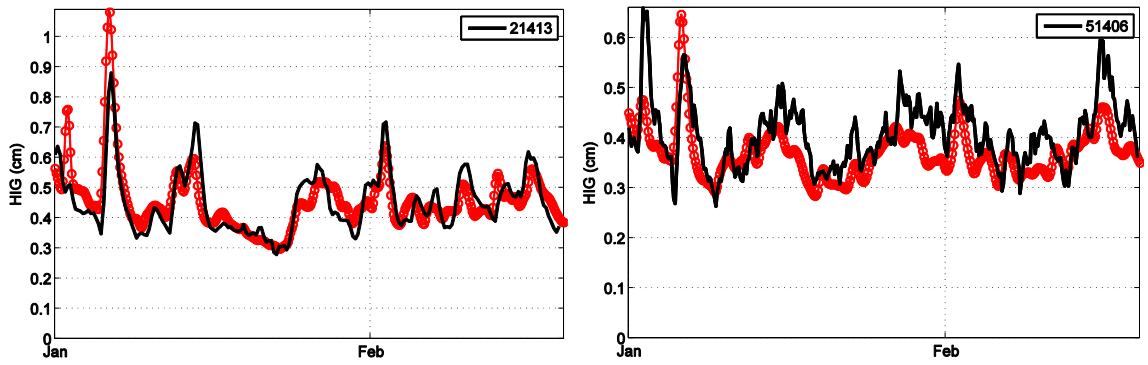

Figure 5.13 Time series of measured (black curves) and modeled (red circles) HIG, integrated in the frequency range 0.005Hz to 0.010Hz at selected DART locations in the North Pacific Ocean.

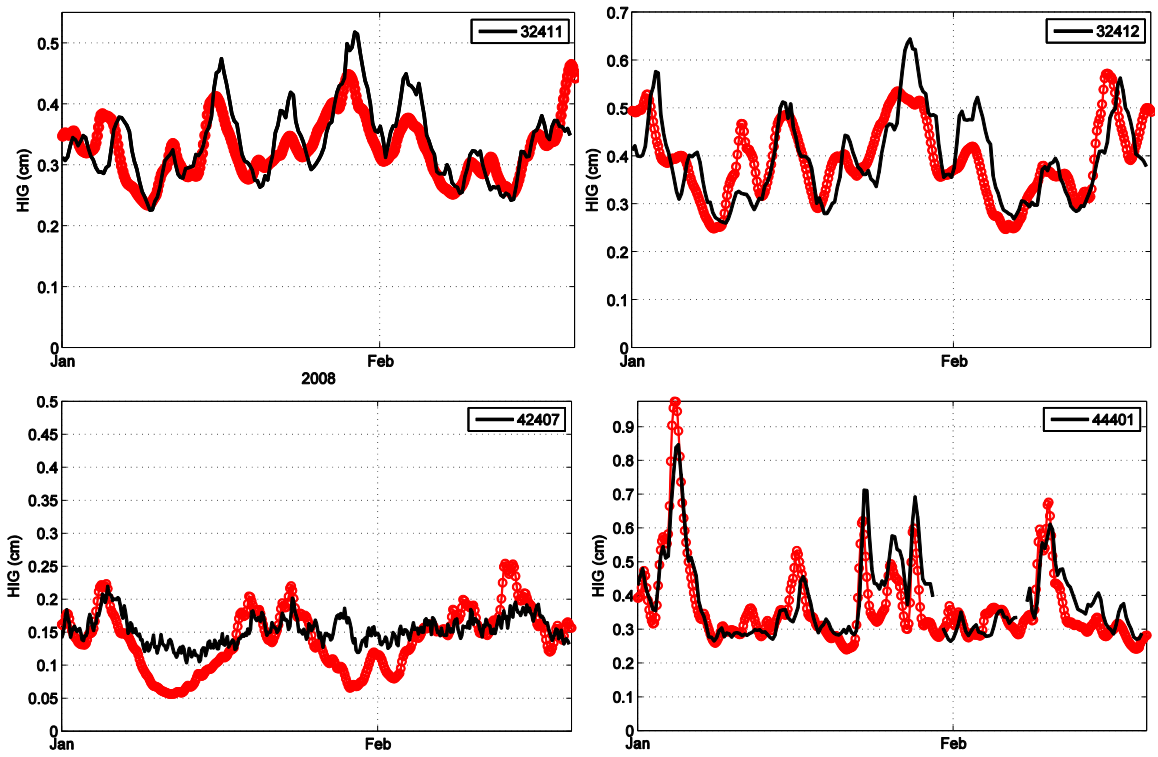

Figure 5.14 Time series of measured (black curves)and modeled (red circles) HIG, integrated in the frequency range 0.005Hz to 0.010Hz at selected DART locations in the south Pacific (32411 and 32412) and North Atlantic Ocean (44401 and 42407).

Estimates are good for most of the DART locations except for station 42407 in the Gulf of Mexico and station 51407 near Hawaii (not shown). These 2 locations seem to have particular characteristics which could explain these discrepancies. It should be noted that a globally constant background IG energy level was added to the model outputs explaining the good match with the observation. However it can be also observed that the highest IG peaks are being sometimes overestimated.

Station 42407 in the Caribbean Sea is found in a semi enclosed basin, between Puerto

Rico and continental Central America. This semi enclosed basin could give rise to multiple internal reflections of IG waves without distance attenuation, which would result in a higher level of 'ambient' IG energy. This could explain the relatively high background IG signal with only higher IG peaks piercing through.

The time series of the measured and modelled HIG for OBS station OBS-21 in the gulf of Cadiz and for BPR station JPP2 on the Mid-Atlantic ridge is shown in Figure 5.15

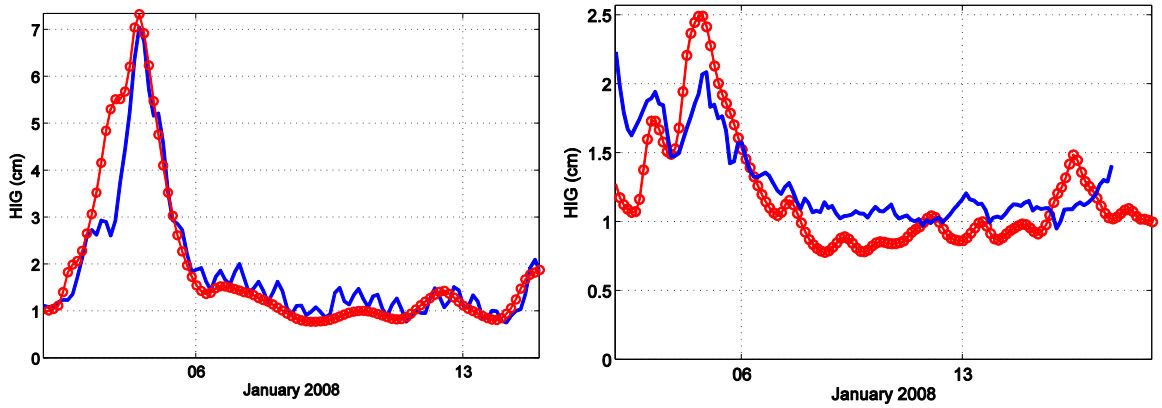

Figure 5.15 Measured (blue curve) and modeled (red circles) HIG for station OBS-21 in the gulf of Cadiz (left) and for station JPP2 on the Mid-Atlantic ridge (right), integrated in the frequency range 0.005Hz to 0.015Hz. The effect of tide cycles can be seen in the observations for station OBS-21.

5.6.2 Effect of slope and frequency dependence

As suggested in the previous chapter, the normalised bed slope has a certain influence of on the IG level, especially on the spectral shape. In the case of a small domain, such as the North Carolina configuration, the bed slope can be assumed to be constant. However on the global scale, where several bed slope type exist (beaches, cliffs and estuaries) with different gradients, a sufficiently accurate gradient map should be used.

This was done with the global runs, but accurate bed slope was available only in some very limited regions, such as the North American coasts. The slopes for the remaining regions of the world, including islands were approximated using ETOPO2, 2-minutes global bathymetry.

However this slope approximation was not very good and turned out to have a negative impact on the modelling results. Hence a constant bottom slope of 10% was used for all the coasts which improved the results. This could be improved in the future whenever better values for global coastal slopes become available.

5.6.3 Effect of sub-grid shelves

Tucker (1950) observed long waves approximately 800 m offshore and found that these waves lagged the incident wave groups by approximately 5 minutes. This lag was about the time required for the forced wave to reach shore and an associated free wave to travel back.

If we consider a shelf of 100m depth, the phase velocity of 12s period waves is around 9m/s, which is equivalent to travelling 55km (0.5° at the equator) in 1h40. The group velocity is about half the phase velocity for *kD>>1*. This travel time from the beginning of the node to the land could hence be more than three hours. If we take into account the time for free IG waves to travel back (shallow water approximation) we can have a lag of up to 6 hours.

Hence the proper resolvability of narrow shelves has to be taken into consideration while setting up a global model. With the current set up, shelves having a width less than 0.5° will not be properly resolved, which would lead to a certain time lag in the offshore peak signal for example. Figure 5.16 below shows IG levels corresponding to an IG burst occurring around the 18th of July 2008 off the coast of Chile in the Eastern Pacific Ocean (cf chapter 5).

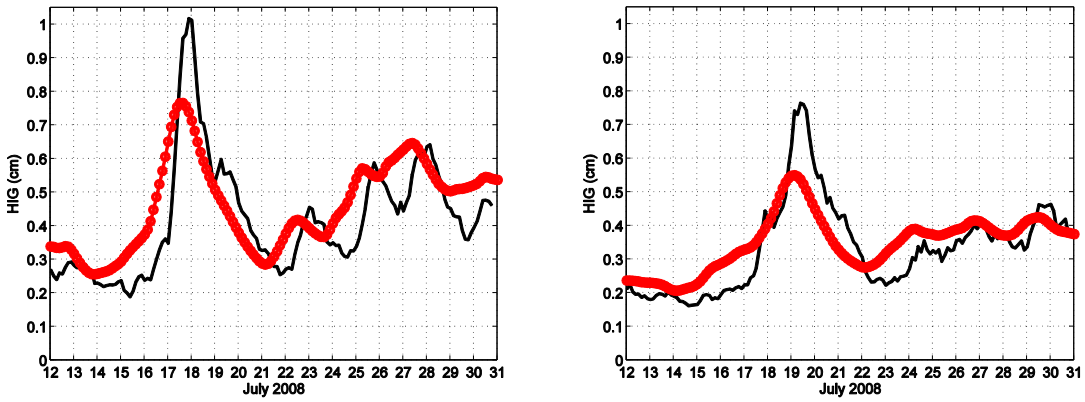

Figure 5.16 IG levels observed (black curves) and modeled (red circles) at DART stations 32412 (left) and 32411 (right) corresponding to an IG burst occurring around the 18th of July 2008 off the coast of Chile.

It can be observed that the modeled peaks in the signals are leading the measured signals by a few hours. It is known that the width of the continental shelf along this portion of the coastline is not very wide (< 30 km) and can be completely absent in the 0.5° grid. So a certain factor could be used that will be proportional to the width of the shelves adjacent to the coastlines and the corresponding depths, and which could be used to artificially correct for this issue. In order to resolve this problem, the best way would be to increase the resolution of the global grid, or use a nesting methodology that better resolves the coastline and shelves at desired locations.

5.7 Discussion and conclusion

We have been able set up a parameterization of free IG generation by the liberation of bound IG waves. These were computed from the incident short waves spectra using 2nd order coupling coefficients. The method was tested and calibrated with correct results along two typical coastlines namely the continental shelf off Duck, in Northern Carolina and around the Hawaiian Islands. Observations from these regions seem to at least partly confirm the generation of free IG from the bound IG generated from the short waves and modulated by a reflection coefficient derived from the normalized bed slope and hence dependent on f^{-4}. This effect of reflection modulation was established in the previous chapters from the investigations with XBeach. However the growth of bound IG, which is also dependent on the normalized bed slope, was not integrated in the parametrization.

The presence of a certain background IG level was noted. It has a tendency to flatten the IG frequency distribution and mask the f^{-4} dependencies in the liberation-generated IG wave spectra. When this IG noise was accounted for by a constant white IG level, better correlation of the results with field measurements was obtained. However this need not be done with the empirical approach.

In general, the empirical approach has a better representation for lower IG levels while underestimating peak IG levels. On the other hand, the 2nd order approach shows better correlation for higher IG values while underestimating lower values for IG. It can be inferred that there is certain complementarity between these two approaches, probably linked to different but complementary underlying generation mechanisms. Since for the empirical approach there is a linear dependency of H_{IG} with the short wave height H_s, it can be linked to the varying-breakpoint generation mechanism of Symonds et al. (1982), hence explaining better result correlation for lower IG levels (including the previously discussed background IG level). The 2nd order approach has a quadratic dependency of H_{IG} with H_s (Longuet-Higgins and Stewart, 1964), which explains the better correlation for higher IG levels but underestimating lower IG levels. Hence this might give the impression of having an unaccounted background IG level.

In the deep sea and where data was available, the modelled IG levels is consistent with analysed records from Deep-ocean Assessment and Reporting of Tsunamis (DART) systems (Aucan and Ardhuin, 2013) as well as records from other measurement systems including hydrophones on the seafloor. Some issues were highlighted, including the possible effect of sub-grid shelves on the time lag of IG waves and the effects of bed slope. However the true effect of the bed slope could not be properly studied on the global scale due to the absence of proper estimates of these slopes globally.

In the next chapter we are going to use both the empirical and the second order method to study specific IG events on the global scale, including their generation and propagation across whole ocean basins.

6 Global IG waves events

The objective of the present chapter is to investigate the generation and the propagation from coast to coast of high energy free IG wave events. The seasonal average IGW fields have already been investigated by using in-situ data (Aucan and Ardhuin (2013) and numerical simulations (Ardhuin et al., 2014). Here, our focus on the strongest IGW events is motivated by several applications in which these events are important: this is the case for the question of precise satellite altimetry measurements or the breaking of ice tongues off Antarctica (Bromirski et al., 2010). For example for the upcoming Surface Water & Ocean Topography (SWOT) mission, the determination of the strongest 'noise' in sea level measurement coming from IG waves will be crucial, especially during these major IG bursts.

A detailed comparison between predictions and observations are made over ~10 day periods corresponding to a major storm in the north Pacific, another major storm in the Atlantic and a third one in the south Pacific. The model and data analysis method is briefly reviewed in section 2, followed by a detailed analysis of the three IG events in section 3, a thorough discussion in section 4, and a conclusion in section 5. A large portion of this chapter, mostly the first two events was published in Rawat et al. (2014).

6.1 Methods: Numerical model and data processing

6.1.1 Model

The numerical model for infragravity waves represents the spectral evolution of the free IG waves by a simple extension to low frequencies of the usual spectral wave models used for wind seas and swell. A source of IG wave energy is parameterized from the shorter wave components at all grid points adjacent to land. All these aspects are described in details by Ardhuin et al. (2014), and are included in the version 4.18 of the WAVEWATCH III modeling framework (Tolman et al., 2014). The important aspect of this model is the source of IG free waves, which was inferred empirically from coastal measurements in Hawaii, North Carolina and France. Based on these datasets, the IG wave height H_{IG} radiated from the shoreline was set to

$$H_{IG} \approx \alpha_1 H_s T_{m0,-2}^2 \sqrt{\frac{g}{D}} \tag{6.1}$$

where H_s is the significant wave height of wind seas and swells, $T_{m0,-2}$ is the mean period given by the -2 and 0 moments of the surface elevation spectrum, g is the apparent acceleration of gravity, D is the local mean water depth, and α_1 is a dimensional constant.

.

The validation of this model was shown for a few locations in Ardhuin et al. (2014).

An alternative IG model described in chapter 4 and based on the liberation of bound IG waves in the surf zone and their subsequent reflection on the beach was also used for some of the runs.

Both models showed similar results and can be used interchangeably. The same settings are used, with a spatial resolution of 0.5 degree in latitude and longitude, a model spectral band that ranges from 0.005 Hz to 0.72 Hz, and a forcing that includes ECMWF operational wind analyses, NCEP sea ice concentrations, and small iceberg concentrations for the southern ocean from Ifremer/CERSAT which reduce the wave energy flux (Ardhuin et al., 2011).

6.1.2 Observations

We use bottom pressure records from a few stations, including permanent Deep-ocean Assessment and Reporting of Tsunamis (DART) stations, the pressure time series from the MOMAR (Monitoring of the Mid-Atlantic Ridge) Observatory (Ballu et al., 2006, 2009), and the NEAREST campaign off the continental margin of Portugal (Harris et al., 2013), including broad-band hydrophones HTI-01-PCA/ULF digitized and logged in Geolon MCS recorders. Ocean bottom pressure records are transformed into infragravity wave elevation parameters by computing Fourier transform over 30-minute overlapping windows averaged every three hours.

After correcting for the instrument response, the bottom power pressure spectrum $F_p(f)$ was converted to a surface elevation spectrum $E(f)$, assuming that all the recorded signal corresponds to (free) linear surface gravity waves as in Aucan and Ardhuin (2013),

$$E(f) = F_p(f)\left(\frac{cosh(kD)}{\rho g}\right)^2 \tag{6.2}$$

This transformation is appropriate if the linear wave signal dominates, and if it is above the instrument noise floor. These constraints limit the validity of eq. (6.2) to a finite range of frequencies between f_{min} and f_{max}. To avoid other types of motions we chose f_{min} = 5 mHz and to be able to compare data from all water depths, up to 5800 m, we set f_{max} = 10 mHz. Over these frequencies we define an infra-gravity wave height, by analogy with the usual significant wave height,

$$H_{IG} = 4\sqrt{\int_{f_{min}}^{f_{max}} E(f) - E_N df} \tag{6.3}$$

where E_N is a noise floor that was adjusted to the median of the spectral density at 15 mHz for each measurement location. We also estimated this height from the modeled spectra $E(f)$ using the same expression. In that case there is no noise and we use E_N=0. All previous studies have shown that at depths greater than a few hundred meters, the bound infragravity waves are negligible compared to the free waves (e.g. Webb et al.,

1991; Herbers et al., 1994 and Okihiro et al., 1993). We can thus compare directly the model results for $E(f)$ or H_{IG} to the measurements.

Because most high resolution data is not available from DART stations after the year 2008, and because the numerical wave model is most reliable for recent years when winds are best known (e.g. Rascle and Ardhuin, 2013), we have thus focused on the year 2008 and chosen the most energetic events for each of the North Pacific and the North Atlantic regions.

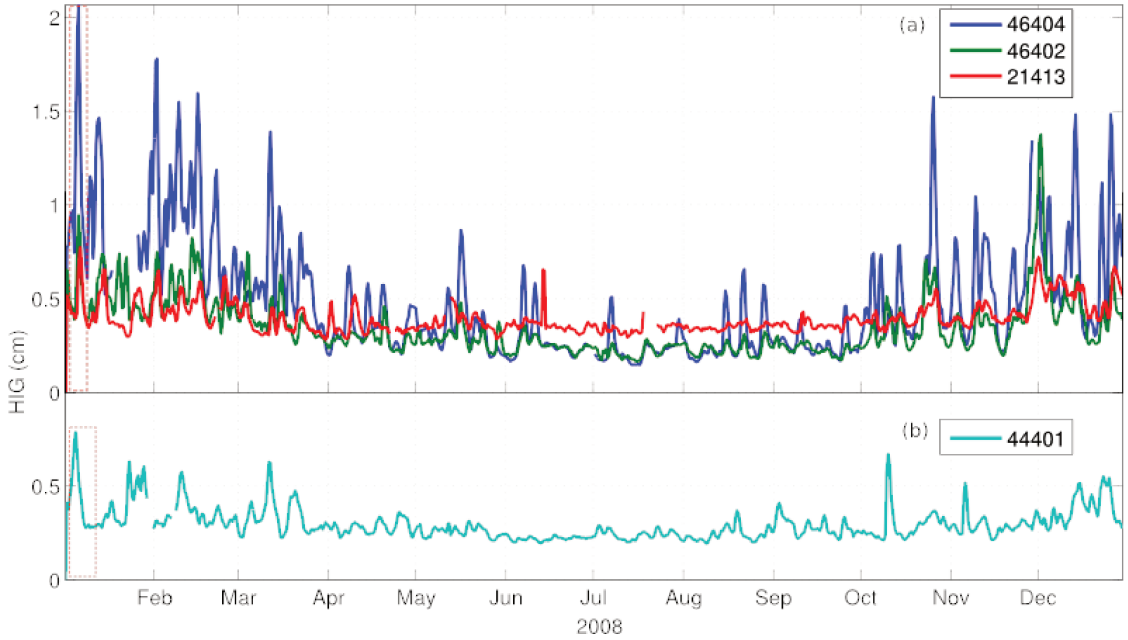

Figure 6.1: Time series of IG levels measured at (a) DART stations 46404 (off Oregon), 46402 (off Alaska) and 21413 (off Japan), all in the North Pacific and (b) DART station 44401 in the Atlantic. The red boxes mark the two events that are studied in detail. Pressure values were translated into surface elevation for the frequency range 5 mHz to 10mHz and the temporal resolution is 6 hours.

Observations shown in Figure 6.1 are for DART station 46404, 46402 and 21413 in the Pacific Ocean and DART station 44401 in the Atlantic Ocean cover both winter and summer seasons. Many peaks in all three Pacific time-series appear to coincide, especially during winter months, revealing that IG bursts are not localized events but can be coherent at the scale of ocean basins. A comprehensive analysis of the year 2008 (Supporting information figure) shows a good correlation between the peak levels recorded at DART stations 46407 and 21413 within a time lag of about 20 hours. The next section will focus on the most energetic events of the year 2008, one in the north Pacific, and one in the north Atlantic, that are representative of all the events for which the IG wave height reaches over 0.8 cm, when computed over the range 5 to 10 mHz.

6.2 IG waves across the Pacific

A major storm developed rapidly in the North Pacific and hit the Eastern Pacific coasts from Canada to Mexico on January 5, 2008, with offshore wave heights in excess of 10 m,

and peak periods of around 17 s. These large periods, high wave heights and the storm's large spatial extent combine to produce the largest source of infragravity signal recorded in 2008 at DART station 46404, located 4000 km offshore of Oregon at 2800 m depth. As defined by eq. (5), the IG wave height at the surface is estimated at 27 mm over the frequency band 5 to 10 mHz. Station 46407, located 400 km to the south also reported the highest value for that year during that event, with 31 mm. Across the Pacific, there is a clear IGW event occurring on January 6 (Figure 2), with heights of 5 mm at Pitcairn Island, in the Central Pacific (DART station 51406), 5 mm near the Philippines (station 52404), and 7 to 9 mm off Japan (stations 21413 and 21418). For these three west Pacific stations, these are the highest values recorded over the period January to March 2008. The same is true for the Aleutian island station 46408 with 13 mm recorded near 0 UTC on February 6. In contrast, the Hawaii station 51407, located 60 km west of Big Island, did not record anything particular on January 6, probably due to the masking effect of the island. Based on these measurements alone, it is very difficult to associate these records with a single event. It is the numerical model, as shown on Figure 6.2(a), which brings a clear picture of a coherent IG wave field forming on January 5 in the north-east Pacific and radiating across the oceans over the next two days. The model gives a picture of the IG wave heights that is strongly blocked by islands chains and amplified by mid-ocean topographic features. That amplification is due to the shoaling of these long waves when the water depth decreases. Infragravity waves have periods that are only a few times shorter than those of large tsunamis. IG and tsunami waves thus have very similar propagation speeds, and spatial distributions of amplitudes caused by shoaling and refraction.

These model gradients are difficult to validate with the few data available. Still, the general pattern of lower wave heights to the south of the source, and higher wave heights to the west is very well captured by the model, together with the timing of the IG wave arrival.

Contrary to many coastal shallow water sites that are often dominated by local IG waves, the deep ocean records in the west Pacific are thus dominated by IG waves that have travelled across the ocean basin. These remote IG waves are easily detected due to the lower levels of regionally generated IG energy. This lower level, following eq. (1), is the result of lower incident wave heights and shorter wave periods along the western boundaries of the Pacific basin.

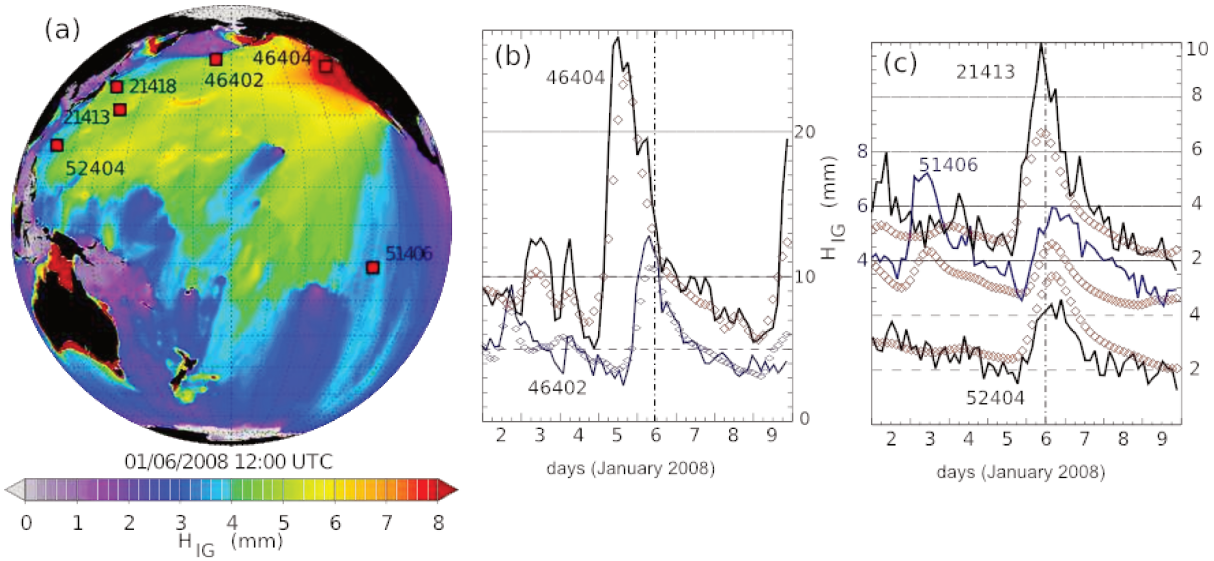

Figure 6.2: (a) Modelled infragravity wave heights at 12:00 UTC on 06/01/2008 over the Pacific Ocean with locations of pressure sensors used (red squares). (b) HIG measured (solid lines) and modelled (symbols) at DART stations close to the North American shorelines. (c) HIG measured (solid lines) and modelled (symbols) at remote DART stations, the curves have been offset vertically. Pressure measurements were translated into surface elevation using eqs. (4)-(5). The vertical dash-dotted line in (b) and (c) marks the time of the map shown in (a).

6.3 IG waves across the North Atlantic

A massive North-Atlantic winter storm developed off Newfoundland on January 2 2008, and generated waves with heights exceeding 15 m in the middle of the north Atlantic by the evening of January 2. High waves arrived in Portugal and Morocco, between January 3 and 4, with wave heights exceeding 10 m and peak periods around 20 s. The model predicts an IG burst propagating across the basin from the Eastern coasts to the Western coasts of the Atlantic (Figure 6.3(a)). Runs for locations OBS13 and JPP2 were carried out using the alternative IG model.

The model predicts IG waves with heights larger than 1 cm in deep water from Brazil to Iceland. These predictions are generally consistent with the few data available. There is even a clear maximum that exceeds 2 mm in the Caribbean Sea south of Puerto Rico (DART station 42407), that occurs at the time predicted by the model.

Only three DART stations had available records in the North Atlantic. These were supplemented by two additional observations collected as part of the geophysical experiment NEAREST and the seafloor pressure time series collected in the framework of the MoMAR Observatory (Ballu et al., 2009) In the context of the NEAREST project, broadband ocean bottom seismometers and hydrophones (OBS) were deployed in the Gulf of Cadiz for the period of September 2007 to August 2008. The OBS13 sensor was deployed the Gulf of Cadiz, at a depth of around 4500m. It is situated close to the source of the IG event and recorded a maximum height of 3.0 cm which coincides with the

maximum modelled value of 2.5 cm. Model estimates of H_{IG} at DART stations 44401 and 42407 are also in good agreement with the measurements. Discrepancies are more important at station 44402, off the U.S. coast.

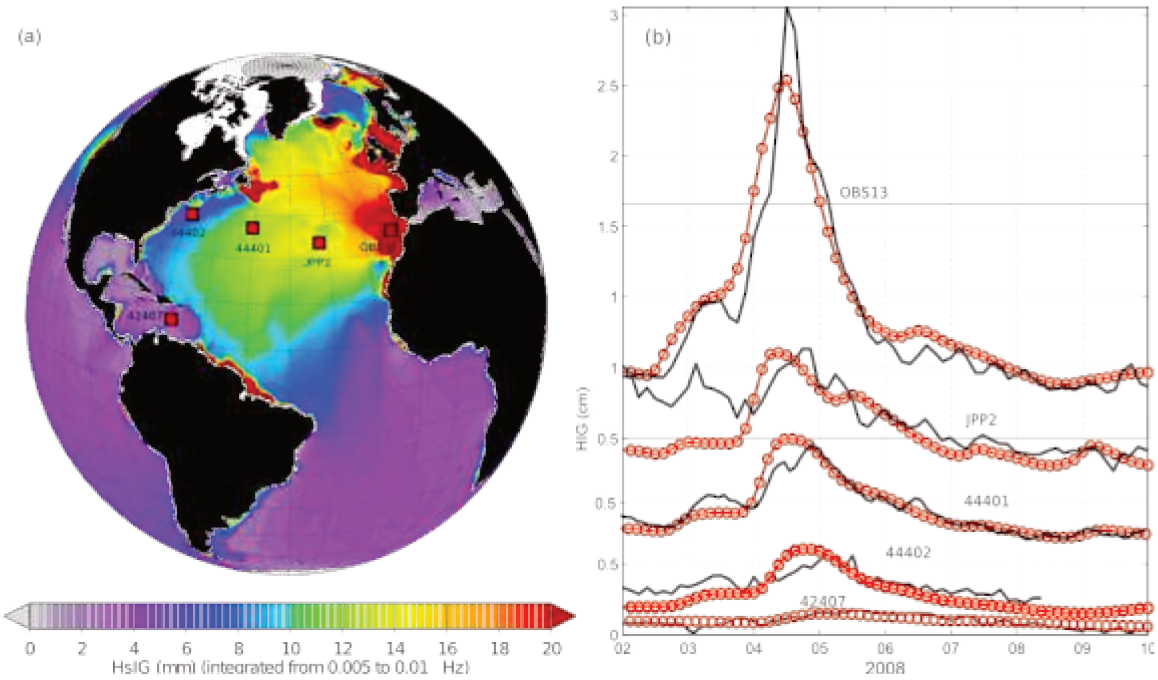

Figure 6.3 (a) Modelled instantaneous IG wave field on 06/01/2008 over the North-Atlantic Ocean with locations of pressure sensors used (red squares). (b) IG levels measured (black lines) and modelled values (red lines and circles) for the corresponding station. Pressure values were translated into surface elevation for the frequency range 0.005Hz to 0.010Hz

The spatial distribution of IG wave heights is marked by a strong shoaling and refraction across the Grand Banks, off Newfoundland. As a result, the U.S. East coast, including station 44402, receives a much lower level of IG energy. The shadowing effect of the Azores can also be noticed. The model also predicts an important amplification over the mid-Atlantic ridge, with values that are consistent with measurements made at the MoMAR Observatory JPP2 site. Before the IG event, the model underestimates the energy levels on January 2 and 3 at JPP2 and 44401. These are, according to the model, caused by the previous storm which hit the Portuguese coast on January 2. This model underestimation at JPP2 may be the result of an exaggerated sheltering by the Azores. According to the model, the January 4 event is the largest source of IG waves for that month, for most locations in the North Atlantic with depth larger than 2000 m, in the latitude band 5 to 55°N, including the Caribbean sea, but excluding the Gulf of Mexico which was rather sheltered from his event.

6.4 IG event from the South Pacific Ocean

The third IG event that was considered occurred in the southern Pacific Ocean along the western South American coast. The origins of this IG burst are waves from an unreferenced southern Pacific Ocean storm hitting the coast of Chile. The storm started

around the around the 17th of July 2008 and lasted for a few days. The level of IG energy liberated can be observed propagating across the whole Pacific Ocean with a fair signal level observed as far as DART station 46402 along the Alaskan coast.

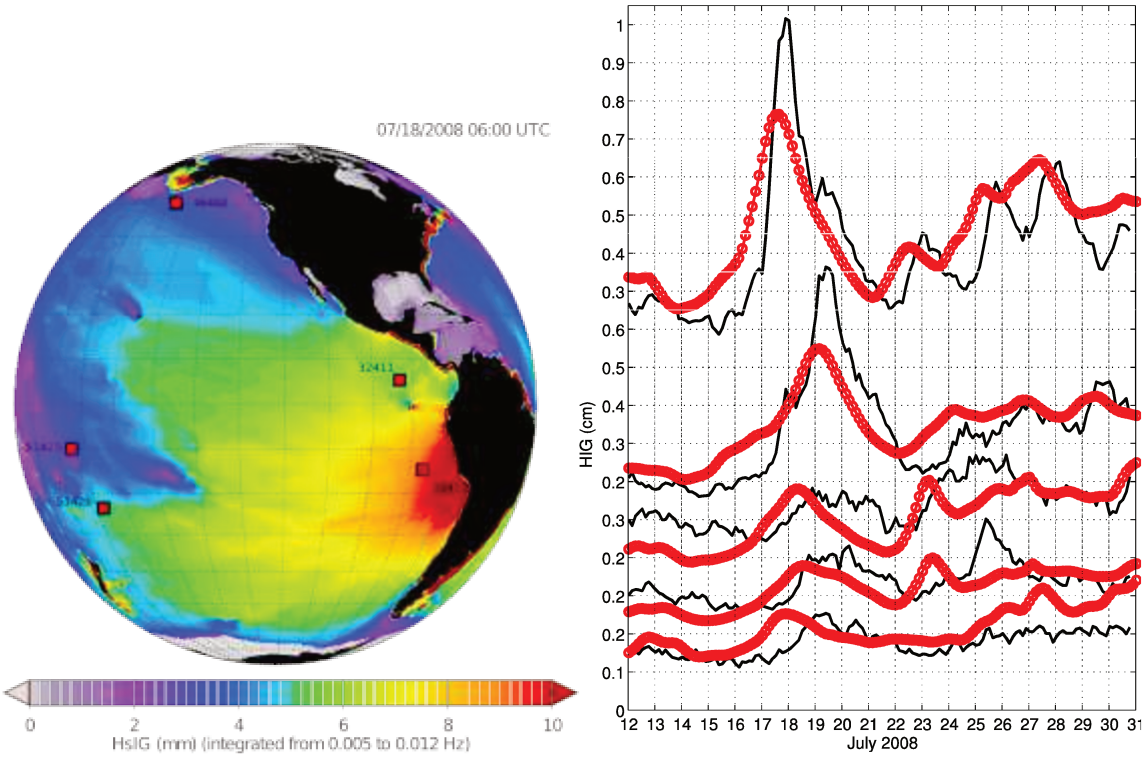

Figure 6.4 (a) Modelled instantaneous IG wave field on 18/07/2008 over the Pacific Ocean with locations of pressure sensors used (red squares). (b) IG levels measured (black lines) and modelled values (red lines and circles) at the corresponding DART stations. Pressure values were translated into surface elevation for the frequency range 0.005Hz to 0.09Hz

A total of 5 DART observations were available for this period. IG peak is slightly underestimated by the model at stations 32412 and 32411. The other 3 locations seem to have good IG level estimates. Here it can be observed that for all the points considered, the modeled signal is lagging the observed signal by a few hours. Since this lag is consistent for all the points, it can be deduced that the propagation in the model is not faulty. This could probably be due to the quality of the winds used to force the model.

6.5 Discussion

All three infragravity wave events highlighted here are caused by long period swells from extra-tropical storms with predominant westerly winds and waves. Waves propagating from east to west can also generate IG waves on western boundaries. However, given the scaling of the IG source with wave height and mean period squared, the sources off western boundaries of the Pacific and Atlantic Oceans are much weaker in general. Compared to the extra-tropical depressions, even hurricane waves are generally too small and with too short periods to generate comparable IGW bursts. From

the model runs used and available observations, few sources of strong IG event were found in the equatorial regions. For example, in 2008 only one clear event was observed at DARTs 42407, 44401 and 41424 around the 19th of March 2008. This event was noticeable in the region around Puerto Rico and the U.S. Virgin Islands. It was not associated with a tropical storm but rather to unusual long swell generation by an extratropical storm. This is the 'Extreme Atlantic Swell Event of March 2008' analyzed by Lefevre and Cooper et al. (2013). Another similar case of 'high swell from a remote storm' caused widespread flooding in western Pacific islands (Hoeke et al. 2013) on December 10, 2008.

IG generation in general is not limited to these storms and hurricanes, and any interaction of short waves with the coastlines will produce IG waves but their energy can be several orders of magnitude less than in the cases selected here. It is the intensity, duration and trajectory of the winter storms that define the largest wave heights and periods (e.g. Hanafin et al., 2012) and give rise to the strongest IG bursts.

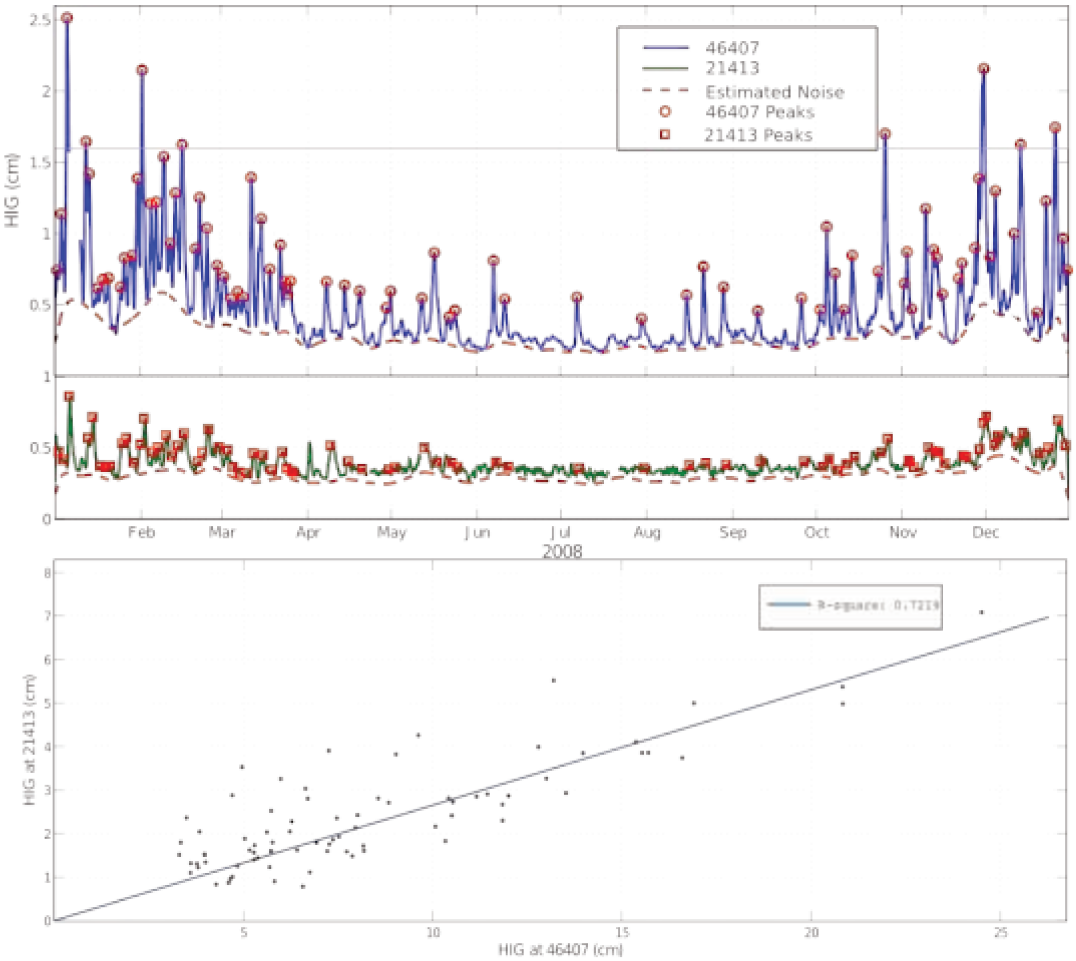

Figure 6.5 Figure showing HIG recorded at (a) DART station 46407 (in blue) and (b) 21413 (in green) and peaks greater than 5mm at station 46407 highlighted by red circles. The estimated noise is shown by red dashed curves. (c) The Correlation between noise-corrected IG wave peaks observed at DART 46404 and DART 21413 in the frequency range 0.005Hz to 0.010Hz and with a time lag of around 18 hours.

As observed on Figure 6.5, during the period of January to April and October to December 2008, a causal relationship between the peaks recorded by 2 pacific buoys, DART 46407 and DART 21413 is apparent. The peaks are always highest on the western part of the Pacific Ocean at DART 46407, and lower at DART 21413. Also the time lags between most of the corresponding peaks at these two stations seem to be constant.

When the IG wave heights observed at DART 46407 are plotted against those at DART 21413 the best correlation is obtained with a time lag of around 18 hours, especially for higher values of HIG. This corresponds approximately to the propagation time between these 2 locations for waves with speed in the studied frequency range and water depths. The good correlation observed strongly supports the westward propagation of IGW bursts with sources primarily on the eastern coast of the Pacific Ocean. The ratio between values of corresponding observations quantifies the attenuation of IG energy between these 2 locations.

Some aspects concerning the propagation distances and attenuation of tsunami waves were investigated by Rabinovich, et al., (2013). But they investigated the decay (in time) within ocean basins, rather than their attenuation along propagation paths. They suggested that higher frequency waves tend to dissipate everywhere whereas low frequency waves tend to dissipate mostly in shallow waters. The conclusion was that Pacific tsunamis dissipated due to shelf/coastal absorption processes, using the acoustic analogy of sound intensity in an enclosed room (Munk, 1963). The same reasoning is also valid for IG waves. The exact processes of this coastal dissipation has not been properly explained yet, and probably involves bottom friction near the coast and complex interactions with short waves in the surf zone as described in chapter 2.

6.5.1 Explanation for signal lag

Another issue is the time lag that could be underestimated by the model. When short-waves reach the shoreline, IG are generated and liberated. However, over the shelf the short waves would travel slower and reach the shoreline after some time before the IG are generated. The generated IG would also travel much slower over the shelf than in the deep ocean.

When the shelf is not well resolved, as could be the case if its width is comparable to the grid size, the modeled IG would have a tendency to have a small 'advance' over what is physically happening. This could partly explain the time lag between the modeled and observed signals, particularly for the event occurring in the South Pacific Ocean off the coast of South America. As a matter of fact, the shelf is quite narrow and is poorly resolved in the 0.5° global grid.

6.6 Conclusion

We have shown that free infragravity (free IG) waves radiating from coastlines along the eastern boundaries of ocean basins are the origin of the largest energy bursts in the infragravity band (here restricted to 5-10 mHz). Free IG waves are recorded by the global network of bottom pressure recorders used for tsunami warning, and other geophysical experiments using pressure gauges or hydrophones. The large free IG events are also well predicted by our spectral numerical model which uses empirical free infragravity sources determined from wind sea and swell properties all along the world's shorelines (Ardhuin et al. 2014).

Previous studies were based on the analysis of a single array at one location and estimated likely position and sometimes strengths of sources of the IG waves (Webb 1991, Harmon et al. 2012). Here we have combined scattered in situ observations and a global numerical model to demonstrate the trans-oceanic propagation of IG waves, which has not been explicitly documented previously. A typical example is the IG event recorded in the west Pacific off Japan or the Philippines on January 5, 2008, caused by swells on the North American coast, on the other side of the basin, 10000 km away and one day earlier.

The most energetic free IG events are associated with long period swells reaching a long stretch of shoreline. The model and the few available data support a similar behavior for the North Atlantic, and the model suggests the same for the South Atlantic and Indian oceans, with free IG energy generally radiating from east to west.

7 Conclusion

7.1 Achievements

Both the results from a 2D surf-beat model (XBeach) and analysis of field observations revealed the role of the normalized bed slope in shaping the outgoing free IG spectra through the coastal reflection of IG waves. We have also been able to use XBeach to model and propose an explanation to extreme IG levels observed around the island of Bannec off the coast of Brittany during winter storms.

We proposed links between IG observations and previously described mechanisms such as the coastal reflection of liberated IG waves (Battjes et al., 2004). This led to the successful construction of an alternative global IG model based on the liberation of bound IG waves, which appears to complement the empirical approach of Ardhuin et al. (2014). Several configurations were calibrated and tested with satisfactory results when compared to several observation datasets.

The role of a certain background IG level was noted in the observations. It could not be reproduced by the 2nd order approach only but seemed to have been partially included in the empirical approach. The complementarity between these two approaches was therefore highlighted, and the empirical approach was linked to the varying-breakpoint generation mechanism of Symonds et al. (1982).

Both IG models were then used to model some IG phenomena, notably the generation and propagation of several major IG events on an ocean-wide scale. Concerning these IG events, although it is generally well known that IG waves travel across oceans, and that local array measurements have suggested various source locations, these have never been previously verified with IG measurements right at the source. It is the first time that these propagations are explicitly observed and timed with appropriate observations along the propagation paths. The model lifts a possible ambiguity on the source distribution. The spatial variability of IG wave heights (observed or modeled) during this type of events were never studied previously except for tsunamis. We have also shown that free IG waves radiating from coastlines along the eastern boundaries of ocean basins are the origin of the largest energy bursts in the infragravity band.

7.2 Future improvements

The first improvement on both IG models would be to properly combine the varying-breakpoint IG generation mechanism with the liberation mechanism. Even though acceptable results were obtained with only the liberation mechanism, the addition of the breakpoint IG generation mechanism should allow a major refinement of the model. However good estimates of the slopes are needed since both the frequency distribution of the generated IG spectra and the choice between either of the two generation mechanisms depend on the normalised bed slope. The slopes along the coastlines of the

whole globe should be properly estimated and implemented in the model. In the global runs carried out, the global slopes were estimated using 1min ETOPO bathymetry, but this doesn't seem to be accurate enough. The tidal modulation of the IG level could also be added to the model as the tide can have an effect on the shoreline slopes.

Also, for the liberation mechanism, the growth of bound IG, which is also dependent on the normalized bed slope and which could play a role in the level of liberated IG was not integrated in the parametrization. This could also be a possible improvement on the model.

Another issue encountered with the global model was the time lag observed in some part of the oceans, such as the south pacific. This is probably due to the continental shelves not being resolved properly in some regions of the 0.5° grid. This is the case for the Chilean Pacific coastline.

A good method to resolve the shelf more accurately would be to carry out a nesting. For example a high resolution like (eg 1 km) coastal strip of about 1.0° width along the coasts of all the land masses including continents and islands can be nested into the actual 0.5° resolution global grid. This is expected to give better results without having to increase the grid resolution over the whole globe. This would also simplify the issue of subgrid islands.

Bibliography

Andrews, D.G., McIntyre, M.E., 1978. An exact theory of nonlinear waves on a Lagrangian-mean flow. J Fluid Mech 89, 609–646.

Ardhuin, F., Gualtieri, L., Stutzmann, E., 2015. How ocean waves rock the Earth: two mechanisms explain microseisms with periods 3 to 300 s: sources of microseisms from 3 to 300 s. Geophys. Res. Lett. n/a–n/a. doi:10.1002/2014GL062782

Ardhuin, F., Pineau-Guillou, L., Fichaut, B., Suanez, S., Corman, D., Filipot, J.-F., 2011. Extreme set-up and run-up on steep cliffs (Banneg Island, France), in: Proceedings, 12th Int. Workshop of Wave Hindcasting and Forecasting, Hawaii.

Ardhuin, F., Rawat, A., Aucan, J., 2014. A numerical model for free infragravity waves: Definition and validation at regional and global scales. Ocean Model. 77, 20–32.

Ardhuin, F., Roland, A., 2012. Coastal wave reflection, directional spreading, and seismo-acoustic noise sources. J Geophys Res 117, C00J20. doi:10.1029/2011JC007832

Aucan, J., Ardhuin, F., 2013. Infragravity waves in the deep ocean : An upward revision. Geophys Res Lett 40, 1–5. doi:10.1002/grl.50321

Baldock, T.E., 2006. Long wave generation by the shoaling and breaking of transient wave groups on a beach. Proc. R. Soc. Lond. Math. Phys. Eng. Sci. 462, 1853–1876. doi:10.1098/rspa.2005.1642

Baldock, T.E., Huntley, D.A., Bird, P.A.D., O'Hare, T., Bullock, G.N., 2000. Breakpoint generated surf beat induced by bichromatic wave groups. Coast. Eng. 39, 213–242. doi:10.1016/S0378-3839(99)00061-7

Ballu, V., Ammann, J., Pot, O., Viron, O. de, Sasagawa, G.S., Reverdin, G., Bouin, M.-N., Cannat, M., Deplus, C., Deroussi, S., Maia, M., Diament, M., 2009. A seafloor experiment to monitor vertical deformation at the Lucky Strike volcano, Mid-Atlantic Ridge. J. Geod. 83, 147–159. doi:10.1007/s00190-008-0248-3

Battjes, J.A., 1974. Surf similarity, in: Proceedings of the 14th International Conference on Coastal Engineering. ASCE, pp. 466–480.

Battjes, J.A., Bakkenes, H.J., Janssen, T.T., van Dongeren, A.R., 2004. Shoaling of subharmonic gravity waves. J. Geophys. Res. Oceans 109, C02009. doi:10.1029/2003JC001863

Benoit, M., Frigaard, P., Schäffer, H.A., 1997. Analysing multidirectional wave spectra: a tentative classification of available methods, in: Proceedings of the 1997 IAHR Conference, San Francisco. The Johns Hopkins University Press, Baltimore, pp. 131–158.

Biesel, F., 1952. Equations générales au second ordre de la houle irrégulière. Houille Blanche 5, 372–376.

Boussinesq, J., 1872. Théorie des ondes et des remous qui se propagent le long d'un canal rectangulaire horizontal, en communiquant au liquide contenu dans ce canal des vitesses sensiblement pareilles de la surface au fond. J Math Pures Appl 17, 55–108.

Bromirski, P.D., Sergienko, O.V., MacAyeal, D.R., 2010. Transoceanic infragravity waves impacting Antarctic ice shelves. Geophys Res Lett 37, L02502. doi:10.1029/2009GL041488

Bruno, D., De Serio, F., Mossa, M., 2009. The FUNWAVE model application and its validation using laboratory data. Coast. Eng. 56, 773–787. doi:10.1016/j.coastaleng.2009.02.001

Dongeren, A.V., Reniers, A., Battjes, J., 2003. Numerical modeling of infragravity wave response during DELILAH. J Geophys Res 108, 4.

Dongeren, A. van, Battjes, J., Janssen, T., Noorloos, J. van, Steenhauer, K., Steenbergen, G., Reniers, A., 2007. Shoaling and shoreline dissipation of low-frequency waves. J Geophys Res 112, C02011. doi:10.1029/2006JC003701

Elgar, S., Herbers, T.H.C., Guza, R.T., 1994. Reflection of ocean surface gravity waves from a natural beach. J Phys Ocean. 24, 1,503–1,511.

Evangelidis, D.A., 1996. Infragravity waves on the continental shelf. Naval Postgraduate School, Monterey, CA.

Fichaut, B., Suanez, S., 2011. Quarrying, transport and deposition of cliff-top storm deposits during extreme events: Banneg Island. Mar. Geol. 283, 36–55. doi:doi:10.1016/j.margeo.2010.11.003

Gobbi, M.F., Kirby, J.T., Wei, G., 2000. A fully nonlinear Boussinesq model for surface waves. II. Extension to $O(kh)^4$. J. Fluid Mech. 405, 181–210.

Godin, O.A., Zabotin, N.A., Sheehan, A.F., Collins, J.A., 2014. Interferometry of infragravity waves off New Zealand. J. Geophys. Res. Oceans 119, 1103–1122. doi:10.1002/2013JC009395

Godin, O.A., Zabotin, N.A., Sheehan, A.F., Yang, Z., Collins, J.A., 2013. Power spectra of infragravity waves in a deep ocean. Geophys Res Lett 40, 2159–2165. doi:10.1002/grl.50321

Guza, R.T., Thornton, E.B., 1985. Velocity moments in nearshore. J Waterw. Port Coast Ocean Eng 111, 235–256.

Hall, A.M., Hansom, J.D., Jarvis, J., 2008. Patterns and rates of erosion produced by high energy wave processes on hard rock headlands: The Grind of the Navir, Shetland, Scotland. Mar. Geol. 248, 28–46. doi:10.1016/j.margeo.2007.10.007

Hanafin, J., Quilfen, Y., Ardhuin, F., Vandemark, D., Chapron, B., Feng, H., Sienkiewicz, J., Queffeulou, P., Obrebski, M., Chapron, B., Reul, N., Collard, F., Cormand, D., Azevedo, E.B. de, Vandemark, D., Stutzmann, E., 2012. Phenomenal sea states and swell radiation: a comprehensive analysis of the 12-16 February 2011 North Atlantic storms. Bull Amer Meterol Soc 93, 1825–1832.

Harmon, N., Henstock, T., Srokosz, M., Tilmann, F., Rietbrock, A., Barton, P., 2012. Infragravity wave source regions determined from ambient noise correlation. Geophys Res Lett 39, L04604. doi:10.1029/2011GL050414

Harris, D., Matias, L., Thomas, L., Harwood, J., Geissler, W.H., 2013. Applying distance sampling to fin whale calls recorded by single seismic instruments in the northeast Atlantic. J Acoust Soc Amer 134, 3522–3535.

Hasselmann, K., 1963. On the non-linear energy transfer in a gravity wave spectrum Part 2: conservation theorems; wave-particle analogy; irreversibility. J Fluid Mech 15, 273–282.

Hasselmann, K., 1962. On the non-linear energy transfer in a gravity wave spectrum, part 1: general theory. J Fluid Mech 12, 481–501.

Henderson, S.M., Bowen, A.J., 2002. Observations of surf beat forcing and dissipation. J Geophys Res 107, 3193. doi:10.1029/2000JC000498

Henderson, S.M., Guza, R.T., Elgar, S., Herbers, T.H.C., Bowen, A.J., 2006. Nonlinear generation and loss of infragravity wave energy. J. Geophys. Res. Oceans 111. doi:10.1029/2006JC003539

Herbers, T.H.C., Elgar, S., Guza, R.T., 1995. Generation and propagation of infragravity waves. J Geophys Res 100, 24863–24872.

Herbers, T.H.C., Elgar, S., Guza, R.T., 1994. Infragravity-frequency (0.005-0.05 Hz) motions on the shelf, part I, forced waves. J Phys Ocean. 24, 917–927.

Herbers, T.H.C., Hendrickson, E.J., O'Reilly, W.C., 2000. Propagation of swell across a wide continental shelf. J Geophys Res 105, 19,729–19,737.

Holman, R., Bowen, A.J., 1984. Longshore structure of infragravity wave motions. J Geophys Res 89, 6446–6452.

Janssen, P., 2003. Nonlinear four-wave interactions and freak waves. J Phys Ocean. 33, 863–884.

Janssen, P.A.E.M., 2009. On some consequences of the canonical transformation in the Hamiltonian theory of water waves. J Fluid Mech 637, 1–44.

Kinsman, B., 1965. Wind waves. Prentice-Hall, Englewood Cliffs, N. J.

Krasitskii, V.P., 1994. On reduced equations in the Hamiltonian theory of weakly nonlinear surface waves. J Fluid Mech 272, 1–20.

Lecornu, F., De Roeck, Y.-H., 2009. PREVIMER - Observations & Prévisions Côtières. Houille Blanche 60–63. doi:10.1051/lhb:2009006

Lin, P., Liu, P.L.-F., 1998. A numerical study of breaking waves in the surf zone. J. Fluid Mech. 359, 239–264. doi:10.1017/S002211209700846X

Lippmann, T.C., Herbers, T.H.C., Thornton, E.B., 1999. Gravity and Shear Wave Contributions to Nearshore Infragravity Motions. J Phys Ocean. 24, 231–239.

Longuet-Higgins, M.S., 1957. The Statistical Analysis of a Random, Moving Surface. Philos. Trans. R. Soc. Lond. Ser. Math. Phys. Sci. 249, 321–387.

Longuet-Higgins, M.S., Stewart, R.W., 1964. Radiation stress in water waves, a physical discussion with applications. Deep Sea Res. 11, 529–563.

Longuet-Higgins, M.S., Stewart, R.W., 1962. Radiation stresses and mass transport in surface gravity waves with application to `surf beats'. J Fluid Mech 13, 481–504.

Longuet-Higgins, M.S., Stewart, R.W., 1960. Changes in the form of short gravity waves on long waves and tidal currents. J Fluid Mech 8, 565–583.

Lynett, P., Liu, P.L.-F., 2004. A two-layer approach to wave modelling. Proc Roy Soc Lond A 460, 2637–2669.

Madsen, P.A., Bingham, H.B., Schäffer, H.A., 2003. Boussinesq-type formulations for fully nonlinear and extremely dispersive water waves: derivation and analysis. Proc. R. Soc. Lond. Math. Phys. Eng. Sci. 459, 1075–1104. doi:10.1098/rspa.2002.1067

Madsen, P.A., Murray, R., Sørensen, O.R., 1991. A new form of the Boussinesq equations with improved linear dispersion characteristics. Coast. Eng. 15, 371–388. doi:10.1016/0378-3839(91)90017-B

Madsen, P.A., Sørensen, O.R., 1993. Bound waves and triad interactions in shallow water. Ocean Eng. 20, 359–388. doi:10.1016/0029-8018(93)90002-Y

Miche, A., 1944. Mouvements ondulatoires de la mer en profondeur croissante ou décroissante. Forme limite de la houle lors de son déferlement. Application aux digues maritimes. Deuxième partie. Mouvements ondulatoires périodiques en profondeur régulièrement décroissante. Ann. Ponts Chaussées Tome 114, 131–164,270–292.

Munger, S., Cheung, K.F., 2008. Resonance in Hawaii waters from the 2006 Kuril Islands Tsunami. Geophys. Res. Lett. 35, L07605. doi:10.1029/2007GL032843

Munk, W.H., 1950. Origin and generation of waves, in: Proceedings 1st International Conference on Coastal Engineering, Long Beach, California. ASCE, pp. 1–4.

Munk, W.H., 1949. Surf beat. Eos Trans AGU 30, 849–854.

Okihiro, M., Guza, R.T., Seymour, R.J., 1993. Excitation of Seiche Observed in a Small Harbor. J Geophys Res 98, 18201–18211.

Oltman-Shay, J., Guza, R.T., 1987. Infragravity edge wave observations on two California beaches. J Phys Ocean. 17, 644–663.

Pomeroy, A., Lowe, R., Symonds, G., Van Dongeren, A., Moore, C., 2012. The dynamics of infragravity wave transformation over a fringing reef. J. Geophys. Res. Oceans 117, C11022. doi:10.1029/2012JC008310

Rascle, N., Ardhuin, F., 2013. A global wave parameter database for geophysical applications. Part 2: model validation with improved source term parameterization. Ocean Model. 70, 174–188. doi:10.1016/j.ocemod.2012.12.001

Rawat, A., Ardhuin, F., Ballu, V., Crawford, W., Corela, C., Aucan, J., 2014. Infragravity waves across the oceans. Geophys. Res. Lett. 41, 2014GL061604. doi:10.1002/2014GL061604

Reniers, A.J.H.M., Dongeren, A.R. van, Battjes, J.A., Thornton, E.B., 2002. Linear modeling of infragravity waves during Delilah. J Geophys Res 107, 3137. doi:10.1029/2001JC001083

Reniers, A.J.H.M., Groenewegen, M.J., Ewans, K.C., Masterton, S., Stelling, G.S., Meek, J., 2010. Estimation of infragravity waves at intermediate water depth. Coast. Eng 57, 52–61.

Rijnsdorp, D.P., Smit, P.B., Zijlema, M., 2014. Non-hydrostatic modelling of infragravity

waves under laboratory conditions. Coast. Eng. 85, 30–42. doi:10.1016/j.coastaleng.2013.11.011

Roelvink, D., Reniers, A., Dongeren, A. van, Vries, J. van T. de, McCall, R., Lescinski, J., 2009a. Modelling storm impacts on beaches, dunes and barrier islands. Coast. Eng 56, 1133–1152.

Roelvink, D., Reniers, A., van Dongeren, A., van Thiel de Vries, J., McCall, R., Lescinski, J., 2009b. Modelling storm impacts on beaches, dunes and barrier islands. Coast. Eng. 56, 1133–1152. doi:10.1016/j.coastaleng.2009.08.006

Ruessink, 1998. Bound and free infragravity waves in the nearshore zone under breaking and nonbreaking conditions. J Geophys Res 103, 12795–12805.

Ruggiero, P., Holman, R.A., Beach, R.A., 2004. Wave run-up on a high-energy dissipative beach. J. Geophys. Res. Oceans 109, C06025. doi:10.1029/2003JC002160

Ruju, A., Lara, J.L., Losada, I.J., 2012. Radiation stress and low-frequency energy balance within the surf zone: A numerical approach. Coast. Eng 68, 44–55.

Schäffer, H., 1993. Infragravity waves induced by short-wave groups. J Fluid Mech 247, 551–588.

Senechal, N., Coco, G., Bryan, K.R., Holman, R.A., 2011. Wave runup during extreme storm conditions. J. Geophys. Res. 116. doi:10.1029/2010JC006819

Sheremet, A., Staples, T., Ardhuin, F., Suanez, S., Fichaut, B., 2014. Observations of large infragravity-wave run-up at Banneg Island, France. Geophys Res Lett 41.

Shi, F., Kirby, J.T., Harris, J.C., Geiman, J.D., Grilli, S.T., 2012. A high-order adaptive time-stepping TVD solver for Boussinesq modeling of breaking waves and coastal inundation. Ocean Model. 43–44, 36–51. doi:10.1016/j.ocemod.2011.12.004

Stelling, G., Zijlema, M., 2003. An accurate and efficient finite-difference algorithm for non-hydrostatic free-surface flow with application to wave propagation. Int. J. Numer. Methods Fluids 43, 1–23. doi:10.1002/fld.595

Stokes, G.G., 1849. On the theory of oscillatory waves. Trans Camb Phil Soc 8, 441–455.

Svendsen, I.A., 1984. Wave heights and set-up in a surf zone. Coast. Eng 8, 303–329.

Symonds, G., Huntley, D.A., A. J. Bowen, 1982. Two-dimensional surf beat: Long wavegeneration by a time-varying breakpoint. J Geophys Res 87, 492–498.

Toledo, Y., Hsu, T.-W., Roland, A., 2012. Extended time-dependent mild-slope and wave-action equations for wave-bottom and wave-current interactions. Proc Roy Soc Lond A 468, 184–205. doi:10.1098/rspa.2011.037

Tolman, H.L., 2002. Limiters in third-generation wind wave models. Glob. Atmos Ocean Syst 8, 67–83.

Tolman, H.L., Accensi, M., Alves, H., Ardhuin, F., Bidlot, J., Booij, N., Bennis, A.-C., Campbell, T., Chalikov, D.V., Chawla, A., Filipot, J.-F., Foreman, M., Janssen, P., Leckler, F., Jian-Guo, Orzech, K.L.M., Padilla-Hernández, R., Rogers, W.E., Rawat, A., Roland, A., Sikiric, M.D., Szyszka, M., Tolman, H.L., Tracy, B., Vledder, G.P. van, Westhuysen, A. van der, Zieger, S., 2014. User manual and system documentation

of WAVEWATCH-III$^\rmTM$ version 4.18 (No. 316). NOAA/NWS/NCEP/MMAB.

Tucker, M., 1950. Surf beats: sea waves of 1 to 5 min. period. Proc Roy Soc Lond A 202, 565–573.

Van Dongeren, A., Reniers, A., Battjes, J., Svendsen, I., 2003. Numerical modeling of infragravity wave response during DELILAH. J. Geophys. Res. Oceans 108, 3288. doi:10.1029/2002JC001332

Vis, F.C., Mol, A., Rita, M.M., Deelen, C., 1985. Long waves and harbour design. Int Conf Num Hyd Model. Ports Harb. 249–255.

Wadhams, P., Doble, M.J., 2008. Digital terrain mapping of the underside of sea ice from a small AUV. Geophys. Res. Lett. 35. doi:10.1029/2007GL031921

WAMDI Group, 1988. The WAM Model - A third generation ocean wave prediction model. J Phys Ocean. 18, 1775–1810.

Webb, S., Zhang, X., Crawford, W., 1991. Infragravity waves in the deep ocean. J Geophys Res 96, 2723–2736.

Wei, G., Kirby, J.T., Grilli, S.T., Subramanya, R., 1995. A fully nonlinear Boussinesq model for surface waves. Part 1. Highly nonlinear unsteady waves. J Fluid Mech 294, 71–92.

Zakharov, V.E., Kuznetsov, E.A., 1997. Hamiltonian formalism for nonlinear waves. Phys.-Uspekhi 40, 1087–1116.

Zijlema, M., Stelling, G., Smit, P., 2011. SWASH: An operational public domain code for simulating wave fields and rapidly varied flows in coastal waters. Coast. Eng 58, 992–1012.

Appendix - Radiation stress

The bound long waves in a regular wave group were shown by Longuet-Higgins and Stewart, (1962) by to be produced by fluxes of mass and momentum associated with the short waves . It is the nonlinearities in the momentum balance of surface gravity waves that result in momentum being transferred from the surface wave frequency to low frequency oscillations. These fluxes of mass and momentum act through the radiation stress which is an internal compressive force proportional to the square of the wave height.

Radiation stress is the depth-integrated and phase-averaged excess momentum flux caused by the presence of the surface gravity waves, which is exerted on the mean flow. It behaves as a second-order tensor that describes the additional forcing due to the presence of the waves. This changes the mean depth-integrated horizontal momentum in the fluid layer and as a result the variation of the radiation stresses induce changes in the mean surface elevation (wave setup) and the mean flow (wave-induced currents). The radiation stress tensor, and its implications on the physics of surface gravity waves and mean flows, was formulated by Longuet-Higgins and Stewart (1960, 1962, 1964).

For wave propagation in two horizontal dimensions the radiation stress tensor is

$$\mathbf{S} = \begin{pmatrix} S_{xx} & S_{yx} \\ S_{xy} & S_{yy} \end{pmatrix} \qquad \text{[I-1]}$$

Where the components are given by

$$S_{xx} = \overline{\int_{-D}^{\eta} (p + \rho\tilde{u}^2)\, dz} - \frac{1}{2}\rho g(D + \bar{\eta})^2 \qquad \text{[I-2]}$$

$$S_{yy} = \overline{\int_{-D}^{\eta} (p + \rho\tilde{v}^2)\, dz} - \frac{1}{2}\rho g(D + \bar{\eta})^2 \qquad \text{[I-3]}$$

$$S_{xy} = S_{xy} = \overline{\int_{-D}^{\eta} (\rho\tilde{u}\tilde{v}\,)\, dz} \qquad \text{[I-4]}$$

Where D is the water depth, $\tilde{u}$ and $\tilde{v}$ are the horizontal *x*- and *y*-components of the oscillatory part of the flow velocity vector and $\bar{\eta}$ is the surface elevation averaged over several wave crests. For regular wave groups, these expressions can then be simplified to

$$S_{xx} = \rho g \left[E \frac{C_g}{C} cos^2\theta + \frac{E}{2}\left(2\frac{C_g}{C} - 1\right)\right] \quad \text{[I-5]}$$

$$S_{yy} = \rho g \left[E \frac{C_g}{C} sin^2\theta + \frac{E}{2}\left(2\frac{C_g}{C} - 1\right)\right] \quad \text{[I-6]}$$

$$S_{xy} = S_{xy} = \rho g E \frac{C_g}{C} sin\theta \, cos\theta \quad \text{[I-7]}$$

Where E is the total wave energy, C the wave velocity and C_g the group velocity and θ is the angle of the wave propagation with respect to the x-axis (normal to the beach).

Newton's second law of motion requires that gradients in these radiation stresses must be balanced by a steady force and consequently this result in wave setup or setdown and longshore currents. In regions of high wave energy the radiation stress S_{xx} is greater than in regions of low energy. Hence there is a tendency for fluid to be expelled from under regions of high energy density. The medium responds to the stress as to a horizontal force $-\frac{\partial S_{xx}}{\partial x}$ per unit distance, progressing with the group-velocity C_g. For a 1-D case, neglecting surface and bottom tensions the conservation of momentum **M** along the x direction gives

$$\frac{\partial \boldsymbol{M}}{\partial t} = -\frac{\partial}{\partial x}(S_{xx} + \rho g D \bar{\eta}) \quad \text{[I-8]}$$

The continuity equation gives

$$\frac{\partial(\rho\bar{\eta})}{\partial t} = -\frac{\partial \boldsymbol{M}}{\partial x} \quad \text{[I-9]}$$

Since the pattern progresses with velocity C_g, we may replace $\frac{\partial}{\partial x}$ by $-\frac{1}{C_g}\frac{\partial}{\partial t}$. Hence we obtain

$$\rho \frac{\partial \bar{\eta}}{\partial x} = -\frac{1}{gD - {C_g}^2}\frac{\partial S_{xx}}{\partial x} \quad \text{[I-10]}$$

$$\frac{\partial \boldsymbol{M}}{\partial x} = -\frac{C_g}{gD - {C_g}^2}\frac{\partial S_{xx}}{\partial x} \quad \text{[I-11]}$$

Which on integration and with appropriate constants of integration give

$$\bar{\eta} = -\frac{S_{xx}}{\rho\left(gD - {C_g}^2\right)} \quad \text{[I-12]}$$

$$\boldsymbol{M} = -\frac{C_g S_{xx}}{gD - {C_g}^2} \quad \text{[I-13]}$$

It should be noted that the linear dependency of $\bar{\eta}$ on S_{xx} and hence on the total wave energy E, means that there is a quadratic dependency of the bound long-waves with the short wave height H_s.

Waves propagating towards the shore start to break at a certain position and subsequently they transform into turbulent bores. Energy, released due the wave breaking is first transferred to a 'roller'. This roller is defined as the rotating part resting on the wave front, which propagates with the phase velocity. A shear stress will develop due to the velocity difference between the roller and the underlying water particles and this stress dissipates the roller energy in the surf zone.

So a roller contribution can also be added to the previously defined radiation stresses.

$$S_{xx,roller} = 2\rho g E_r cos^2\theta \quad \text{[I-14]}$$

$$S_{yy,roller} = 2\rho g E_r sin^2\theta \quad \text{[I-15]}$$

$$S_{xy,roller} = S_{xy,roller} = 2\rho g E_r sin\theta\ cos\theta \quad \text{[I-16]}$$

where E_r is the kinetic roller energy density that can be defined as a function of the roller area and the length of the wave front as in Svendsen (1984).

If we assume that the wave field changes slowly in time, the radiation stress gradients can be included in the momentum balance of long wave models such as for example Reniers et al (2004) where the short-wave averaged, depth-averaged velocity field is computed with nonlinear shallow water equations. In this case the continuity and momentum equations are given by

$$\frac{\partial \eta}{\partial t} + \frac{\partial (hu)}{\partial x} + \frac{\partial (hv)}{\partial y} = 0 \quad \text{[I-17]}$$

$$\frac{\partial u}{\partial t} + u\frac{\partial u}{\partial x} + v\frac{\partial v}{\partial y} = -F_x - g\frac{\partial \eta}{\partial x} + \nu_h\left(\frac{\partial^2 u}{\partial x^2} + \frac{\partial^2 u}{\partial y^2}\right) - \frac{\tau_x}{h} \quad \text{[I-18]}$$

$$\frac{\partial v}{\partial t} + u\frac{\partial v}{\partial x} + v\frac{\partial v}{\partial y} = -F_y - g\frac{\partial \eta}{\partial y} + \nu_h\left(\frac{\partial^2 v}{\partial x^2} + \frac{\partial^2 v}{\partial y^2}\right) - \frac{\tau_y}{h} \quad \text{[I-19]}$$

Where ν_h is the horizontal turbulent eddy viscosity, τ_x and τ_x represent the combined short-wave and (Eulerian) current bottom shear stress operating in the cross-shore and alongshore directions respectively and F_x and F_y are the wave and roller-induced forces defined as

$$F_x = \frac{1}{\rho h}\left(\frac{\partial S_{xx}}{\partial x} + \frac{\partial S_{yx}}{\partial y}\right) \quad \text{[I-20]}$$

$$F_y = \frac{1}{\rho h}\left(\frac{\partial S_{yy}}{\partial y} + \frac{\partial S_{xy}}{\partial x}\right) \quad \text{[I-21]}$$

Also included in the formulation, but not described here, are the conservation equations for the short-wave energy balance, and for the kinetic roller energy balance.

It is a similar approach that is used by Roelvink et al. (2009) for XBeach, with a Generalized Lagrangian Mean (GLM) formulation.

Résumé

Les vagues de surface qui sont généralement générées par le vent et appelées houle ou mer de vent, sont omniprésents à la surface de l'océan. Ils ont des périodes variant entre 2 et 25 secondes et de longueur d'onde variant de quelques mètres à plusieurs centaines de mètres. Il existe aussi des ondes plus longues et à plus basse fréquence appelés ondes infragravitaires (IG), qui sont associés aux groupes de vagues courtes, générées par le vent. Ces ondes IG ont des périodes dominantes comprise entre 30 secondes et 10 minutes et, quand ils se propagent librement, avec des longueurs d'ondes pouvant atteindre plusieurs dizaines de kilomètres. En dehors de la zone de surf, l'amplitude verticale de ces ondes infragravity est de l'ordre de 1 à 10 cm, tandis que l'amplitude des vagues courtes est de l'ordre de 1-10 m.

Malgré leurs petites échelles d'amplitude, ces ondes infragravitaires peuvent avoir une importance non-négligeable dans certaines situations. Elles peuvent par exemple exciter des phénomènes de seiches dans les ports et mettre en résonance des structures en mer et des lames de glaces dans l'arctique ou l'antarctique. Le champ d'ondes infragravitaires constitueront probablement aussi une fraction significative du signal mesuré par la future mission du satellite Surface Water Ocean Topography (SWOT). Ce champ d'onde infragravity devra être caractérisé pour atteindre la précision attendue sur les mesures de hauteur de mer dynamiques. Il est probable que la précision visée ci-dessus ne soit pas possible pour les forts états de mer avec de longues houles. L'un des objectifs de cette thèse était de fournir une première quantification de ces incertitudes associées. Au-delà de la mission SWOT, la quantification du champ d'ondes IG est un problème clé pour la compréhension de plusieurs autres phénomènes géophysiques tels que la compréhension des microséismes.

Mots clés : Ondes infragravitaires, SWOT, modélisation à l'échelle globale